Mechanical and chemical activation of CaO-based sorbents for post-combustion CO_2 capture at high temperature

by

Ehsan Hassani

A dissertation submitted to the Graduate Faculty of
Auburn University
in partial fulfillment of the
requirements for the Degree of
Doctor of Philosophy

Auburn, Alabama
May 7, 2022

Keywords: CaO-based sorbent, CO_2 capture, in situ X-ray, temperature programmed carbonation
Ball milling, Ca_2CuO_3 nanofiber

Approved by

Tae-Sik Oh, Assistant Professor, Department of Chemical Engineering
Jin Wang, Professor, Department of Chemical Engineering
Andrew Adamczyk, Assistant Professor, Department of Chemical Engineering
Bart Porork, Professor, Department of Material Engineering
Sushil Adhikari, Professor, Department of Biosystem Engineering

Abstract

The Calcium Looping (CaL) process is one of the most efficient technology for post-combustion CO_2 capture. The raw material for CO_2 adsorption is CaO which can be derived from limestone. The abundance and high capacity of this sorbent make the process highly favorable. Despite the advantages of CaO, regenerability remains a significant challenge. In the CaL process, CaO losses its surface area and pore structure due to the high temperature at the regeneration process. Therefore, the development of CaO-based sorbents is necessary to improve the overall efficacy of the technology.

In this work, mechanical and chemical activation of CaO-based sorbents were investigated. Through the mechanical activation, ball-milling was used to synthesize high surface and porous material to increase the conversion of the sorbent in the carbonation reaction stage. Carbonation, regeneration, and cycle stability of mechanically activated $Ca(OH)_2$ were investigated using in situ XRD technique. The results showed the overall efficacy of the process increased by 24%. Although mechanical activation of the sorbent increased the conversion initially, the cycle stability remained challenging.

Chemical activation method was applied to the sorbent. Three different transient metals (Cu, Co, Fe) were selected to synthesize calcium metal oxides. The performance of these sorbents was investigated and we found that Ca_2CuO_3 has a decent potential to be a suitable sorbent for post-combustion CO_2 capture. The sorbent showed a high regeneration kinetic even at lower temperatures compared to CaO. A decomposing process was developed for Ca_2CuO_3 to improve the performance of the sorbent for CO_2 capture. Using hydrogen, Ca_2CuO_3 decomposed to CaO and Cu. The former was the active material to adsorb CO_2, while the latter provided a facile heat

transfer to mitigate sintering. A high stability performance was observed for the fully decomposed Ca_2CuO_3. Finally, the direction for future works was proposed.

Acknowledgments

There is always something to be thankful for, and for my Ph.D. journey, there are many great people that I would like to thank.

I would like to thank my advisor, Dr. Tae-Sik Oh, for his support, dedication, guidance, and mentorship on my Ph.D. project. I want to thank former and current members of Dr. Oh's Lab; Myeongseok Sim, Ali Rashti, and Farshad Feyzbar, for their friendship, assistance with research experiments, and their advice on my research work. Thank you to the undergraduate students, Logan Respess, Rachel Haigh and Dalton Green for their help with experiments and data analysis. I would like to thank Dr. Jin Wang, Dr. Andrew Adamczyk, Dr. Bart Porork, and Dr. Sushil Adhikari for their willingness to serve on my committee and for feedback on this thesis which made this work more valuable.

I am extremely grateful to my parents, Hamidollah and Fereshteh Hassani. I could not be here without their support throughout my entire life. I am so grateful to have my brother, Iman, and his family who have made my life much easier in the USA. I would like to thank my sister, Fatemeh, for her kindness and support. I would also like to thank my in-law family: Lee McCoy, Katrina McCoy, Kathryn McCoy, and Della Cook. They have truly adopted me as their own and have shown me endless kindness and inclusion.

Last but not least, I would like to thank the love of my life, Maggie. I cannot be thankful enough for her support during my PhD. I see myself as the luckiest man in the world to have the kindest wife who supported me emotionally in my academic and my personal life. I wanted to let you know that this journey would not be possible without you.

Table of Contents

Abstract 2

Acknowledgments 4

List of Tables 9

List of Figures 11

List of Abbreviations 18

Chapter 1 Literature review 19

1.1 Introduction 19

1.1.1 Pre-combustion 22

1.1.2 Oxy-fuel combustion 23

1.1.3 Post-combustion 23

1.1.3.1 Calcium Looping process 26

1.1.3.2 Models for CaO carbonation 28

1.1.3.2.1 The grain model 29

1.1.3.3 Deactivation of CaO in the Calcium Looping process 31

Chapter 2 Carbonation, regeneration, and cycle stability of the mechanically activated $Ca(OH)_2$ sorbents for CO_2 capture: An in situ X-ray diffraction study 33

Abstract 33

2.1 Introduction 33

2.2 Experimental section 36

2.2.1 Sorbent preparation 37

2.2.2 CO_2 capture test 38

2.3 Results and discussion 44

2.3.1 Sorbent characterization 44
2.3.2 Carbonation/regeneration of sorbents without mechanical activation 48
2.3.3 Carbonation kinetics 50
2.3.4 Regeneration kinetics 52
2.3.5 Isothermal cycle stability 55
2.4 Conclusion 62
Chapter 3 Ca_2CuO_3: A high temperature CO_2 sorbent with rapid regeneration kinetics 64
Abstract 64
3.1 Introduction 64
3.2 Experimental section 68
3.2.1 Sorbent preparation 68
3.2.2 Temperature swing carbonation and decarbonation 70
3.2.3 Enthalpy calculation 71
3.2.4 Results and Discussion 73
3.2.4.1 Synthesized sorbent 73
3.2.4.2 Temperature programmed carbonation and decarbonation (TPC-TPDC) 76
3.2.4.3 CO_2 uptake and sorbent conversion 78
3.2.4.4 Effect of initial $Ca(OH)_2$ on TPC-TPDC 79
3.2.4.5 Behavior of calcium-based ternary oxide sorbents 83
3.3 Conclusion 96
Chapter 4 Solid-state decomposition of Ca_2CuO_3 enhances its CO_2 reactivity and cycle stability 99
Abstract 99

4.1 Introduction 100
4.2 Experimental 102
4.2.1 Sorbent preparation 102
4.2.1.1 CaO 102
4.2.1.2 Ca_2CuO_3 (N-CCO) 102
4.2.1.3 Fully decomposed Ca_2CuO_3 (F-CCO) 102
4.2.1.4 Partially decomposed Ca_2CuO_3 (P-CCO) 103
4.2.2 Sorbents characterization 103
4.2.3 CO_2 capture test 103
4.2.3.1 Ex situ experiment 103
4.2.3.2 In situ experiment 104
4.2.3.2.1 Temperature-resolved carbonation and regeneration experiment 105
4.2.3.2.2 Time-resolved carbonation and regeneration experiment 105
4.2.3.2.3 Isothermal stability test 106
4.3 Result and discussion 106
4.3.1 Sorbent characterization 106
4.3.2 Temperature-resolved carbonation and regeneration 112
4.3.2.1 Carbonation behavior of N-CCO and F-CCO 112
4.3.2.2 Regeneration behavior of the carbonated N-CCO and F-CCO 115
4.3.3 Time-resolved carbonation and regeneration 118
4.3.3.1 Isothermal carbonation kinetics 118
4.3.3.2 Isothermal regeneration kinetics 120
4.3.4 Stability of the sorbents 122

4.4 Conclusion 127

Chapter 5 Conclusion and future work 129

5.1 Synthesizing nanofiber sorbents 130

5.2 Synthesizing composite sorbents with high melting point and thermal conductivity 135

5.3 Using CaO based sorbent for carbon capture at low temperatures 137

References 142

List of Tables

Table 2.1. Samples characterization: BET, X-ray diffraction, and dynamic light scattering analysis. 45

Table 3.1. Crystal parameter of the synthesized sorbents. 74

Table 3.2. Peak positions (2θ) and Miller indices of the synthesized sorbents..... 75

Table 3.3. CO_2 uptake and sorbent conversion for CaO, Ca_2CuO_3, $Ca_3Co_4O_9$ and $Ca_2Fe_2O_5$ in various CO_2 concentrations. Sorbent mass = 0.5 g. 84

Table 3.4. The result of Rietveld Refinement (using Maud software) for the sorbents after TPC-TPDC. 88

Table 3.5. The amount of CO_2 uptake in each cycle for CaO and Ca_2CuO_3 when the sorbents were cycled between T_c and T_d. 94

Table 3.6. The amount of CO_2 release in each cycle for CaO and Ca_2CuO_3 when the sorbents were cycled between T_c and T_d. 95

Table 4.1. The miller index of each peak in Figure 4.1. the balk, red, blue and green colors show the peaks information of CaO, Ca_2CuO_3, Cu_2O and Cu respectivly. The reference data was obtained from Crystallography Crystallography Open Database [132-138]. 108

Table 4.2. Thermal properties of relevant materials. 126

Table 4.3. Crystal size of CaO phase in the sorbents within $\pm 2\ nm$ error. 126

Table 5.1. The performance comparison of Ca_2CuO_3 powder and Ca_2CuO_3 nanofiber under 20% of CO_2 in temperature swing carbonation/ decarbonation experiment. 132

Table 5.2. CO_2 pressure and conversion over time under 300 rpm ball milling when $Ca(OH)_2$ was used as the sorbent..... 137

List of Figures

Figure 1.1. The level of carbon dioxide concentration throughout history. (Credit: Luthi, D., et al.. 2008; Etheridge, D.M., et al. 2010; Vostok ice core data/J.R. Petit et al.; NOAA Mauna Loa CO_2 record). 20

Figure 1.2. The schematic of carbon capture techniques [8, 9]. Copyright 2012 Wiley Online Library 22

Figure 1.3. The schematic of amine scrubbing unit [21]. 25

Figure 1.4. The schematic of Calcium Looping (CaL) process for post combustion CO_2 capture. 27

Figure 1.5. Sintering of CaO during carbonation/regeneration process. 32

Figure 1.6. Incorporation of metal oxide into CaO for sintering prevention. 32

Figure 2.1. Reactor setup schematic. a) The direction of gas through the sorbent. b) The ceramic sample holder dimension. 39

Figure 2.2. Experimental setup for testing CO_2 capture. 40

Figure 2.3. An example for phase quantification by Rietveld refinement. The X-ray diffraction data is related to CH0 after 20 min of carbonation under 20% CO_2 at 700 °C. 41

Figure 2.4. Phase evolution of $CaCO_3$ and CaO at 700 C under 20% CO_2 during carbonation of CH0. 42

Figure 2.5. Phase evolution of $CaCO_3$ and CaO at 700 C under 20% CO_2 during regeneration of CH0. 43

Figure 2.6. X-ray diffraction pattern of the intact sorbent and mechanically activated sorbents from commercial source. "#" marks denote the strongest peaks from $CaCO_3$. 46

Figure 2.7. SEM images of samples derived from commercial $Ca(OH)_2$: (a) CH0, (b) CH100, (c) CH300, and (d) CH500. 47

Figure 2.8. CaO conversion % as a function of time for sorbents without mechanical activation. Carbonation gas condition: 20 sccm CO_2 + 80 sccm N_2. Regeneration condition: 100 sccm pure N_2. Sorbent behavior of two different samples is shown: CH0 and homemade $Ca(OH)_2$. 50

Figure 2.9. Comparison of the CaO conversion % of the samples at different temperatures: (a) 650 °C, (b) 700 °C, and (c) 750 °C. The feed gas was 20% CO_2 in N_2. (d) Carbonation rate constant from the fast carbonation stage. Solid lines note values of CH0. 51

Figure 2.10. Comparison of the CaO recovery % of the samples at different temperatures: (a) 650 °C, (b) 700 °C, and (c) 750 °C. The feed gas was 100% N2. (d) Decarbonation rate constant from the fast decarbonation stage. Solid lines note values of CH0. (e–g) Recovery rate comparison for three temperatures. Two extreme cases are compared. All data points are from (a)–(c) plotted up to 30 min only. 54

Figure 2.11. (a) Comparison of the isothermal cycle stability between CH0 and CH500. (b) The first cycle. (c) The 10th cycle. 56

Figure 2.12. SEM images of the samples after 1 cycle and 10 cycles. (a) CH0 after one cycle. (b) CH0 after 10 cycles. (c) CH500 after 1 cycle. (d) CH500 after 10 cycles. 58

Figure 2.13. BET plot. a) Before any cycling (surface area of 71.7 m2/g for CH0 and 67.4 m2/g for CH500). b) After ten cycles (surface area of 24 m^2/g for CH0 and 30 m^2/g for CH500). 59

Figure 2.14. BJH pore size distribution up to 35 nm. (a) Before any cycling (surface area: 71.7 m^2/g for CH0 and 67.4 m^2/g for CH500). (b) After 10 cycles (surface area: 24 m^2/g for CH0 and 30 m^2/g for CH500). 59

Figure 2.15. Crystallite size at the end of each carbonation step. (a) $CaCO_3$. (b) CaO. This shows the sorbent microstructure during the 10 cycles right before each decarbonation/regeneration step. 61

Figure 2.16. End-of-cycle conversion % of each cycle fitted to the Grasa model. 62

Figure 3.1. The schematic of the sorbent synthesis. 69

Figure 3.2. XRD of calcium cobalt oxide at 800 °C (blue line) and 900 °C (red line). "•" indicates XRD peaks for $Ca_3Co_2O_6$. The peaks without any mark show $Ca_3Co_4O_9$ peaks.... 73

Figure 3.3.The X-ray diffraction patterns of the synthesized samples. The calcination temperature of all samples was 900 °C except $Ca_3Co_4O_9$. The calcination temperature of $Ca_3Co_4O_9$ was 800 °C. 74

Figure 3.4. Effect of heating rate on TPC-TPDC (CaO under 10% CO_2). a) CO_2 concentration during adsorption and desorption processes with different heating rates. b) Inversion temperature as function of heating rate. c, d, and e) Amount of CO_2 adsorption at 2, 5 and 10 °C/min respectively. 76

Figure 3.5. TPC-TPDC of CaO under 10% CO_2 in 90% N_2. The flow rate is 100 sccm in total. The heating rate was 5 °C/min. a) CO_2 concentration in the flue gas during carbonation and decarbonation process. b) Conversion of sorbent during the whole process. The sorbent conversion peaks at the inversion point. 78

Figure 3.6. Effect of initial $Ca(OH)_2$ content on TPC-TPDC behavior (10% CO_2 in nitrogen with heating rate at 5 °C/min). a) CO_2 concentration and humidity of the exhaust gas

during the temperature rise. b) Initial X-ray diffraction patterns of CaO. The "Fresh" scan is for CaO right after $Ca(OH)_2$ thermal decomposition. The "Aged" scan is for CaO after 1 day of exposure to ambient air at room temperature. 81

Figure 3.7. Back-to-back TPC-TPDC for CaO under 10% CO_2 and 5 °C/min heating rate. 82

Figure 3.8. TPC-TPDC under 4 different CO_2 levels: 5% (black), 10% (red), 15% (blue), and 20% (green). Heating rate was 5 °C/min for all. a) CaO, b) Ca_2CuO_3, c) $Ca_3Co_4O_9$ and d) $Ca_2Fe_2O_5$..... 83

Figure 3.9. Temperature profile as function of CO_2 concentration. a) Maximum carbonation rate temperature. b) Maximum decarbonation rate temperature, and c) the difference between the two temperatures. 86

Figure 3.10. Enthalpy from inversion temperatures for CaO, Ca_2CuO_3, $Ca_3Co_4O_9$ and $Ca_2Fe_2O_5$. 88

Figure 3.11. Final phases of different samples after cooling down under 10% CO_2. a) CaO, b) Ca_2CuO_3, c) $Ca_3Co_4O_9$ and d) $Ca_2Fe_2O_5$..... 89

Figure 3.12. Pore size distribution analyzed by density functional method. All samples were analyzed after the TPC-TPDC test. 90

Figure 3.13. Temperature swing carbonation/decarbonation kinetics comparison under 10% CO_2 for 6 cycles. a) CaO mass change rate. b) Ca_2CuO_3 mass change rate. One cycle was 60 minutes long: 10 min of carbonation at 700 °C, 20 min for heating up, 10 min of decarbonation at 800 °C, and 20 min for cooling down..... 91

Figure 3.14. Temperature swing carbonation/decarbonation kinetics comparison under 20% CO_2. a) CaO mass change rate. b) Ca_2CuO_3 mass change rate. The experiments were done between T_c and T_d of each sorbent. 93

Figure 3.15. Morphology changes of Ca_2CuO_3 and CaO sorbents after the temperature swing carbonation/decarbonation process. 96

Figure 4.1. X-ray diffraction patterns of the sorbents. Black, red, blue, and green are CaO, N-CCO, P-CCO, and F-CCO respectively. The symbols x, o and * indicate CaO, Cu, and Cu_2O accordingly. All the profiles were taken ex situ except the scan for the partially decomposed Ca_2CuO_3 (P-CCO) which was taken in situ. 107

Figure 4.2. Uniform distribution of Ca and Cu. Energy-dispersive X-ray spectroscopy (EDS) of a) N-CCO b) F-CCO. 109

Figure 4.3. Characterization of sorbents. a) Pore size distribution of N-CCO and F-CCO before any carbonation. b) Pore size distribution after ex-situ carbonation of N-CCO and F-CCO under pure CO_2 for 12 h at 800 °C. c) X-ray diffraction patterns of ex-situ carbonated N-CCO and F-CCO. 112

Figure 4.4. Carbonation behavior of the N-CCO and F-CCO under pure CO_2 from 300 °C (bottom scan) to 800 °C (top scan) with a 100 °C interval. a) N-CCO and b) F-CCO. c) Sorbent conversion with respect to temperature. Scanning after 26 min dwell. 13 min scan duration. Heating rate: 10 °C/min. 114

Figure 4.5. The composition of the sorbents under a carbonation condition as the temperature rises. a) N-CCO and b) F-CCO. 115

Figure 4.6. Regeneration behavior of the carbonated N-CCO and carbonated F-CCO from 300 °C (bottom scan) to 800 °C (top scan) with a 100 °C interval. a) N-CCO under pure air. b) F-CCO under 4% H_2 in N_2. c) Sorbent recovery with respect to temperature. Scanning after 26 min dwell. 13 min scan duration. Heating rate: 10 °C/min..... 117

Figure 4.7. The composition of the sorbents under a regeneration condition as the temperature rises. a) N-CCO and b) F-CCO. 118

Figure 4.8. The carbonation kinetics of the sorbents under pure CO_2 at 800 °C. a) N-CCO, b) P-CCO, c) F-CCO, and d) Sorbent conversion after each scan (scan duration: 13 min). 119

Figure 4.9. The composition of the sorbents during isothermal carbonation at the end of scans. a) N-CCO, b) P-CCO, and c) F-CCO. The carbonation temperature was 800 °C. ... 120

Figure 4.10. The regeneration kinetics of the sorbents under pure air (for N-CCO) and 4% H_2 (for P-CCO and F-CCO) at 800 °C. a) N-CCO, b) P-CCO, c) F-CCO, and d) Sorbent recovery after each scan (scan duration: 13 min). 121

Figure 4.11. The composition of the sorbents during isothermal regeneration at the end of scans. a) N-CCO, b) P-CCO, and c) F-CCO. The decarbonation temperature was 800 °C. 122

Figure 4.12. Stability analysis for the Ca_2CuO_3 series compared to CaO at 800 °C during 780 min (78 min for each cycle). Each point represents the end of carbonation after complete regeneration. a) Sorbent conversion trend when regenerated by air (CaO and N-CCO). b) Sorbent conversion trend when regenerated by 4% H_2 in N_2 (CaO, P-CCO and N-CCO). 125

Figure 4.13. Weight percentage of phases at the end of carbonation as the number of cycles increased. a) CaO, b) N-CCO, c) P-CCO, and d) F-CCO. 127

Figure 5.1. Temperature swing carbonation/decarbonation kinetics comparison under 20% CO_2. a) Ca_2CuO_3 powder change rate. b) Ca_2CuO_3 nanofiber mass change rate. The experiments were done between Tc (740 °C) and Td (850 °C) of each sorbent... 132

Figure 5.2. Surface area and pore size distribution of fresh Ca_2CuO_3 Powder and Ca_2CuO_3 nanofiber. 133

Figure 5.3. SEM Images of fresh Ca_2CuO_3 Powder and Ca_2CuO_3 nanofiber. 133

Figure 5.4. Electrospinning condition for synthesizing Ca_2CuO_3 nanofiber. 134

Figure 5.5. Comparison of F-CCO carbonation performance when 4% H_2 and pure N_2 were used as regeneration gas. 136

Figure 5.6. CO_2 conversion over time under 300 rpm ball milling when $Ca(OH)_2$ (1.1 g) was used as the sorbent. 138

Figure 5.7. Comparison of CO_2 conversion of CaO and $Ca(OH)_2$ (3 g) over time under 300 rpm ball milling. 140

List of Abbreviations

CCS carbon capture and storage

IPCC Intergovernmental Panel on Climate Change

MEA Monoethanolamine

SOX Sulphur oxides

NOX Nitrogen oxides

CaL Calcium Looping

XRD X-ray Diffraction

BET Brunner–Emmett–Teller

BHJ Barrett–Joyner–Hanelda

DLS Dynamic Light Scattering

SEM scanning electron microscopy

TGA Thermogravimetric analysis

N-CCO Non-decomposed calcium copper oxide

P-CCO Partially decomposed calcium copper oxide

F-CCO Fully decomposed calcium copper oxide

EDS Energy-dispersive X-ray spectroscopy

sccm standard cubic centimeters per minute

Chapter 1 Literature review

1.1 Introduction

As the earth warms, anthropogenic carbon emission mitigation strategy has emerged as a significant scientific focus. The reason for this is that the historic primary form of energy generation relied on the combustion of fossil fuels. However, this combustion necessitates release of CO_2 from said fuels. As the years progress and the climate continues to change, it becomes ever more clear that the primary greenhouse gas is CO_2 and that the release of CO_2 from fossil fuel combustion must be mitigated. It is very clear that an increase in carbon emissions leads to increased concentrations of CO_2 in the atmosphere and thus increased global temperatures. In fact, we can see an increase of 100 ppm in the atmosphere since pre-industrial times [1]. **Figure 1.1** clearly shows that the atmospheric level of CO_2 had never been above 300 ppm for millennia. However, since 1950 has been increasing significantly. Currently, the CO_2 level is reached 410 pm, which means an increase of 33% since the industrial revolution.

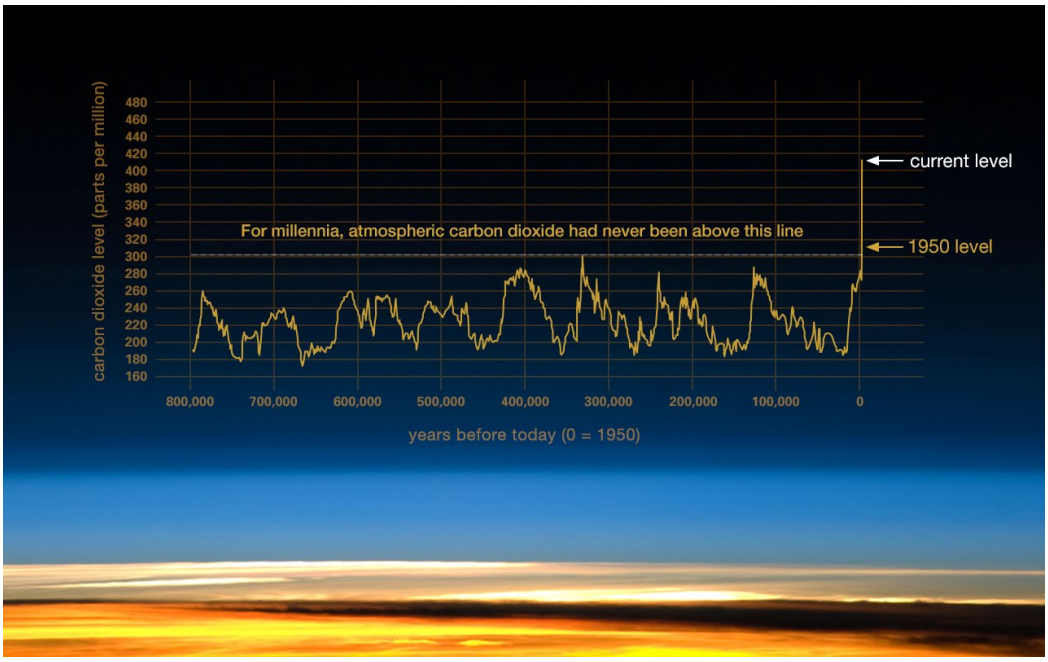

Figure 1.1. The level of carbon dioxide concentration throughout history. (Credit: Luthi, D., et al.. 2008; Etheridge, D.M., et al. 2010; Vostok ice core data/J.R. Petit et al.; NOAA Mauna Loa CO_2 record).

More than 75% of carbon emission from human activity is attributed to the combustion of fossil fuels. In addition, a significant amount of excess carbon and also the inability of nature to recapture carbon is due to chemical processing and deforestation [1]. According to the Intergovernmental Panel on Climate Change's 2022 report, the impact of increased greenhouse gasses from human activity has been observed to be severe. Humans experience a wide range of severe impacts from climate change, including but not limited to heat-related mortality, drought-related mortality, fatalities due to severe weather events, food and water insecurity, and irreversible damage to ecosystems throughout the world [2].

The IPCC found that, even in the near-term, the risks of the level of global warming reaching 1.5 °C are unacceptably high, particularly to vulnerable people and populations. Thus, urgent action is needed to stem the impacts of increased carbon emissions, of which one powerful tool is carbon emission elimination and reduction technology [2].

One way of mitigating climate change is to reduce or eliminate anthropogenic carbon emissions through Carbon Capture and Storage (CCS). Through this variety of technologies, carbon emitted from fossil fuel combustion can be separated and stored. This allows emissions to be stopped at the source and alleviates the pressure on the environment due to added carbon. From the analysis of a variety of assessments, it can be inferred that an 80-90% reduction of carbon emissions could be realized if a modern typical power plant implemented CCS. The carbon that is captured could be used in a number of ways. One of the most attractive ways would be to inject the stored carbon into oil reservoirs themselves. This effectively completes the loop of carbon capture and enhances the oil recovery process. This is just one of many options for storage, some of which are more feasible than others. The problem of what to do with the stored carbon is a subject that begs additional scientific attention. One option would be to convert the CO_2 into another compound that is useful to industry. Regardless, the CCS technology will inevitably add additional cost to the operation in which it is implemented. Therefore, it is critical that advances are consistently made in CCS technologies to make them economically feasible and efficient [1].

There are three main mechanisms of CCS: pre-combustion, oxy-fuel combustion, and post-combustion (**Figure 1.2**) [3-7]. Each of these mechanisms has benefits and disadvantages unique to the method. For every technology, one must consider its own economic favorability, health consideration, safety consideration, environmental consideration, and ability to scale. In addition, one must consider the reasonableness of utilizing the technology given the current state of

technology today. It must be considered that carbon emissions originate from a socio-industrial complex that has been built around fossil fuel combustion, and in such case necessitates the emission of CO_2. Therefore, a chief consideration must be made to the feasibility of utilizing such technology with the existing energy infrastructure today.

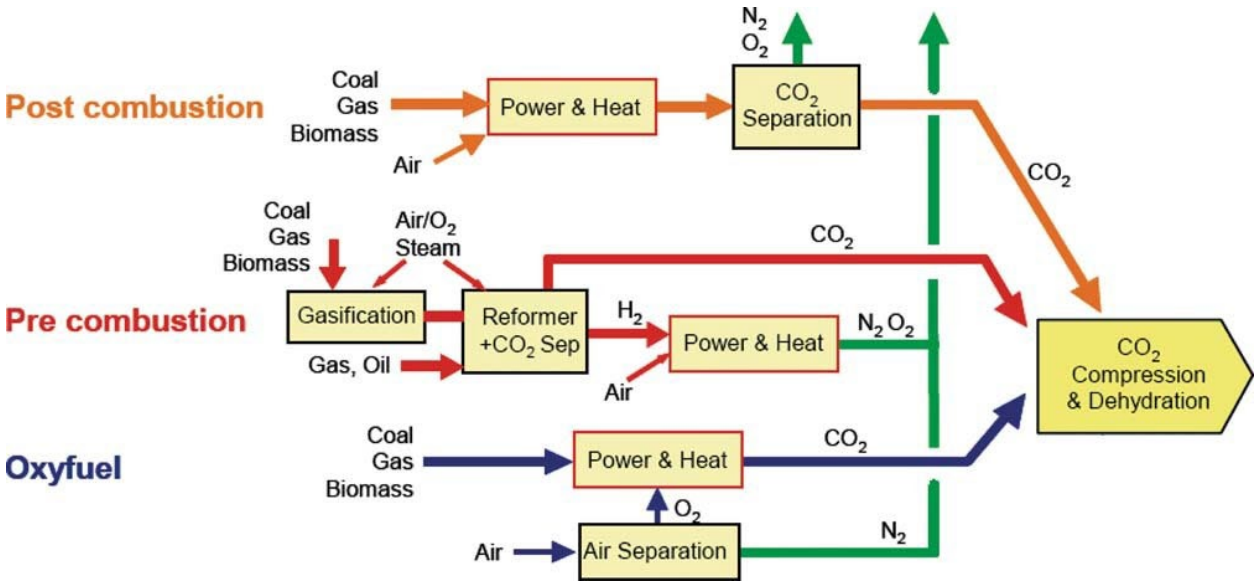

Figure 1.2. The schematic of carbon capture techniques [8, 9]. Copyright 2012 Wiley Online Library

1.1.1 Pre-combustion

Pre-combustion carbon capture takes place, naturally, before combustion. For this to occur, prior to entering a furnace, the fuel will be broken into CO_2 and H_2. The CO_2 is sequestered from the feed to the furnace, thus leaving the H_2-heavy fuel gas to enter the furnace and be burned [10]. This process consists syngas production and water-gas shift reaction. The two main pathways to produce syngas are steam reforming and gasification [10-14]

$$Steam\ reforming:\ CH_4 + H_2O \leftrightarrow CO + 3H_2 \quad (1-1)$$

$$Gasification:\ 2\,CH_4 + O_2 \leftrightarrow 2\,CO + 4H_2 \quad (1-2)$$

Through water-gas shift reaction [15-20] CO is converted to CO_2

$$CO + H_2O \leftrightarrow CO_2 + H_2 \quad (1-3)$$

Implementation of the technology requires the installation of a gasifier, which is typically only possible in facilities that are built new and less possible for retrofitting [21].

1.1.2 Oxy-fuel combustion

The second mechanism to consider is Oxy-fuel combustion. For systems employing this method, instead of air, the fuel will burn in the presence of oxygen. Therefore, the main combustion products that will be found in the flue gas will be CO_2 and H_2O [22-26]. This scheme achieves an easy removal of CO_2. Despite this, oxy-fuel combustion comes at a significant energy cost, as almost pure O_2 is necessary for the process and must be produced using air separation. Some types of this technology can be utilized in existing carbon-producers. However, it typically compromises the efficiency of the furnace and is thus less attractive for retrofitting and even new-built power plants [11, 27].

1.1.3 Post-combustion

The method that is most highly favored for research is post-combustion carbon capture because it can more easily be paired with existing technology through a retrofit process [1, 11, 28, 29]. In this process, the carbon is removed after combustion rather than before or during, as with

pre-combustion and oxy-fuel combustion. The carbon is removed using three main methods: membrane-assisted removal [30-32], amine scrubbing [21, 33, 34], and calcium looping [35-41]. The primary scheme for these methods involves removing CO_2 directly from the flue gas. In this way, different means of removal of CO_2 can be utilized and investigated separately.

The first method of carbon capture that we will consider is separation by selective membranes. This is a fairly new development in the research scene, and they have their own advantages and disadvantages. This separation method uses a selective membrane in the flue gas stream to eliminate CO_2 from the stream [25, 31]. An advantage of this process is that they do not take up much space and also are fairly simple to retrofit in a conventional power plant. However, the expense of the membranes stands as a barrier to the widespread adoption of this technology [1].

To accomplish CO_2 capture by amine scrubbing, one must use a solution of aqueous amines, as shown in **Figure 1.3**. In this arrangement, an amine solution in aqueous form is used to treat the flue gas. As this flue gas passes through the solution, it will absorb the CO_2 into the solution. A stripping column is then used to remove the CO_2 from the solution. However, this process does require heat, which can be sourced from the excess steam from the plant's furnace steam cycle. When CO_2 is stripped from the solution, it can then be subjected to additional processes, such as sequestration, to prepare for transportation. Although many amines are suitable for this, the most commonly used and studied amine is monoethanolamine (MEA) [21, 42, 43]. Although this process is widely studied and useful for industry, many problems present significant challenges to its adoption. First, amines tend to degrade under high temperatures, which might require an additional cooling step for the flue gas depending on the amine used. In addition, amines themselves present environmental risks. SO_X and NO_X emissions can lead to flue gas poisoning.

The aqueous amine solution can be toxic and corrosive. If this solution is released into the environment, it could lead to serious consequences. Even without release, the corrosive nature of amine solutions can lead to compromised equipment integrity, increasing the risk of inadvertent emissions and surely increasing the requirement and cost of maintenance. Amines themselves are expensive, which impacts the cost vs. benefit analysis. Additional cost can be incurred because amines are volatile and can be lost through traps or aerosolized and lost to off gasses in the process and further pollute the environment. Because amines break down under high temperatures, there are even higher potentials for emissions and the need for makeup solutions, thus increasing the cost. In addition, when an amine oxidizes, other compounds such as amides, organic acids, or ammonia will result. If the degradation occurs due to thermal conditions, then the effectiveness of carbon capture capacity will also degrade in addition to producing resulting compounds that are even more corrosive and toxic to the environment than the original amine solution. This will lead to additional makeup amine solution, equipment breakdown, and maintenance due to corrosion, and environmental emission controls, which further diminishes the economic favorability [1, 21].

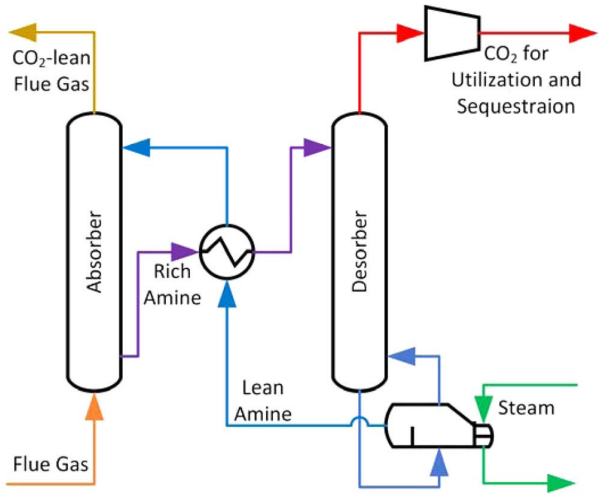

Figure 1.3. The schematic of amine scrubbing unit [21]. Copyright 2015 American Chemical Society

1.1.3.1 Calcium Looping process

The most favorable process that can be used to capture CO_2 post-combustion is calcium looping (CaL) [35-37, 39, 40, 44]. The method is based on the carbonation of CaO. One of the biggest attractions of this material is its low cost. Natural CaO is readily available as limestone. The following reversible reaction describes the carbonation and regeneration of the sorbent.

$$CaO(s) + CO_2(g) \rightarrow CaCO_3\,(s) \qquad (1-4)$$

The schematic of the CaL process is shown in **Figure 1.4**. After burning fossil fuel for the power generation, Instead of releasing the flue gas into atmosphere, it will introduce to a fluidized bed reactor for the carbonation process. The CaO-based sorbent in the reactor captures CO_2 by the carbonation. In this process, CaO turns into $CaCO_3$ and the clean gas, free of CO_2, leaves the reactor. The $CaCO_3$ will transfer to another fluidized bed reactor for the CO_2 collection and the sorbent regeneration. The regenerated sorbent travels to carbonator reactor for the new carbonation process.

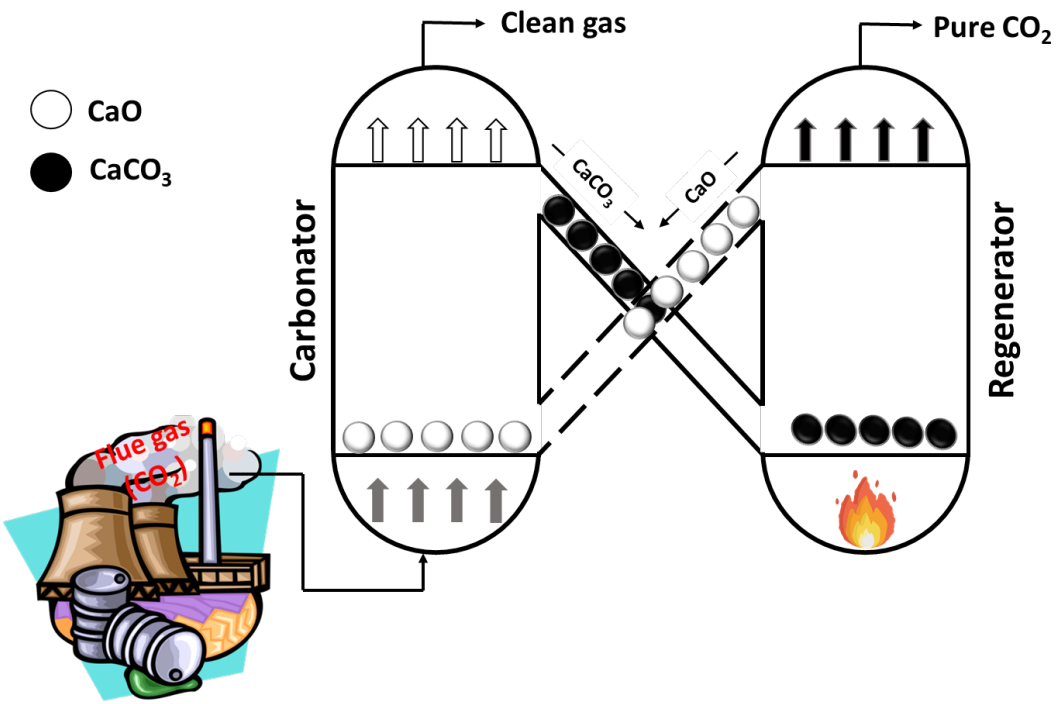

Figure 1.4. The schematic of Calcium Looping (CaL) process for post combustion CO_2 capture.

The CaL can be done by temperature or pressure swing carbonation/decarbonation. In temperature swing process, the typical carbonation temperature is 650 °C, while the regeneration occurs at 900-950 °C [40]. This high temperature is necessary since the regeneration is done under pure CO_2 at atmospheric pressure. In pressure swing adsorption, the carbonation and regeneration are done at a constant temperature (650 °C). In order to overcome the thermodynamic barrier for $CaCO_3$ decomposition, we need to lower the CO_2 pressure in the regeneration reactor. This can be done by introducing steam to the reactor or using a vacuum pump to depressurize the reactor pressure [41, 45].

1.1.3.2 Models for CaO carbonation

Like any other solid-gas reaction, the carbonation of CaO under CO_2 also has two stages. The fast and slow stages which are controlled by chemical reaction and diffusion. For the former can be modeled by intrinsic reaction rate, while the latter can be described by the apparent model [46].

The intrinsic rate of CaO-CO_2 can be described by grain model [47]. This model can be expressed as follow,

$$R = \frac{dX}{dt(1 - X(t))^{2/3}} = 3r \qquad (1-5)$$

where R, r, X, and t are reaction rate, grain model reaction rate, conversion, and reaction time . Taking the integration of the equation above,

$$1 - \left(1 - X(t)\right)^{\frac{1}{3}} = r \times t \qquad (1-6)$$

the constant reaction rate can be obtained by plotting $1 - \left(1 - X(t)\right)^{\frac{1}{3}}$ versus t.

The apparent model was proposed by Lee [48]for the slow stage of CaO carbonation. The model can be simplified as the following equation,

$$X(t) = \frac{X_u t}{\left({X_u}/{k}\right) + t} \qquad (1-7)$$

where X_u is the ultimate conversion of CaO, and k is the reaction constant rate. Considering the time that half of the ultimate conversion can be achieved (τ)

$$X_u = k\tau \qquad (1-8)$$

Combining the equation 1-7 and 1-8,

$$X(t) = \frac{k\tau t}{\tau + t} \qquad (1-9)$$

τ and k can be calculated by using the linear form or equation above,

$$\frac{1}{X(t)} = \frac{1}{k}\left(\frac{1}{t}\right) + \frac{1}{k\tau} \qquad (1-10)$$

This model does not take morphological parameters into account.

The activation energy (E) can be calculated by the Arrhenius equation,

$$\ln(k) = -\frac{E}{R}\left(\frac{1}{T}\right) + lnA \qquad (1-11)$$

1.1.3.2.1 The grain model

For CaO carbonation, CO_2 needs to diffuse from gas bulk to porous pellet surface and then into the pellet. The mass balance equation for CO_2 around CaO pellet with the following assumption:

- A porous CaO pellet contains lots of grains
- Pellets have cylindrical geometry
- Grains are nonporous and have spherical geometry
- The porosity is time-depended
- Diffusivity of gas changes with the product layer around the grain,

can be written as follow

$$\frac{\partial(\varepsilon C_{CO_2})}{\partial t} = \frac{1}{r}\frac{\partial}{\partial r}\left(r\, D_e \frac{\partial C_{CO_2}}{\partial r}\right) + 3\frac{(1-\varepsilon_0) r_c^2}{r_0^3}\, S \qquad (1-12)$$

with initial condition and boundary conditions

$$C_{co_2}(t=0) = C_{CO_2,0} \qquad (1-13)$$

$$\frac{\partial C_{co_2}}{\partial r}(r=0) = 0 \qquad (1-14)$$

$$D_e \frac{\partial C_{co_2}}{\partial r}\left(r = r_p\right) = k_c\left(C_{CO_2,b} - C_{CO_{2,s}}\right) \qquad (1-15)$$

where $\varepsilon, C_{CO_2}, r, D_e, r_c, r_0, and\ S$ are pellet porosity, CO_2 concentration, radius pellet, effective diffusivity, radial position of the reaction, initial radius of the grains, and surface reaction rate.

The mass balance of CaO grain is

$$\frac{dr_c}{dt} = \frac{M_{CaO}}{\rho_{CaO}} S \qquad (1-16)$$

with initial condition of,

$$r_c(t=0) = r_0 \qquad (1-17)$$

where ρ_{CaO} and M_{CaO} are density and molecular weight of CaO.

The first-order surface reaction can be expressed as follow,

$$S = kC_{CO_2} \qquad (1-18)$$

$$k = k_0 e^{-E/RT} \qquad (1-19)$$

The porosity of CaO varies by grain radius and the effective diffusion coefficient varies by porosity

$$\varepsilon = 1 - (1 - \varepsilon_0)\left(\frac{r_g}{r_0}\right)^3 \qquad (1-20)$$

$$D_e = D_{e0}\left(\frac{\varepsilon}{\varepsilon_0}\right)^2 \qquad (1-21)$$

This model was proposed by Khoshandam et al [49].

1.1.3.3 Deactivation of CaO in the Calcium Looping process

Despite the advantages of CaO for CO_2 capturing at high temperatures. The activity of the sorbent decrease with the increase of the cycle due to sintering, as shown in **Figure 1.5**. When CO_2 (in flue gas) contacts with fresh CaO, the carbonation occurs and layers of $CaCO_3$ form around the sorbent. The carbonated sorbent will be heated to regenerate. Due to the high temperature, the sorbent losses its surface area and pore structure, and sintering happens. A number of study has been done on the deactivation and different model has been proposed [50-52] .Wang and Anthony proposed a second-order deactivation rate through sintering [51],

$$X_N = \frac{1}{1+kN} \qquad (1-22)$$

where k, N, and X_N, are deactivation constant, the number of cycles, and conversion of CaO at N^{th} cycle.

Grasa and Abanades found residual conversion on a large number of cycles. This conversion remains constant after 50 cycles [52]. They modeled deactivation based on the second-order with residual conversion consideration.

$$X_N = \frac{1}{\frac{1}{1-X_r}+kN} + X_r \qquad (1-23)$$

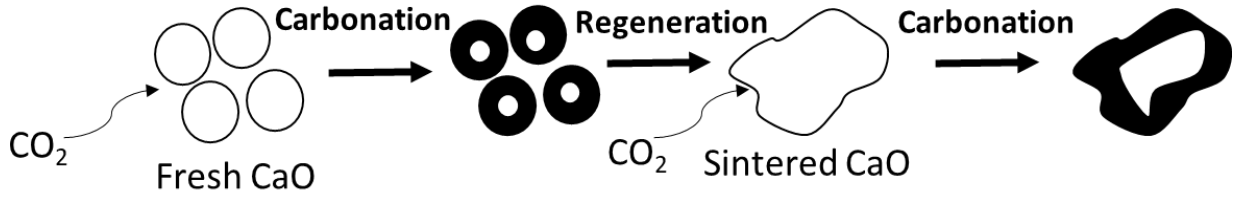

Figure 1.5. Sintering of CaO during carbonation/regeneration process.

A large number of studies have been done on sintering prevention of CaO [9, 28, 29, 53-58]. The incorporation of metal oxide into CaO considers as one of the effective methods to prevent the sintering of this sorbent (**Figure 1.6**). Metal oxide as an inert phase with a high melting point, provides the scaffold for the sorbent. As a result, the pore structure remains, therefore sintering of the sorbent delays.

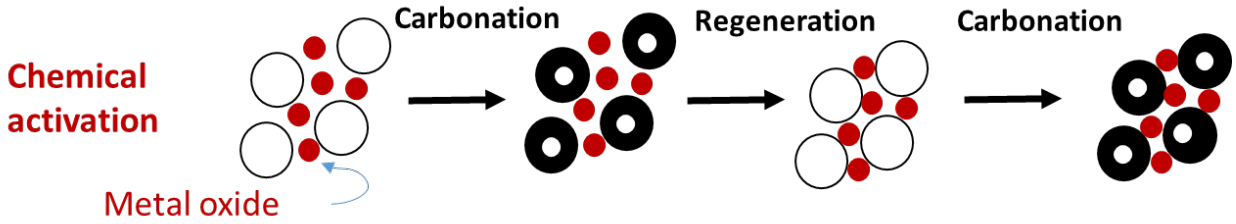

Figure 1.6. Incorporation of metal oxide into CaO for sintering prevention.

Chapter 2 Carbonation, regeneration, and cycle stability of the mechanically activated $Ca(OH)_2$ sorbents for CO_2 capture: An in situ X-ray diffraction study

Abstract

The impact of mechanical activation on calcium hydroxide-based sorbent was investigated. Carbonation/decarbonation kinetics and sorbent cycle stability were characterized by in situ X-ray diffraction. By increasing the speed of ball milling, we could reduce the particle size and crystallite size while increasing the pore volume in the sorbent as evidenced by XRD, dynamic light scattering, and nitrogen physisorption. At 700 °C, mechanically activated (500 rpm planetary ball milled) sorbent showed a 24% increase in capture capacity over 10 isothermal carbonation–regeneration cycles when compared to the sorbent without mechanical activation. The possible reason behind this improvement is discussed, which links the microstructure evolution and sorbent regeneration rate.

2.1 Introduction

Anthropogenic carbon emission has a clear impact on the climate. As greenhouse gas emissions are at a historic high, unprecedented action is required to ensure the planet's habitability. So far, entire industrial systems have been developed on the combustion of fossil fuels. 78% of the increase in greenhouse gas emissions during the period from 1970 to 2010 can be attributed to industrial process pollution and fossil fuel combustion [59]. A long-term solution would be to drive the whole industry solely by renewable energy, although that would require an overhaul of infrastructure. It is imperative to mitigate carbon emission now until this big change is realized. Because of the mounting concerns over climate change, a large effort has been made by the

scientific community to develop affordable methods of Carbon Capture and Storage (CCS) [60-62].

Amine scrubbing has been widely studied and employed to reduce the carbon release from fossil fuel combustion [21]. Unfortunately, this technology has some challenges that make it less efficient than desired [38]. Its regeneration process is very energy-intensive [63]. Furthermore, degradation of solvents over time [64, 65] and equipment corrosion due to the solvent itself [66, 67] hurt the economic applicability of this technology.

A potentially favorable option for CO_2 capture is calcium looping (CaL). The first investigation of CaL by an academic endeavor was in 1999 by Shimizu et al [68]. This method is based on a reversible reaction: carbonation and decarbonation of calcium oxide. The carbonation reaction is written as follows:

$$CaO(s) + CO_2(g) \rightarrow CaCO_3\,(s) \qquad \Delta H = -178\,kJ/mol \qquad (2-1)$$

The carbonation reaction is an exothermic reaction; therefore, lower temperature is thermodynamically favorable. However, if the temperature is too low, the reaction is not facile enough. On the other hand, decarbonation, commonly called regeneration, is an endothermic reaction. Higher temperature is suitable when considering thermodynamics and kinetics of decarbonation. Still, due to energy cost, one would want to provide as small of an amount of heat as possible to drive the decarbonation reaction. To accommodate the thermodynamic and kinetic requirements, the commonly chosen temperatures are 650 °C for carbonation and 950 °C for regeneration [69]. Recently, Yin et al. [41, 45]proposed performing the carbonation/regeneration process at a constant temperature. This process can be carried out by depressurization or steam dilution to provide a thermodynamic driving force for the regeneration reaction (decreasing the

partial pressure of CO_2 in the gas phase). Isothermal carbonation/regeneration cycles can cut down the process cost remarkably [41].

Calcium looping technology offers favorable characteristics for industrial use. Limestone, the primary source of calcium oxide in CaL scheme, is abundant, inexpensive, and environmentally benign [38]. Furthermore, the theoretical CO_2 capture capacity of CaO is decently high (0.78 g CO_2/g CaO) when one assumes one gaseous molecule of CO_2 bound to a CaO formula unit.

The efficiency of the process remains relatively high when coupled with a combustion process. The efficiency penalty for the overall process is 6.7–7.9% [38, 63] as compared to no CO_2 capture at all. More importantly, the cost of CO_2 capture by calcium looping has been estimated to be about 50% less than that by amine scrubbing, which amounts to 29 USD per ton of CO_2 capture through calcium looping [58].

Despite all of the advantages of calcium looping, CaL technology suffers from a decrease in the reactivity of sorbents as the number of carbonation–decarbonation cycles increases [70, 71]. The efficiency is mainly deteriorated by sintering [38]. When the solid sorbent sinters to minimize surface energy, a change in the microstructure of the material, pore shrinkage or grain growth, takes place. Because sintering takes place by diffusion, a thermally activated process, a high decarbonation temperature will surely aggravate the cycle stability [53]. Sorbents are also susceptible to fragmentation by thermal and mechanical stresses [38].

One strategy to strengthen sorbent robustness is to use the synthesized sorbent apart from naturally occurring limestone. In this case, the sorbent synthesis cost needs to be considered for real application. A balance must be found between the synthesis/materials' cost and the performance enhancement. Various chemical and mechanical methods were adopted for sorbent

preparation. Precipitation, hydration, acid modification, carbon coating, incorporating inert supports, and the synthesis of CaO hollow microspheres have been applied to chemically activate the calcium-based sorbent [72-77]. On the other hand, the sorbent can also be mechanically activated through dry ball milling, wet ball milling, and sound wave pulses [78-82]. Among these sorbent activation schemes, wet ball milling is a simple and efficient way to increase the performance of the sorbent for CO_2 capture.

Sayyah et al. [80] investigated the effect of vibratory, dry planetary, and wet planetary milling on the performance of CaO-based sorbents for CO_2 capture. They found wet planetary milling was the most effective in attaining sorbent stability over 50 cycles of carbonation–regeneration. Sun et al. [81] varied the ball milling time to see the impact on sorbent cyclability enhancement. In their study, it was found the increasing the time of ball milling increased the CO_2 uptake by producing finer particles. The capture capacity of the sorbent increased by 30%. Interestingly, ball milling treatment had an optimum duration such that excess ball milling causes particle agglomeration while short time ball milling is not adequate for grinding down the sample.

Despite the known effectiveness of ball milling for increasing the performance of the sorbent for CO_2 capture, the effect of ball milling on the kinetics of the carbonation and regeneration reaction has not been thoroughly studied. This work focuses on the mechanical sorbent modification and temperature-dependent behavior of such processed sorbents for CO_2 capture. Carbonation–decarbonation kinetics and sorbent cyclability were investigated by in situ X-ray diffraction.

2.2 Experimental section

2.2.1 Sorbent preparation

$Ca(OH)_2$ from Sigma-Aldrich with 95% purity, without any treatment, was used to prepare the samples using a planetary ball mill (PQ-N_2 Across International). The X-ray diffraction (XRD) pattern of the commercial $Ca(OH)_2$ sample straight from the bottle showed a small amount of $CaCO_3$. One gram of commercial $Ca(OH)_2$ and 6 mm diameter grinding alumina balls (~480 counts) were put into an alumina jar first. Next, 10 mL of ethanol was added to it. Three different speeds, 100, 300, and 500 rpm, were chosen for $Ca(OH)_2$ activation. After ball milling was performed for 3 h, to collect the sample, the ceramic jars were washed out with ethanol to fill the centrifuge tubes. After that, the tubes were centrifuged at 3000 rpm for 10 min (Heraeus Megafuge 16 Centrifuge, Thermofisher Scientific). In the end, milled $Ca(OH)_2$ was dried at 70 °C in air overnight. The samples were named after the speed of rotation, rpm (rotation per minute). CH100 means 100 rpm milling, for instance. CH0 means that the sample was not milled. We also made $Ca(OH)_2$ crystals in the laboratory by reacting calcium nitrate with KOH in water to have a sorbent with a big crystallite size and a low surface area. KNO_3, the byproduct of the reaction, was washed away with deionized water after reaction. We did not mechanically activate this homemade sorbent.

The dried samples were characterized by XRD, BET, dynamic light scattering (DLS), and scanning electron microscopy (SEM). The XRD was taken by Cu Kα radiation (λ = 1.5418 Å) from an AXRD powder diffraction system (Proto manufacturing). The samples were scanned at a rate of 2.4°/min (Δ2θ = 0.0140°, dwell time = 2 s) from 20° to 80° (2θ) at 30 mA and 40 kV. The surface area and pore volume of samples were analyzed through nitrogen physisorption using a Quantachrome autosorb iQ BET (Brunner–Emmett–Teller) setup. After being degassed at 300 °C under vacuum for 3 h, the sorbent surface area was calculated by the multipoint BET method, and

the pore volume was calculated by the BHJ (Barrett–Joyner–Hanelda) method from the desorption branch of the isotherms. Zetasizer Nano ZS (Malvern Instrument) was used to determine the sorbent particle size by DLS. A small amount of sample was dispersed in 1 mL of water, and the solution was shaken by a vortex mixer for 1 min to get well-dispersed particles. The morphology of the samples was studied by a scanning electron microscope (JEOL JSM-7000F). Because the samples were not electrically conductive, the samples were coated with a thin layer of gold.

2.2.2 CO_2 capture test

Traditionally, thermogravimetric analysis (TGA) has been the main tool to study the CO_2 capture ability of inorganic sorbents. The weight change is recorded as a function of time under controlled gas atmosphere. However, TGA results change on the basis of how much mass is used [83, 84]. This is because of the flow geometry of TGA. Because gas passes over the sample, an undesired effect of insufficient mass transfer may be present [85]. This complication can be ruled out in our in situ XRD setup because the gas flows through the thickness direction of the powder bed similar to a packed bed configuration (**Figure 2.1**). A high gas flow rate also tends to interfere with precise TGA analysis [86]. In the current in situ XRD setup, we can flow up to 300 sccm of the carbonation/decarbonation gas through the powder bed without a problem. These advantages make the current in situ XRD coupled with Rietveld refinement an attractive alternative to TGA for carbonation/decarbonation kinetics study.

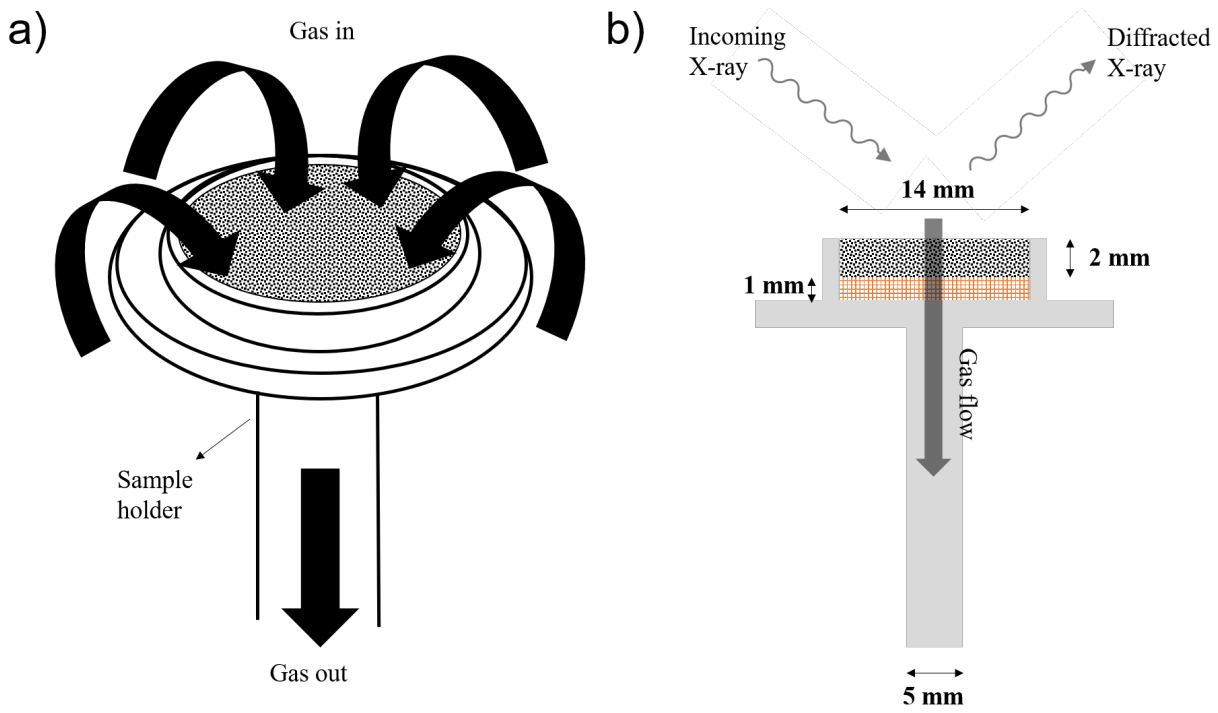

Figure 2.1. Reactor setup schematic. a) The direction of gas through the sorbent. b) The ceramic sample holder dimension.

0.1 g of each sample was loaded on the ceramic sample holder with 14 mm diameter and 3 mm depth (including 1 mm ceramic sieve and 2 mm for sample), which was designed for the XRK 900 (Anton Paar) reactor (**Figure 2.1**). N_2 and CO_2 gas tanks were connected to the reactor, and they were controlled by mass flow controllers (MKS G series). Next, 20 sccm of CO_2 and 80 sccm of N_2 were used for the carbonation process (**Figure 2.2**). It should be noted that, in all cases, the prepared $Ca(OH)_2$ is completely converted to CaO before the carbonation process proceeds. The sample was heated in N_2 to a high temperature (650, 700, and 750 °C) with a 10 °C/min ramping rate and was kept at the preset temperature for 1 h before the first X-ray pattern was taken. This converts all $Ca(OH)_2$ into CaO before carbonation. Because the carbonation reaction is fast,

we took snapshots of X-ray patterns using the X-ray detector that can, at a fixed position, cover 10° in 2θ. The signal integration time for each snap was 10 s. Back-to-back snapshots were taken to monitor carbonation with a high enough time resolution. The 2θ range for pattern collection was from 29.1° to 38.1°. The most intense X-ray diffraction peaks for CaO (2θ = 37.45°) and $CaCO_3$ (2θ = 29.47°) are within this range, which leads to reliable quantification results from Rietveld refinement. The regeneration (decarbonation) process was conducted under 100 sccm of pure N_2.

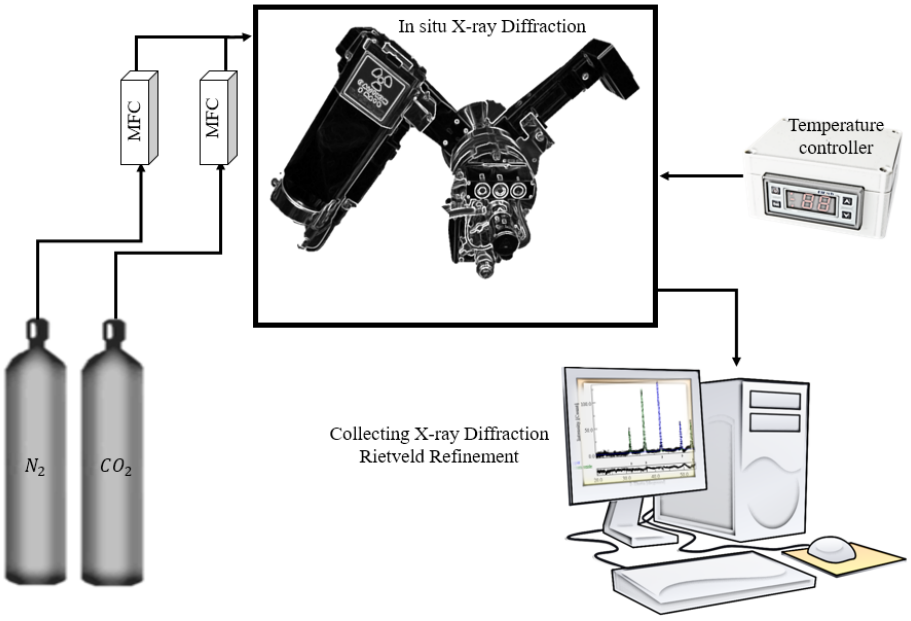

Figure 2.2. Experimental setup for testing CO_2 capture.

After all of the X-ray diffraction pattern snapshots were collected with a 10 s time resolution, the Rietveld refinement was done by MAUD software to identify the composition of phases, and then conversion of CaO to $CaCO_3$ was calculated as follows [81]:

$$Conversion\% = \frac{CaCO_3\ weight\ fraction}{CaCO_3\ weight\ fraction + CaO\ weight\ fraction \times \frac{MW_{CaCO_3}}{MW_{CaO}}} \times 100 \quad (2-2)$$

An illustration of Rietveld refinement can be seen in **Figure 2.3**. The blue line shows the calculated $CaCO_3$ phase, the red line depicts the calculated CaO phase and the "*" shows the experimental data points which is reduced for the sake of better illustration (for the phase calculation we used whole data set points).

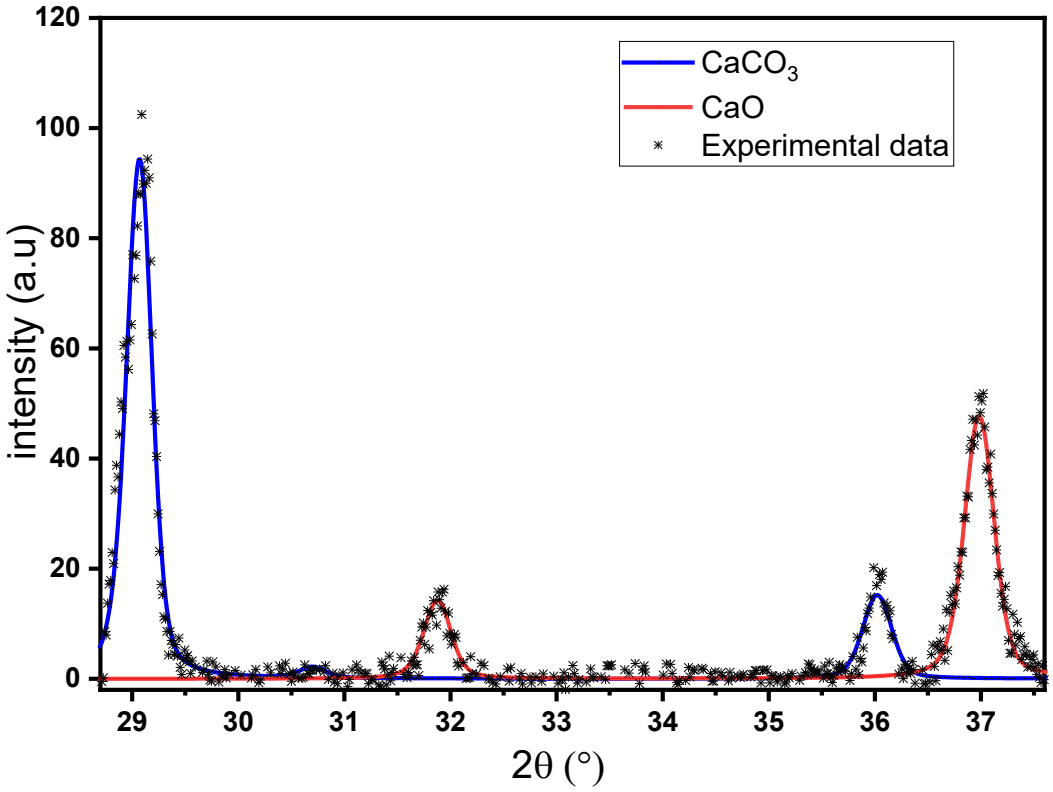

Figure 2.3. An example for phase quantification by Rietveld refinement. The X-ray diffraction data is related to CH0 after 20 min of carbonation under 20% CO_2 at 700 °C.

Figure 2.4 shows a set of selected data that indicates the phase evolution of the sorbent during carbonation process. The peaks around 29° and 36° are related to $CaCO_3$ and the peaks around 32° and 37° are related to CaO. The increase in $CaCO_3$ phase and decrease in CaO phase is visible. The data on graph was computed data by Rietveld refinement. Each Scan was programed

to be taken after 1 min however, due to limitation of the X-ray instrument taken time is a little bit different from the programmed time. The real time is attached to the scan number on the graph.

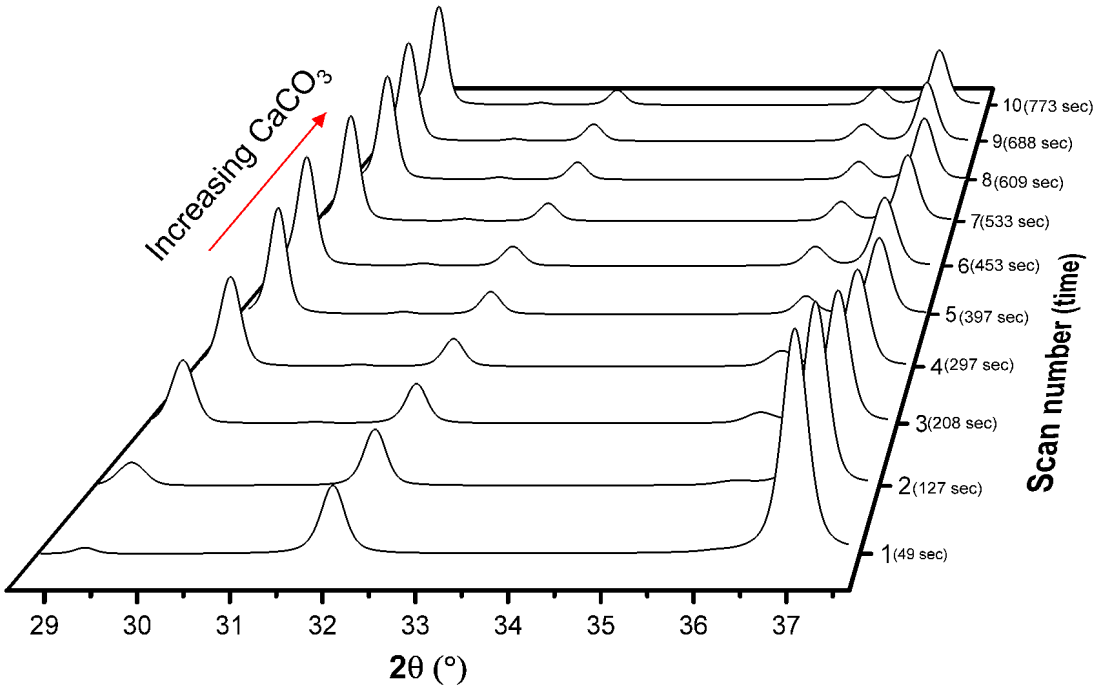

Figure 2.4. Phase evolution of $CaCO_3$ and CaO at 700 C under 20% CO_2 during carbonation of CH0.

Figure 2.5 shows a set of selected data that indicates the phase evolution of the sorbent during regeneration process. The decrease in $CaCO_3$ phase (peaks around 29° and 36°) and increase in CaO phase (peaks around 32° and 37°) is visible

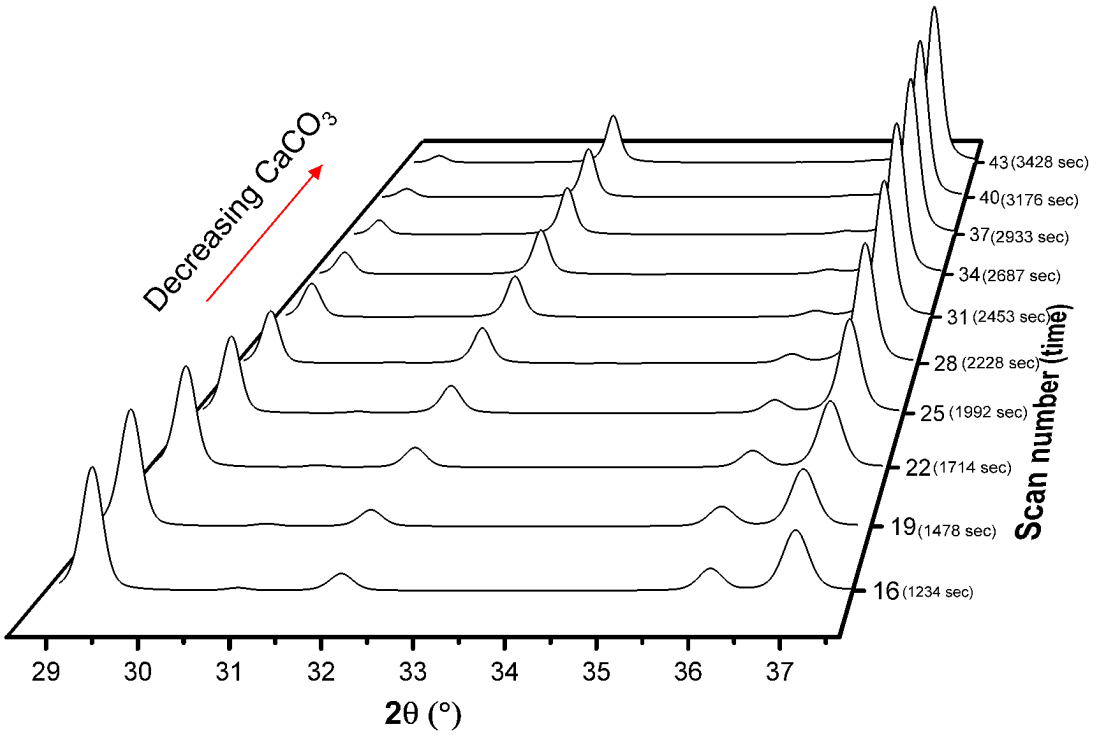

Figure 2.5. Phase evolution of $CaCO_3$ and CaO at 700 C under 20% CO_2 during regeneration of CH0.

Even though carbonation steps were followed by regeneration steps in all cases, for a simpler presentation, we will talk about carbonation and regeneration separately when needed.

The cycle stability of sample was tested at 700 °C during 10 cycles. Each cycle took 1 hour including 20 min of carbonation and 40 min of regeneration. For gas transition during each cycle, gas flow rates were controlled using Labview software. After the high temperature reaction, the sorbent was cooled down under pure N_2. Rate constants were calculated from linear fitting of the kinetics data in the fast reacting region.

2.3 Results and discussion

2.3.1 Sorbent characterization

Table 2.1 lists the BET surface area and the BJH pore volume of the three mechanically activated $Ca(OH)_2$ samples and the two intact samples. The surface area was in general increased by raising the ball milling speed except for CH500, the most harshly treated one. We can find a similar trend when the ball milling time was controlled [78]. This can be explained by the propensity of small particles toward agglomeration. The maximum surface area found was 27% higher than that for the intact sample, CH0. Even though the surface area change is moderate across the tested sorbents, the pore volume increased significantly by milling speed control. CH500 has more than 3 times the pore volume as compared to the intact one. Sorbent pore structure has been known to influence the carbonation kinetics [87].

Table 2.1. Samples characterization: BET, X-ray diffraction, and dynamic light scattering analysis.

	Surface area [a] (m^2/g)	Pore [b] volume (cc/g)	Crystal size [c] (XRD) (nm)	Unit cell [d] (XRD) ($Å^3$)	Microstrain [e] (XRD)	Particle size [f] (DLS) (nm)
Homemade	22.5	0.048	148	55.08	13.3×10^{-4}	--
CH0	71.7	0.199	36.5	54.86	8.75×10^{-4}	--
CH100	74.9	0.148	34.6	54.88	7.98×10^{-4}	239
CH300	91.3	0.260	32.2	54.76	7.75×10^{-4}	92
CH500	67.4	0.610	26.8	54.91	6.76×10^{-4}	75

[a]BET theory.
[b]BJH theory.
[c]Rietveld refinement.
[d]Rietveld refinement.
[e]Williamson–Hall plot.
[f]Mie theory.

XRD, SEM, BET, and DLS experiments were conducted on the mechanically activated sorbents to better understand the impact of ball milling on $Ca(OH)_2$ microstructure. Samples without ball milling were not analyzed by DLS. The XRD patterns of the samples are shown in **Figure 2.6**. The results show that ball milling did not induce detectable phase change. The adventitious $CaCO_3$ peaks appear in all the samples as an impurity phase in $Ca(OH)_2$. By doing Rietveld refinement on all data set, it was found that all samples contain around 5 ± 2 weight percent of $CaCO_3$. Rietveld refinement also shows increasing RPM of ball milling reduces the

crystallite size of the samples (**Table 2.1**). The particle size was measured by DLS. It should be noted that DLS in this work looks at only the smallest particles in the particle mixture. We shake up and break agglomerated particles before DLS, but real sorbent samples include agglomerated particles. The DLS results clearly show that we get smaller particle size from higher speed of ball milling.

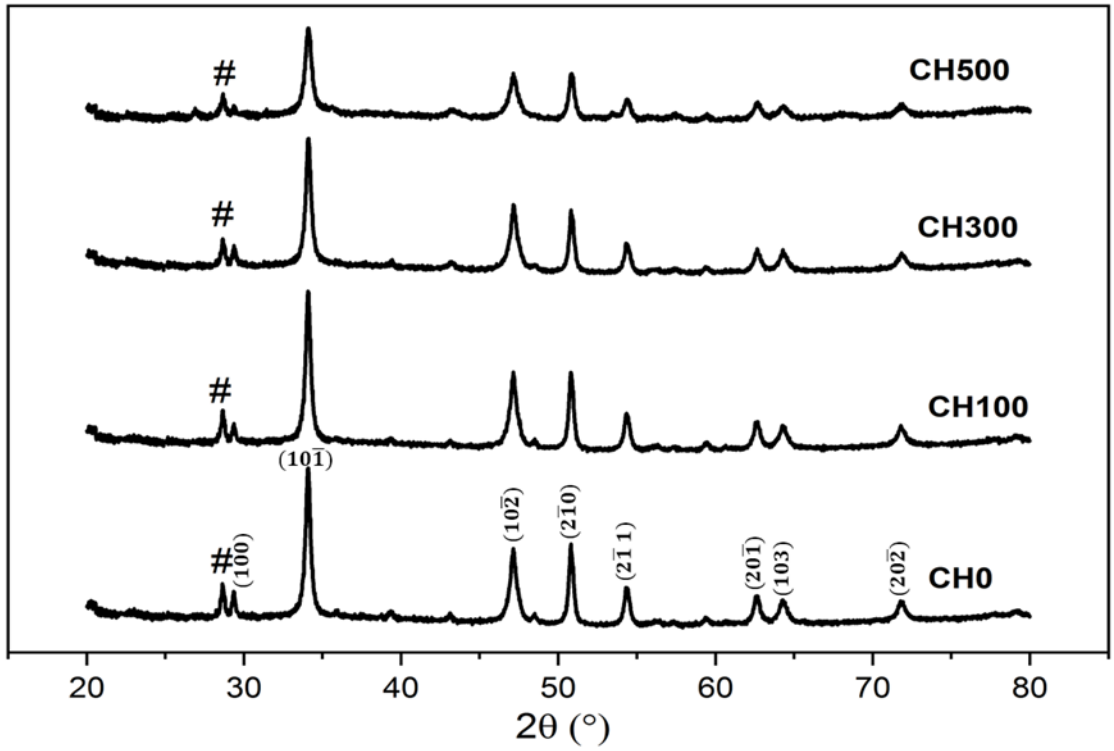

.

Figure 2.6. X-ray diffraction pattern of the intact sorbent and mechanically activated sorbents from commercial source. "#" marks denote the strongest peaks from $CaCO_3$.

Scanning electron microscopy (SEM) images were collected to investigate the effect of ball milling on the morphology of the sample. **Figure 2.7** shows the images from CH0, CH100,

CH300, and CH500. Images of CH0 and CH100 show that the change in particle size is not significant with this low speed milling. Once the rpm increases to 300, small particles clearly form through the breakage of bigger particles (**Figure 2.7c**). For CH500, the sample with the most severe milling condition, the particle size decreased significantly; however, one can also see the agglomeration of small particles (**Figure 2.7d**).

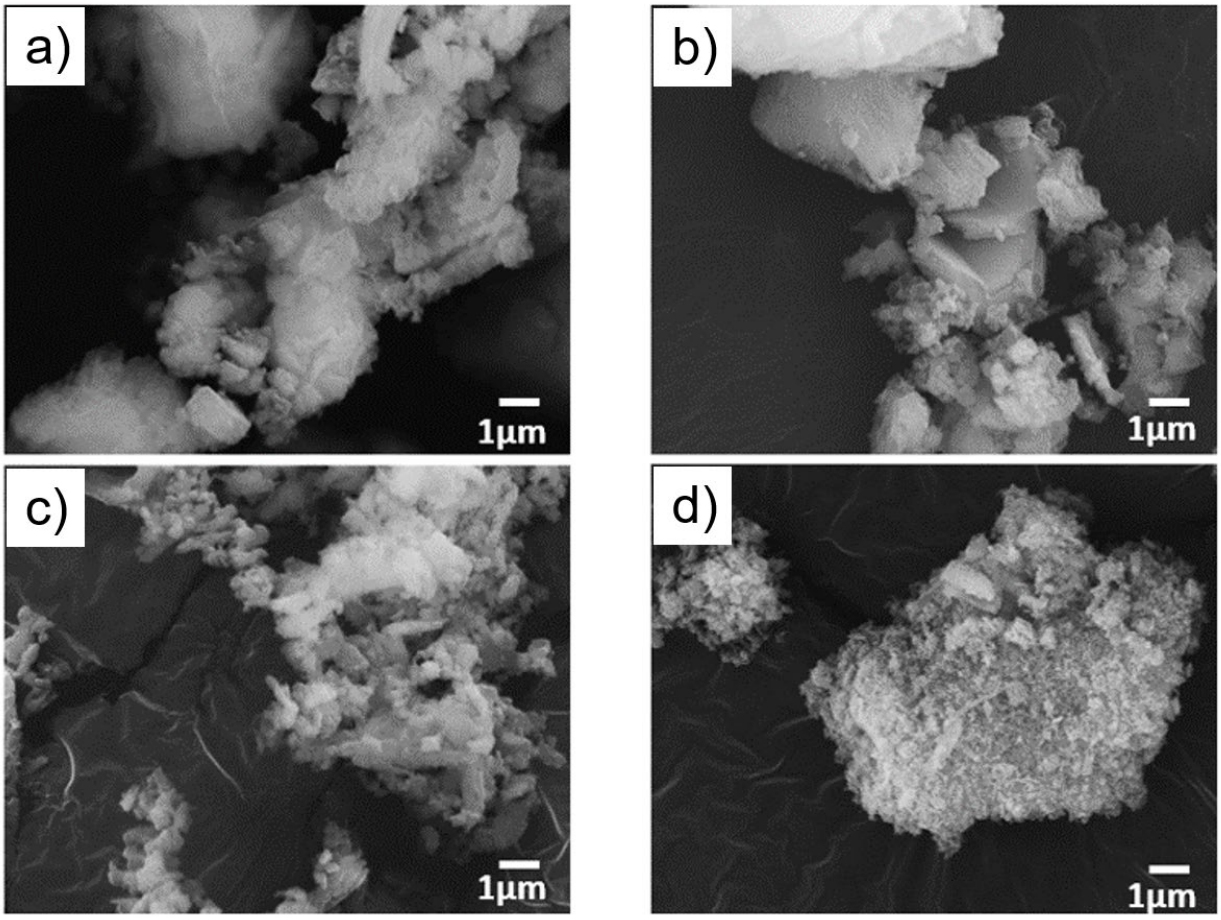

Figure 2.7. SEM images of samples derived from commercial $Ca(OH)_2$: (a) CH0, (b) CH100, (c) CH300, and (d) CH500.

2.3.2 Carbonation/regeneration of sorbents without mechanical activation

The sorbent carbonation and regeneration were carried out isothermally at 650, 700, and 750 °C first for the sorbent without any mechanical activation (**Figure 2.8**). The results indicate the higher conversion is achieved at a lower temperature for the carbonation reaction. Although the difference in conversion between 650 and 700 °C is not considerable, the decrease in conversion is notable for 750 °C. In addition to the conversion difference at the 40 min mark, the carbonation rate at 750 °C decreased significantly. This is because 750 °C was getting close to the inversion temperature where carbonation and decarbonation are taking place with the same rate under 0.2 atm of CO_2.

For all tested temperatures, the earlier fast carbonation stage is followed by a later slow carbonation stage as seen in **Figure 2.8**. The first-order reaction rate constant was calculated in the fast carbonation stage. The rate constants for carbonation were 16.31, 11.31, and 3.35 min^{-1} at 650, 700, and 750 °C, respectively. The rate constant is in good agreement with another in situ XRD study of Biasin et al. The reported carbonation rate constant was 10.8 min^{-1} at 650 °C under 100% CO_2 [86]. Carbonation slows significantly after around 10 min at 650 and 700 °C, while this carbonation speed change took place around 20 min at 750 °C. This is related to the formation of the carbonate shell around calcium oxide. Once direct contact of calcium oxide and CO_2 molecule is prohibited by the carbonate shell, solid-phase diffusion through the carbonate shell becomes rate determining. It is also notable that the homemade $Ca(OH)_2$ with the low surface area, small pore volume, and big crystal size still showed a carbon capture ability similar to that of commercial $Ca(OH)_2$ even though regeneration was somewhat slower. Both samples were not mechanically activated. Increasing the $Ca(OH)_2$ crystal size beyond 100 nm did not limit the sorbent activity, which violated prediction from mere linear extrapolation. This could be explained if big sorbent

particles go through mechanical pulverization during the carbonation step due to stress build-up from a molar volume mismatch between CaO and $CaCO_3$.

The regeneration reaction showed the opposite temperature dependence as expected by its endothermicity. At higher temperature, the CaO recovery was faster. The regeneration kinetics show a strong temperature dependence. For CH0, the first-order rate constants for the regeneration reaction were 1.45, 4.32, and 12.28 min^{-1} at 650, 700, and 750 °C, respectively. Without mechanical activation, the complete regeneration was never achieved within 100 min under pure nitrogen flow. The results indicate that 700 °C operation should be preferred for isothermal cycling because we should have a high enough carbonation and regeneration reaction rate for a practical level of carbonation and decarbonation.

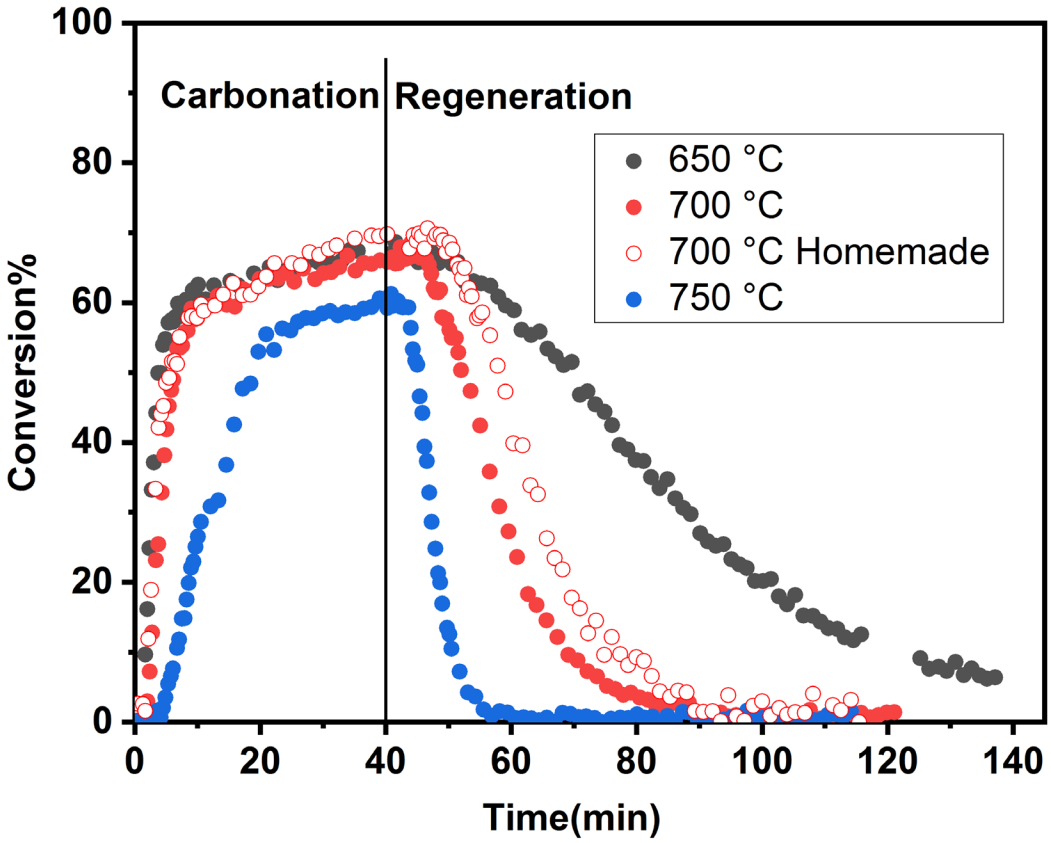

Figure 2.8. CaO conversion % as a function of time for sorbents without mechanical activation. Carbonation gas condition: 20 sccm CO_2 + 80 sccm N_2. Regeneration condition: 100 sccm pure N_2. Sorbent behavior of two different samples is shown: CH0 and homemade $Ca(OH)_2$.

2.3.3 Carbonation kinetics

Mechanical activation was effective for carbonation reaction as seen in **Figure 2.9**. A higher milling speed results in higher conversion within 40 min. The rate constant increased for 650 °C operation, especially for the sorbent milled at 500 rpm as noted with an arrow in **Figure 2.9d**. At 650 °C, the constant reaction rate increased from 16.3 to 24.2 min^{-1}. However, for other temperatures, the mechanical activation did not raise up the carbonation rate much. When we have

a weak thermodynamic driving force toward carbonation, microstructure control cannot result in fast carbonation. From **Table 2.1**, one can see that the pore volume increases significantly for the 500 rpm $Ca(OH)_2$ sample. We assume that this pore volume increment still applies when $Ca(OH)_2$ converts to CaO when heated. The mechanically induced microstructural change enhanced carbonation kinetics only when a substantial thermodynamic driving force is present as in 650 °C operation.

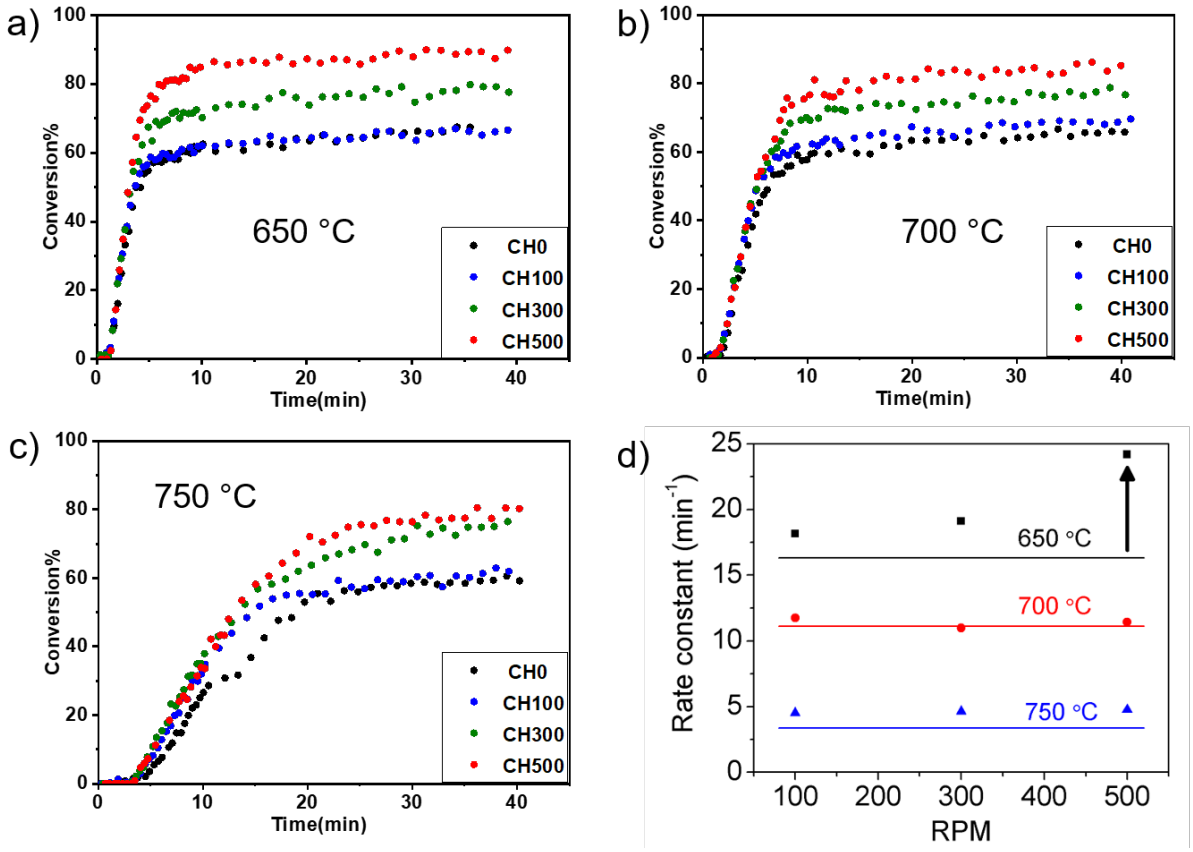

Figure 2.9. Comparison of the CaO conversion % of the samples at different temperatures: (a) 650 °C, (b) 700 °C, and (c) 750 °C. The feed gas was 20% CO_2 in N_2. (d) Carbonation rate constant from the fast carbonation stage. Solid lines note values of CH0.

It should be noted that the carbonation reaction does not immediately proceed when CO_2 gas is introduced into the XRD reactor. Before CO_2 was introduced, the reactor was filled with N2; thus the reactor needs some time to reach a specific concentration of CO_2 to initiate the reaction. This phenomenon relates to the thermodynamics of the reaction. At a higher temperature, a higher CO_2 concentration is needed to initiate carbonation. Thus, at a higher temperature, it took more time for the reaction to get started.

Among all of the ball milled samples, CH500 had the highest conversion of CaO to $CaCO_3$ within 40 min of carbonation. CH0 and CH500 show a remarkable conversion difference at all tested temperatures. The conversion increased from 65.5% to 85.2%, from 62.4% to 81.7%, and from 58.4% to 77.2% at 650, 700, and 750 °C, respectively, for these two extreme cases.

The fast carbonation and high conversion of CH500 should originate from the sorbent microstructure. The crystal size of this sample was the smallest among all sorbents. As Biasin et al. [86] have shown in their study, the smaller crystal size of sample increased the final conversion of CaO. The pore volume of CH500 is notably high as compared to that of other samples (**Table 2.1**). A higher pore volume should facilitate CO_2 gas-phase mass transport to the CaO surface. Consequently, the reaction between CO_2 and CaO can take place easier, which shows a good agreement with a previous report [88] where the authors demonstrated that the CO_2 sorption capacity depends on the surface area and pore size. In that work, pore size played a more dominant role over surface area. This is what we see from our mechanically activated samples. Some loss of surface area could be tolerated when the pore volume increases as in the case of CH500.

2.3.4 Regeneration kinetics

Mechanical activation on the sorbents was effective for the regeneration as well as carbonation process. In general, with increasing speed of ball milling, the regeneration reaction

rate increased (**Figure 2.10**); however, like the carbonation reaction, the sample needs to be ball milled at a higher speed to see a considerable change. Even though mechanical activation has a favorable impact on rate constants, it should be noted that mechanical activation could not remove/modify the initial delay time for the reaction. This indicates that microstructure manipulation cannot alter the thermodynamics of the reaction, as expected. At 650, 700, and 750 °C, the regeneration reaction started after 10, 7, and 4 min, respectively. To have a thermodynamic driving force of the reaction at a specific temperature, the concentration of CO_2 in the gas should be lower than a threshold value for the regeneration reaction to be started. This concentration is lower at lower temperature. Because gas exchange in the XRD reactor cannot be immediate, it takes time to get to the low enough CO_2 concentration. Thus, the regeneration will initiate at a later stage for lower operation temperature. The recovery of CaO from $CaCO_3$ was calculated as follows:

$$Recovery\% = \frac{Initial\ conversion\% - Conversion\%\ during\ regeneration}{Initial\ conversion\%} \qquad (2-3)$$

As can be seen in **Figure 2.10**, at 650 °C the regeneration reaction could not be completed even after 100 min (~90% only). The final recovery at 700 and 750 °C was almost 100%. Given enough time (>80 min), after one carbonation step, all recovery converges no matter what rpm was chosen for mechanical activation.

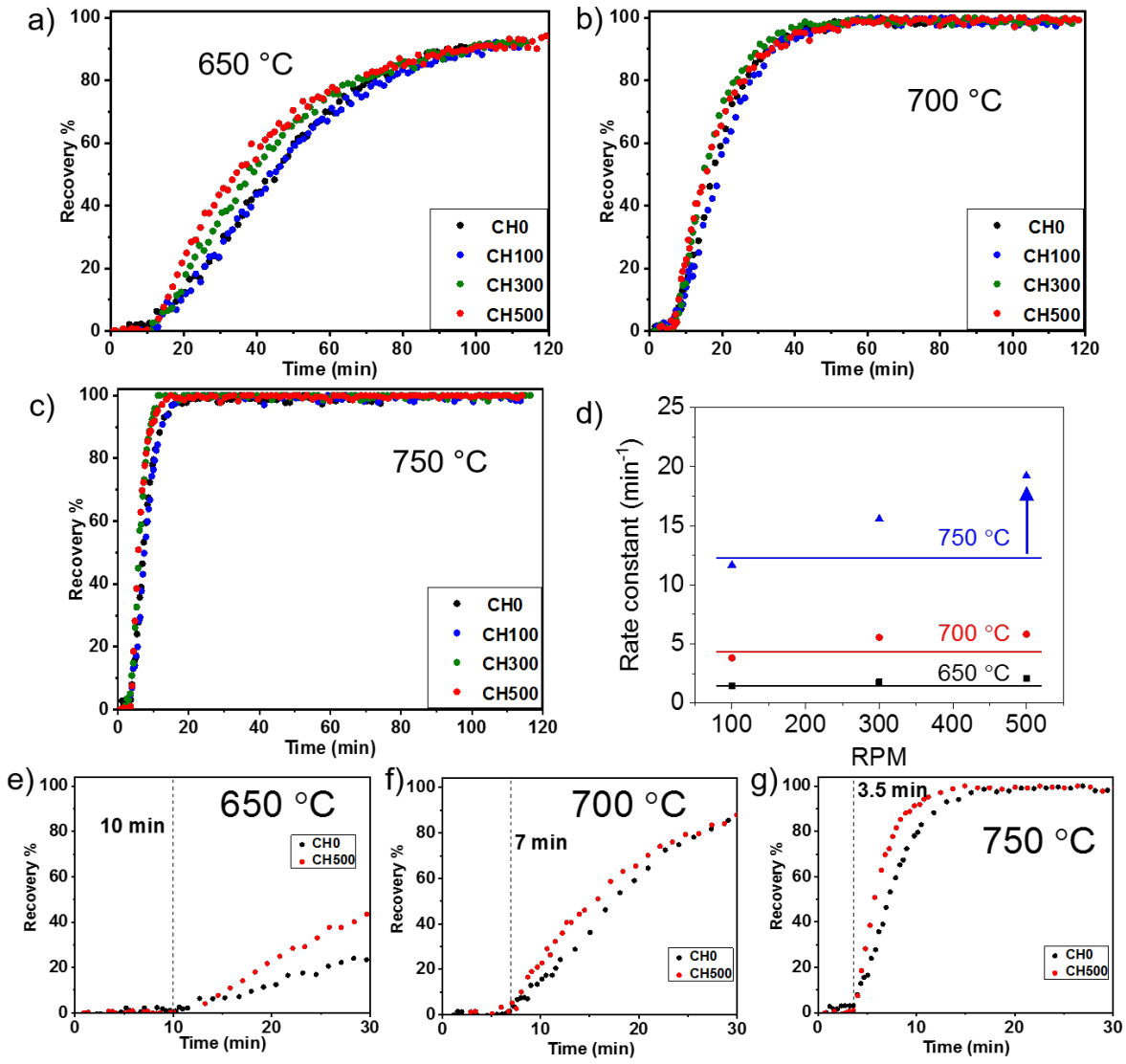

Figure 2.10. Comparison of the CaO recovery % of the samples at different temperatures: (a) 650 °C, (b) 700 °C, and (c) 750 °C. The feed gas was 100% N2. (d) Decarbonation rate constant from the fast decarbonation stage. Solid lines note values of CH0. (e–g) Recovery rate comparison for three temperatures. Two extreme cases are compared. All data points are from (a)–(c) plotted up to 30 min only.

2.3.5 Isothermal cycle stability

Because CH500 shows the highest reaction rates for carbonation and decarbonation, the cycle stability of this sample was further investigated. The multiple cycle test was conducted at 700 °C. From the results in **Figure 2.9** and **Figure 2.10**, one can see that the overall round-trip reaction rate will be higher when carbonation takes place at 650 °C and decarbonation takes place at 750 °C. However, we wanted to study sorbent performance under isothermal operation condition because this operation mode can simplify carbon capture system and may reduce energy cost in regeneration. 700 °C was chosen because reaction rates for both carbonation and regeneration were acceptable.

To test the isothermal cycle stability, 20 min of carbonation and 40 min of regeneration were performed for each cycle. One full cycle corresponds to 1 h. 10 cycles are shown in Figure 6a for two extreme cases, CH0 versus CH500. Both samples show good cycle stability because the carbonation/decarbonation condition that we chose is avoiding the high temperature regeneration step. During this 10-cycle test, the final conversion for CH500 goes from 84% (cycle #1) to 60% (cycle #10). These values went from 65% to 50% for CH0. For the 10 cycles, the theoretical CO_2 capture capacity should be 7.85 g CO_2/g CaO when we assume all calcium atoms are interacting with CO_2 molecules. In our 10-cycle experiment, the entire cycle capture capacity was 5.35 g CO_2/g CaO for CH500 (68.2% efficiency) and 4.33 g CO_2/g CaO for CH0 (55.2% efficiency). A 24% capture capacity enhancement was realized by mechanical activation.

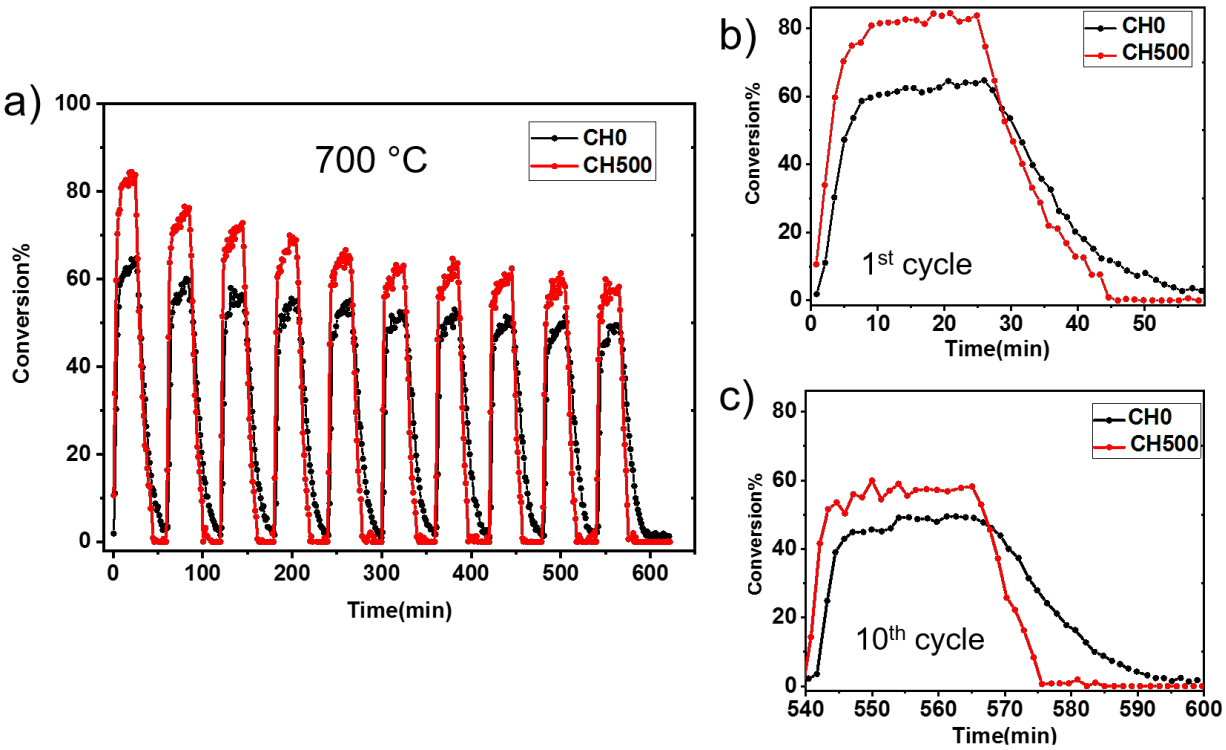

Figure 2.11. (a) Comparison of the isothermal cycle stability between CH0 and CH500. (b) The first cycle. (c) The 10th cycle.

From **Figure 2.11a**, we can see the regeneration was completed for CH500 in each cycle (100% recovery); however, for CH0, there was always a small amount of residual $CaCO_3$ after each cycle. During the 10 cycles, these patterns were repeated. The regeneration rate of CH500 was always higher than that of CH0. The difference becomes more remarkable after each cycle. At the first cycle, the regeneration curves from both samples almost overlap (**Figure 2.11b**), but the difference was considerable at the 10th cycle (**Figure 2.11c**). We do not see regeneration rate degradation for CH500, whereas the regeneration rate decreased after each cycle for CH0.

The change in morphology of the sample was investigated by SEM observation (**Figure 2.12**). After 10 cycles, the particle size increases, and the solid sample seems to lose porosity in

both cases. Notably, we can still see small particles in the CH500 sample even after 10 cycles. The BET surface area and pore volume after 10 cycles were 24 m^2/g and 0.078 cc/g for CH0 and 30 m^2/g and 0.091 cc/g for CH500, respectively (**Figure 2.13**). The total pore volume is not very different between these two after 10 cycles. We need to look at the pore size distribution by the BJH method to see the impact of mechanical activation on the pore structure evolution (**Figure 2.14**). Mechanical activation increases the population of large (d > 10 nm) pores in the initial $Ca(OH)_2$ that is not yet heated. After 10 cycles, both CH0 and CH500 lose small (d < 10 nm) pores, while the larger pore population increases. However, the pore population increase in the 10–25 nm size range is steeper for CH500 than for CH0 in addition to the initial higher pore population in that size range for CH500. This is in agreement with the better performance of CH500 over CH0 during the 10 cycles. Larger pores that facilitate the gas–solid reaction by lowering the mass transport barrier form during the mechanical activation of $Ca(OH)_2$ and during the decarbonation of mechanically activated sorbent.

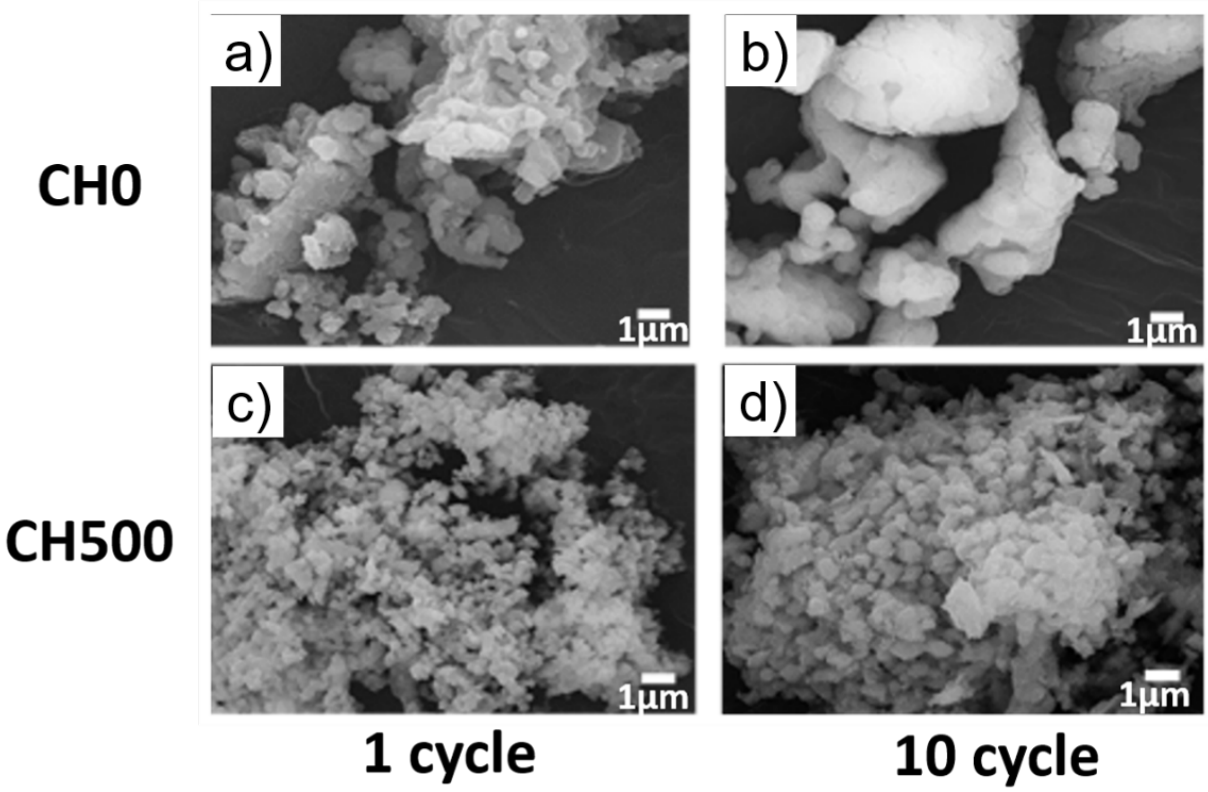

Figure 2.12. SEM images of the samples after 1 cycle and 10 cycles. (a) CH0 after one cycle. (b) CH0 after 10 cycles. (c) CH500 after 1 cycle. (d) CH500 after 10 cycles.

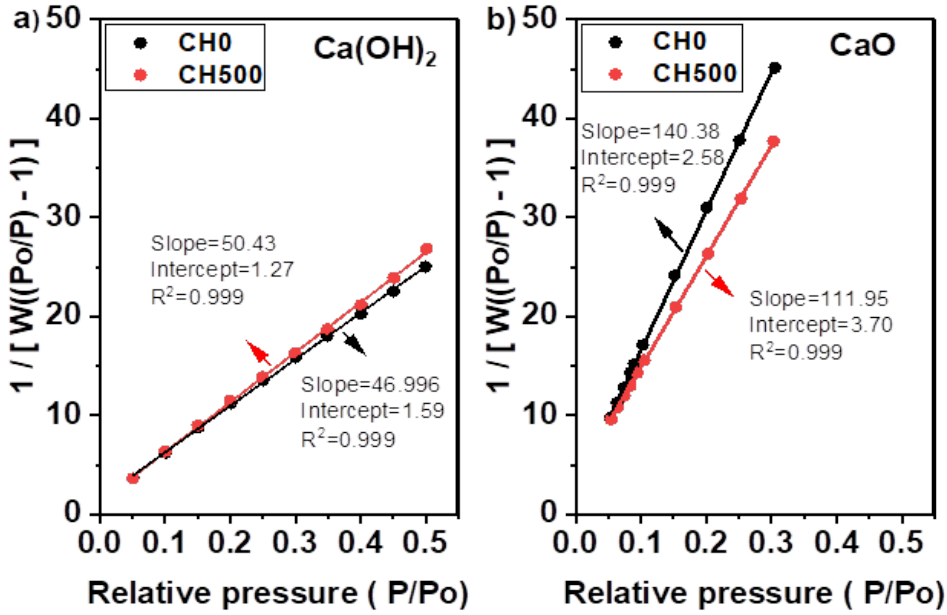

Figure 2.13. BET plot. a) Before any cycling (surface area of 71.7 m2/g for CH0 and 67.4 m2/g for CH500). b) After ten cycles (surface area of 24 m^2/g for CH0 and 30 m^2/g for CH500).

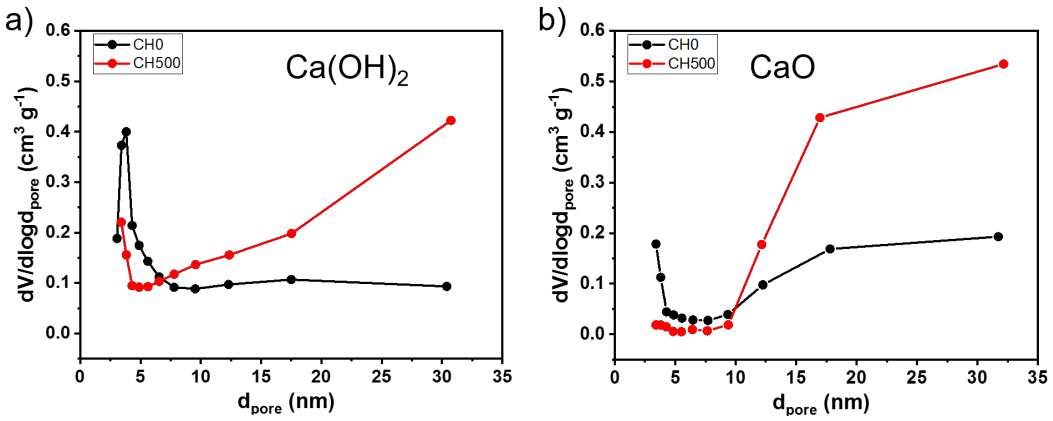

Figure 2.14. BJH pore size distribution up to 35 nm. (a) Before any cycling (surface area: 71.7 m^2/g for CH0 and 67.4 m^2/g for CH500). (b) After 10 cycles (surface area: 24 m^2/g for CH0 and 30 m^2/g for CH500).

Figure 2.15 shows the crystallite size change during the cycling. The data were collected at the end of each carbonation step right before regeneration. Because conversion is not 100%, the carbonate phase and the oxide phase are coexisting. We already know that the regeneration rate was the main difference between CH500 and CH0 during the 10 cycles (**Figure 2.11**). **Figure 2.15a** shows the crystal size of the carbonate phase. Here, we do not see a clear feature that can explain the faster regeneration of CH500 and slower regeneration of CH0 over the 10 cycles. **Figure 2.15b** shows larger CaO crystals for CH500 consistently right before each regeneration step. This coarse structure of CaO seems beneficial for the regeneration rate. When $CaCO_3$ goes back to CaO, small particles of CaO will form on the surface of the $CaCO_3$. When these small particles come in contact with big CaO particles, grain growth can take place. Incorporation of the small grains into the big grains is the basis of the oxide sintering process. The bigger is the particle size difference, the bigger the driving force becomes for grain growth. We speculate that the existing CaO coarse particles work as scavengers of small, newly generated CaO particles. The quick removal of CaO exposes the $CaCO_3$ surface to CO_2-lean gas for further reaction. This CaO crystal size effect and favorable pore size distribution contribute to the better sorbent regeneration performance of CH500.

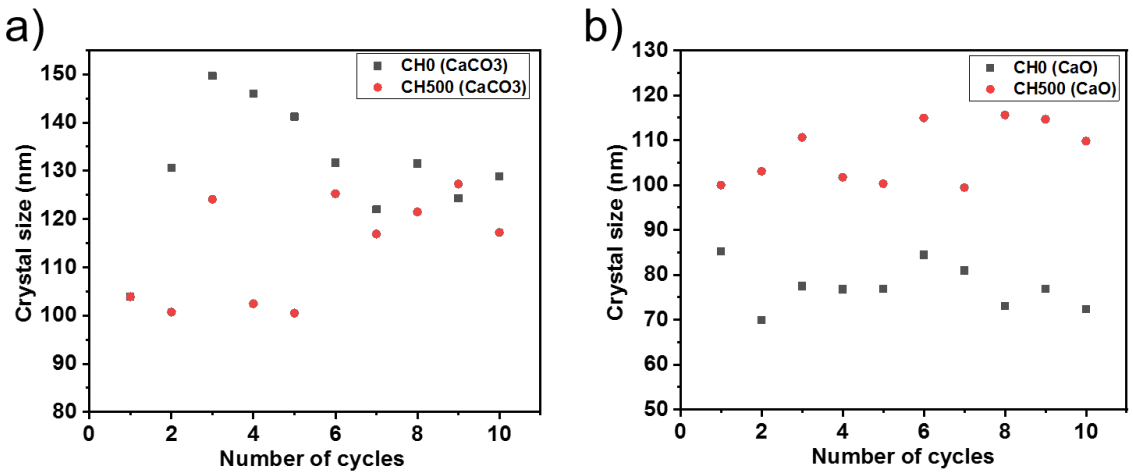

Figure 2.15. Crystallite size at the end of each carbonation step. (a) $CaCO_3$. (b) CaO. This shows the sorbent microstructure during the 10 cycles right before each decarbonation/regeneration step.

The final conversion of each cycle for CH500 and CH0 was fitted to the equation suggested by Grasa et al. as in **Figure 2.16** [52]. This is to show the limitation of the seemingly long-lasting impact of mechanical activation.

$$X_N = \frac{1}{\frac{1}{1-X_r}+kN} + X_r \qquad (2-4)$$

Where X_N is the final conversion of CaO the end of each cycle, k is the deactivation constant, X_r is the residual conversion, and N is the number of cycles. This semi-empirical equation describes the activity decay of the sorbent. The model is based on the second-order deactivation rate, which resembles catalyst deactivation by sintering. Assuming sintering to be the main

contributor for decay, we consider the residual activity of the sorbent in this model [52]. The results showed that the deactivation for CH0 is 4 times faster than that for CH500, although the residual conversions (conversion after infinite number of cycles) for both samples are close to each other. This agreement on residual conversion makes sense. We cannot expect the sorbent mechanical activation at room temperature before carbonation/regeneration cycles to have an everlasting impact.

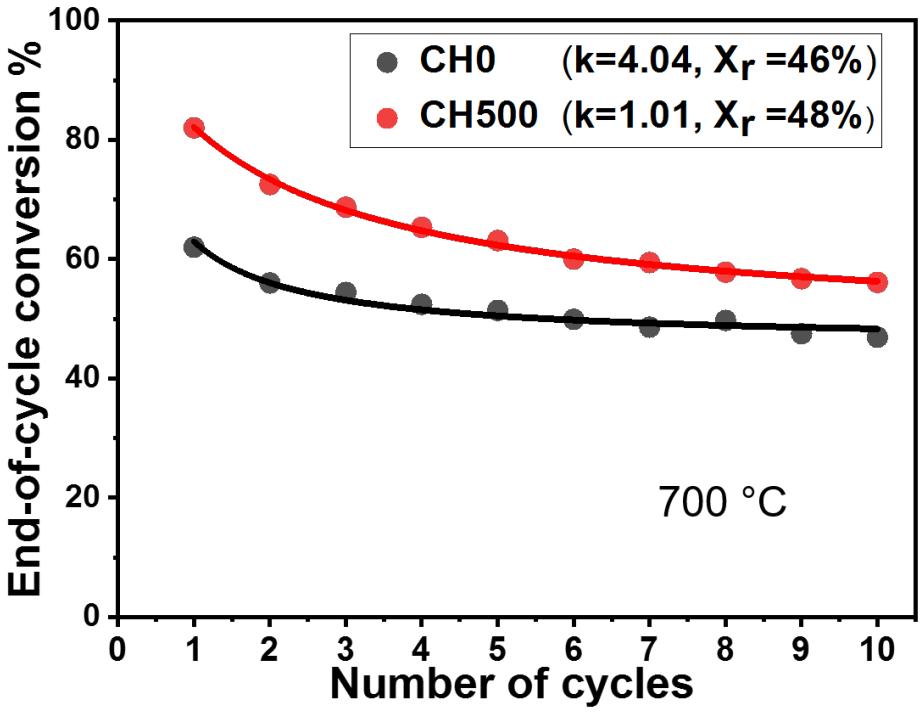

Figure 2.16. End-of-cycle conversion % of each cycle fitted to the Grasa model.

2.4 Conclusion

The effectiveness of sorbent mechanical activation was studied in this work. It was found that a high rpm activation imparted higher reaction rates in both carbonation and regeneration steps. In addition to the initial pseudo-first-order rates, the final conversion was also increased by

mechanical activation. The conversion after 40 min of carbonation increased by 20% for CH500 as compared to CH0 for all tested temperatures. With 700 °C isothermal cycling, the sorbent efficiency over 10 cycles was 68.2% for CH500, while the efficiency of the intact commercial sample under the same condition was 55.2%. By simple isothermal cycling at a well-chosen temperature, we showed that avoiding too high of a regeneration temperature clearly suppresses sorption capacity decay manifested by high residual conversion. Through mechanical activation, both pore structure and calcium oxide crystallite size are preferably tuned to result in facile regeneration of the sorbent over multiple cycles.

Chapter 3 Ca_2CuO_3: A high temperature CO_2 sorbent with rapid regeneration kinetics

Abstract

Three different calcium-based ternary oxide sorbents, Ca_2CuO_3, $Ca_3Co_4O_9$, and $Ca_2Fe_2O_5$, were characterized as potential sorbents for CO_2 capture. The behaviors of these sorbents were compared to CaO under various CO_2 concentrations via temperature programmed carbonation/decarbonation. Ca_2CuO_3 and $Ca_3Co_4O_9$ showed lower inversion temperatures, while $Ca_2Fe_2O_5$ had a higher inversion temperature than CaO. In addition, the copper and cobalt containing sorbents showed relatively narrower temperature windows going from the highest carbonation rate to the highest decarbonation rate. This narrow temperature window can be advantageous in operating a temperature swing process. $Ca_3Co_4O_9$ and $Ca_2Fe_2O_5$ showed low conversion. Under the best-case scenario, the conversion of these sorbents was less than 25 percent. Ca_2CuO_3 showed faster regeneration compared to CaO when the sorbent temperature was cycled between 700 and 800 °C. In addition, we found 740-850 °C for Ca_2CuO_3 and 640-900 °C for CaO as the temperature swing windows of the best reaction rates. The narrower range of operational temperature (110 °C for Ca_2CuO_3 compared to 260 °C for CaO) can lead to higher overall rate of CO_2 uptake and release. Ca_2CuO_3 showed 60% higher cycle-averaged decarbonation rate compared to CaO when cycled between the temperatures of maximum carbonation and decarbonation rates.

3.1 Introduction

The atmospheric CO_2 concentration has been increasing through the past decades, and it reached the highest record (410 ppm) in 2019, an increase of 2.5 ppm compared to 2018 [89]. This high concentration of carbon dioxide contributes to climate change. Therefore, CO_2 capture and storage play a critical role in mitigating climate change. Calcium looping is one of the most

efficient and low-cost post-combustion technologies for CO_2 capture [35, 36, 40, 90-92]. The main source of CaO is naturally occurring limestone. The abundance of this sorbent makes it a favorable candidate for chemical looping processes. CaO-based sorbents capture CO_2 through the following reversible reaction:

$$CaO\ (s)\ +\ CO_2\ (g)\ \leftrightarrow\ CaCO_3\ (s) \qquad (3-1)$$

Instead of releasing CO_2 to the atmosphere after burning fossil fuel, if we redirect the flue gas mixture into the carbonation reactor, the CO_2 portion of the gas reacts with the CaO and turns into $CaCO_3$. The product gets moved to a decarbonator and decomposes to CO_2 and CaO. The pure CO_2 gas is then collected for sequestration, and the regenerated oxide returns to a carbonation reactor for the following carbonation process.

A profound understanding of deactivation and stabilization mechanisms is critical to improving the next generation of CaO-based sorbents [93]. This sorbent's CO_2 capture performance degradation mainly originates from particle sintering over multiple carbonation-decarbonation cycles [87, 94-96]. The scientific community strives to develop anti-sintering strategies to overcome this problem [70, 96-98].

Incorporation of inert metal oxides into CaO to hinder the active phase sintering has been studied previously [99-101]. These studies mainly focused on the stability improvement of the sorbent. Liu et al. synthesized "sintering-resistant sorbents" from calcium and magnesium salts using wet mixing. They found the coexistence of CaO and MgO in their sorbent led to high stability over 24 cycles [55]. The use of coal fly ash has been reported to increase the cycle stability of CaO-based sorbent due to presence of inert materials (SiO_2 and mullite) by hindering aggregation

and sintering [102]. Incorporating of metallic stabilizers is another reported method to increase the cycle stability of CaO-based sorbent and its composites. Aissaoui et al. reported enhanced cycle stability for CaO/NiO composite sorbent by doping Fe/Mg stabilizers. They reported that the formation of mixed oxide reduced the sorbent structural deterioration caused by CaO agglomeration [103]. Radfarnia et al. used various metal sources such as Al, Zr, and Mg to improve the performance of calcium oxide. The effect of metal to calcium ratio (M/Ca) was investigated in their work, and they found the ratio of 0.1 was the optimum composition for Al and Zr and 0.4 for Mg. They also showed that the performance of Zr-stabilized sorbent exhibited the most efficient behavior [104]. Despite the effectiveness of Zr, the high material cost directed the researchers to focus on less expensive elements such as copper and iron. Qin et al. enhanced the performance of the CaO sorbent by thermal pretreatment of CuO [105]. Chen et al. reported that structural change of CuO to hollow spheres enhanced the cycle stability of CaO/CuO composite sorbent [106]. Kazi et al. developed a highly stable composite for CO_2 capture for a Ca-Cu looping process. The composite of 22 wt% CaO, 25 wt% $Ca_{12}Al_{14}O_{33}$, and 53 wt% CuO had a better mechanical strength than calcined limestones do [107]. Manovic et al. synthesized a CaO/CuO-based core-shell composite that has high attrition resistance**.** They found no change in the pore size distribution after high temperature fluidization [108]. Minardi et al. studied influences of metal oxides additives on the CaO-based sorbents' stability and capacity. A number of metal additives were investigated to improve the sorbent performance. They found sorbents containing Y, Nd, Er and Mg had highest sorption capacity and Al, Er, Y and Nd had the most efficient stability [109]. Recently, Alshafei worked on the incorporation of metal oxide into CaO using electrospinning technique with the targeted morphology. They suggested Al-doped CaO nanofibers had a high conversion due to small crystallites of CaO and macroporous intrafiber networks. These nanofibers

also had high stability owing to $Ca_{12}Al_{14}O_{33}$ phase existence (a thermally stable phase) in the sorbent which alleviated the agglomeration [110]. Recently, it has been reported that incorporation of inert supports such as mayenite ($Ca_{12}Al_{14}O_{33}$) and brownmillerite ($Ca_2Fe_2O_5$) increases the mechanical strength and cycle stability of CaO-based sorbent [111-113].

Compared to the numerous thermodynamics studies on CaO carbonation/decarbonation [69, 114-118], reports on sorbent performance of calcium-based single-phase ternary oxides have been relatively scarce. Some studies are documented for syngas and hydrogen production [119-121]. Unlike the conventional method of introducing inert materials from external sources to mitigate sintering, Dang et al. addressed this issue using a misfit layered material, $Ca_3Co_4O_9$, that goes through reversible cobalt precipitation/re-incorporation. CaO and Co form a homogenous composite that suppresses sintering of CaO [122].

A single-phase ternary oxide provides the best mixing of in situ generated second phases and CaO compared to physically mixing in the sintering-barrier phases. Our interest is to study how the endogenous phases will impact the composite microstructure of the sorbent and decarbonation kinetics. Unlike other works that just focus on the cycling stability of the sorbent, we wanted to see if our sorbents can be used in temperature windows of better energy efficiency and reasonable reaction rates. We therefore investigated the sorbent behavior using the TPC-TPDC technique to find the most efficient temperature windows for carbonation and decarbonation process.

In this work, we synthesized three different calcium-based ternary oxide sorbents: Ca_2CuO_3, $Ca_2Fe_2O_5$, and $Ca_3Co_4O_9$. To estimate the operational temperature of the calcium looping process using these new sorbents, we adopted temperature programmed carbonation and decarbonation (TPC-TPDC) as a vital tool to study the carbonation/decarbonation

thermodynamics of these oxides. During the temperature rise, we monitor CO_2 concentration in the exhaust gas from the sorbent powder bed to evaluate the carbonation and decarbonation performance of the sorbent. From one TPC-TPDC experiment, we can get the CO_2 capacity and inversion temperature where the carbonation reaction shifts to the decarbonation reaction. The three ternary oxides were evaluated for their potential as high temperature CO_2 sorbents.

3.2 Experimental section

3.2.1 Sorbent preparation

Calcium-based ternary oxide sorbents were synthesized by the sol-gel method [123]. We chose Cu, Fe, and Co as the second metal since their oxides are easily reducible and it is possible to synthesize single-phase ternary oxides with calcium-to-metal ratios of 1 (Fe), above 1 (Cu), and below 1 (Co). To synthesize Ca_2CuO_3, $Ca_2Fe_2O_5$, and $Ca_3Co_4O_9$, the stoichiometric amounts of calcium nitrate tetrahydrate (BeanTown Chemical, 99%), copper (II) acetate monohydrate (Sigma-Aldrich, ACS Reagent, ≥98%), cobalt (II) nitrate hexahydrate (Acros Organics, 99%, pure), and iron (III) nitrate nonahydrate (Alfa Aesar, ACS 98.0-101.0%) were dissolved in 20 ml deionized water under magnetic bar stirring. Then a proportional amount of citric acid was added to each solution. After 2 hours of stirring, the solution was heated to 180 °C to form a gel. The temperature was further raised to turn the gel into ash. The ash was collected and placed into a high temperature furnace. The furnace was programmed to go to 900 °C in 3 hours (Heating rate ~5 °C/min) and keep the temperature at 900 °C for 3 hours (**Figure 3.1**). Only for $Ca_3Co_4O_9$, we calcined the sample at 800 °C to avoid impurity phase (see Section 3.1).

To compare the ternary oxides with CaO, the most common high temperature CO_2 sorbent, we converted calcium hydroxide to CaO at 900 °C in air for 3 h. After cooling down the sample, we confirmed that we have CaO (**Section 3.1**).

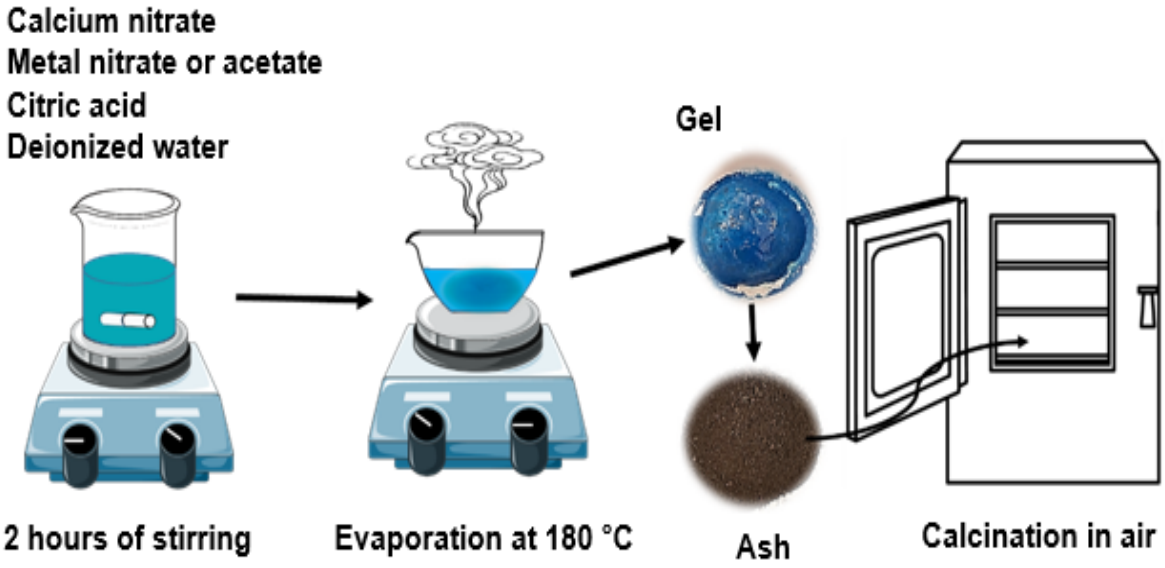

Figure 3.1. The schematic of the sorbent synthesis.

2.2. CO_2 uptake/release measurement

All experiments were conducted in a tube furnace with quartz tubes (inner diameter of 0.86 inches and length of 24 inches). 0.5 gram of sorbent powder was loaded on a ceramic boat in the quartz tube. To calculate decarbonation enthalpy, we selected four different concentrations of CO_2: 5, 10, 15, and 20 volumetric percent. We kept the total flow rate for all experiments at 100 sccm. For instance, if the concentration of CO_2 was 5 %, then we had 5 sccm CO_2 and 95 sccm N_2. The gas flow rates were controlled by mass flow controllers (MKS G series) within ±1 sccm error. The outlet of the reactor (quartz tube) was connected to a CO_2 sensor (ExplorIR®-M CO_2 Sensor, CM-40831) at room temperature to monitor the amount of CO_2 in the exhaust gas. The CO_2 content was recorded every 10 seconds while the sample temperature went from room temperature to 950 °C. The CO_2 molar concentration was calculated by the equation below:

$$C_{CO_2} = \left(\frac{F_{CO_2}}{F_{total}}\right)\left(\frac{\rho_{CO_2}}{M_{CO_2}}\right) \quad (3-2)$$

where C_{CO2}, F_{CO_2}, F_{total}, ρ_{CO_2}, and M_{CO_2} are the molar CO_2 concentration (mol/cm^3), CO_2 flow rate (sccm), total flow rate (sccm), density (g/cm^3), and molecular weight of CO_2 (g/mol), respectively.

3.2.2 Temperature swing carbonation and decarbonation

Temperature swing is a common regeneration practice for solid sorbents [124]. We examined the performance of the CaO and Ca_2CuO_3 under 10% CO_2 (10 sccm CO_2 and 90 sccm N_2) during 6 cycles of carbonation and decarbonation. 0.5 g of the solid sorbent was used in each case. We first heated the sorbent at a 10 °C/min rate to 700 °C and held it at that temperature for 10 minutes to prepare for the temperature cycling. The sample was then heated at a 5 °C/min rate to 800 °C for the first 10-minute decarbonation before cooling back to 700 °C. We repeated the temperature swing 5 more times between 700 and 800 °C ($\pm$ 5 °C/min, 10-minute dwell at preset temperatures) before cooling the sorbent down to the room temperature under 10% CO_2. This procedure gives 6 carbonation periods and 5 decarbonation periods in total.

During this process mass gain rate was calculated based on the following equation:

$$mass\ gain\ rate\ (g\ CO_2/g\ Ca/min) = \frac{\left(F_{CO_2\ IN} - F_{CO_2\ OUT}\right) \times \rho_{CO_2}}{m_{Ca}}. \quad (3-3)$$

where, $F_{CO_2\ OUT}$ is the instantaneous volumetric flow rate that changes over time during the experiment due to the CO_2 uptake or release. $F_{CO_2\ IN}$ is the preset CO_2 volumetric flow rate, a constant value over the duration of an experiment. m_{Ca} is the Ca mass content in the 0.5 g of the solid sorbent.

In addition to the 700-800 °C temperature swing experiment, we cycled selected sorbents between the temperatures of maximum carbonation and decarbonation rates (T_c and T_d, see section 3.1) to examine the sorbent performance within the ideal temperature window. The sorbents were heated to T_c under pure N_2. The gas flow was then changed to 20% CO_2 to initiate the carbonation reaction. After 10 minutes of carbonation, the reactor temperature was further raised to T_d. The sorbent was held for 10 minutes at this regeneration temperature. We repeated this T_c-T_d temperature cycling with 10 °C/min heating and cooling rates to have 12 carbonation periods and 11 decarbonation periods in total.

3.2.3 Enthalpy calculation

The relation between equilibrium constant and standard Gibbs free energy can be correlated by following equation.

$$\Delta G° = \Delta H° - T\,\Delta S° = -RT \ln K \qquad (3-4)$$

where T is the equilibrium temperature (inversion temperature), R is the universal gas constant, ΔH° and ΔS° are standard enthalpy change and standard entropy, and K is the equilibrium constant.

We can rewrite Equation 4:

$$\ln K = -\frac{\Delta H^{\circ}}{RT} + \frac{\Delta S^{\circ}}{R}. \quad (3-5)$$

Considering the decarbonation reaction of $CaCO_3$,

$$K = \frac{a_{CO_2} a_{CaO}}{a_{CaCO_3}}. \quad (3-6)$$

Taking the activity of the CO_2 as partial pressure of CO_2 and taking solid phase activities to be 1,

$$K = P_{CO_2} \quad (3-7)$$

By substituting Equation 7 to Equation 5, the relation between P_{CO_2} and the inversion temperature can be written as the following [69, 125-127],

$$lnP_{CO_2} = -\frac{\Delta H^{\circ}}{RT} + \frac{\Delta S^{\circ}}{R}. \quad (3-8)$$

By plotting lnP_{CO_2} against 1/T, we can get $-\Delta H°/R$ from the slope of the linear fit and $\Delta S°/R$ from the intercept.

3.2.4 Results and Discussion

3.2.4.1 Synthesized sorbent

The X-ray diffraction patterns were taken for the synthesized sorbents after calcination at 900 °C. The results showed Ca_2CuO_3 and $Ca_2Fe_2O_5$ phases without any impurity phase. However, the calcium-cobalt sample had both $Ca_3Co_4O_9$ and $Ca_3Co_2O_6$ (**Figure 3.2)**. To get the phase-pure material, we lowered the $Ca_3Co_4O_9$ calcination temperature to 800 °C for all the following syntheses. The three single-phase ternary oxides and calcium oxide were successfully synthesized. **Figure 3.3** shows the diffraction patterns taken using an in-house X-ray diffractometer (Proto manufacturing, AXRD). The crystal parameters of sorbents were obtained by Retrieval refinement analysis (MAUD software) and presented in **Table 3.1**. The Miller indices of each sorbent were summarized in **Table 3.2**.

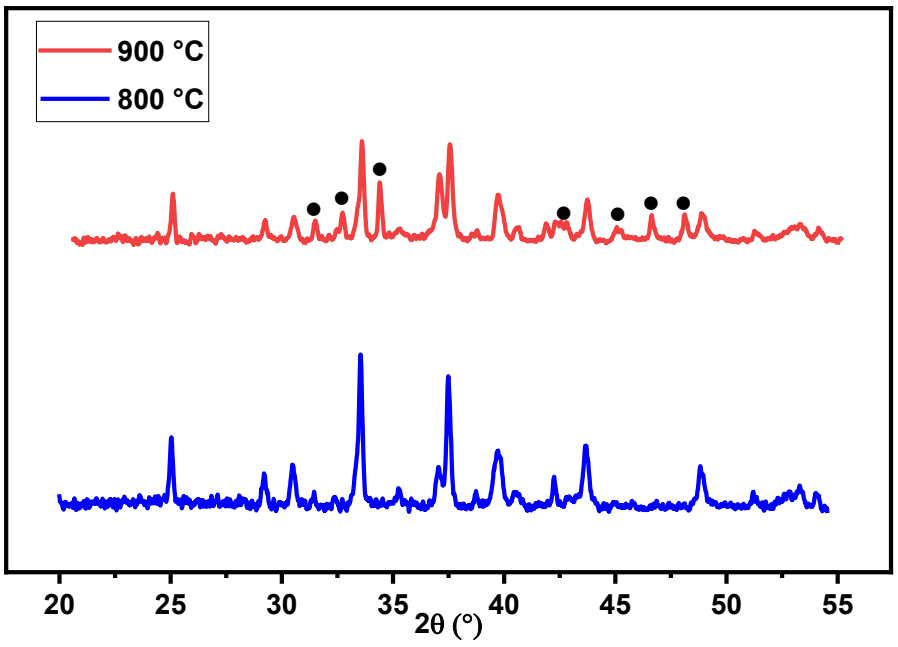

Figure 3.2. XRD of calcium cobalt oxide at 800 °C (blue line) and 900 °C (red line). "•" indicates XRD peaks for $Ca_3Co_2O_6$. The peaks without any mark show $Ca_3Co_4O_9$ peaks.

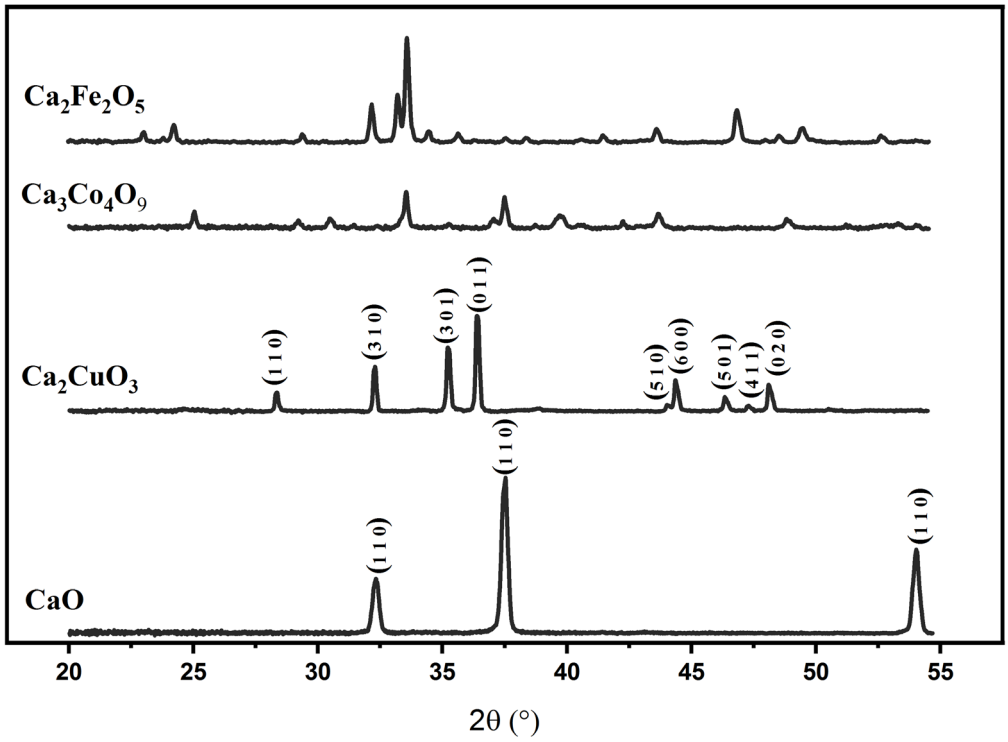

Figure 3.3.The X-ray diffraction patterns of the synthesized samples. The calcination temperature of all samples was 900 °C except $Ca_3Co_4O_9$. The calcination temperature of $Ca_3Co_4O_9$ was 800 °C.

Table 3.1. Crystal parameter of the synthesized sorbents.

Sorbent (COD ID)	Symmetry	Space group	Size (Å)	Microstrain	Unit cell (Å^3)	R_{wp} (%)
CaO (1000044)	Cubic	Fm-3m	1736	7.00E-04	111.4	3.3
Ca_2CuO_3 (2002257)	Orthorhombic	Immm	1988	1.30E-03	151	2.8
$Ca_3Co_4O_9$* (-)	Monoclinic	P2(3)	-	-	-	-
$Ca_2Fe_2O_5$ (1008777)	Orthorhombic	Pcmn:cba	973	1.90E-03	437.1	3.9

* CIF file was not available in COD (Crystallography Open Database).

Table 3.2. Peak positions (2θ) and Miller indices of the synthesized sorbents.

CaO		**Ca_2CuO_3**		**$Ca_3Co_4O_9$**		**$Ca_2Fe_2O_5$**	
Peak position	**Miller indices**	**Peak position**	**Miller indices**	**Peak position**	**Miller indices**	**Peak position**	**Miller indices**
(°)	**(h k l)**	**(°)**	**(h k l)**	**(°)**	**(h k l)**	**(°)**	**(h k l)**
32.2	1 1 1	24.6	1 1 0	24.9	0 0 3	23	1 0 1
37.4	2 0 0	32.3	3 1 0	29	1 1 1	23.8	1 1 1
53.9	2 2 0	35.2	3 0 1	30.3	$1\,\bar{1}\,\bar{2}$	24.2	1 3 0
		36.4	0 1 1	33.4	0 0 4	29.4	1 3 1
		44	5 1 0	37.3	$\bar{2}$ 0 1	32.1	2 0 0
		44.4	6 0 0	37.5	2 0 0	33.2	0 0 2
		46.4	5 0 1	39.4	0 2 0	33.7	1 4 1
		47.3	4 1 1	40.3	0 2 1	34.4	2 2 0
		48.1	0 2 0	43.5	2 0 2	35.5	0 2 2
				43.7	$\bar{1}$ 0 5	37.6	1 1 2
				48.7	2 0 3	38.4	2 2 1
				51	0 0 6	40.7	2 4 0
				52.9	2 1 3	41.5	1 3 2
				53.1	$\bar{2}$ 0 5	43.8	1 6 1
						46.9	2 0 2
						48.1	2 5 1
						48.6	2 2 2
						49.5	1 7 1
						52.6	2 6 1

3.2.4.2 Temperature programmed carbonation and decarbonation (TPC-TPDC)

First, using a plain CaO sorbent under 10% CO_2 concentration, we tested three heating rates of 2 °C/min, 5 °C/min, and 10 °C/min in the temperature-programmed experiments to see their effects on inversion temperature and the CO_2 uptake. We observed an increase in inversion temperature by increasing the heating rate (**Figure 3.4a**). Using linear regression on the three heating rates, we determined the inversion temperature by extrapolating to zero heating rate (**Figure 3.4b**). The inversion temperature was calculated to be 772 °C showing a good agreement with the literature (766 °C [22], 769 °C [23]).

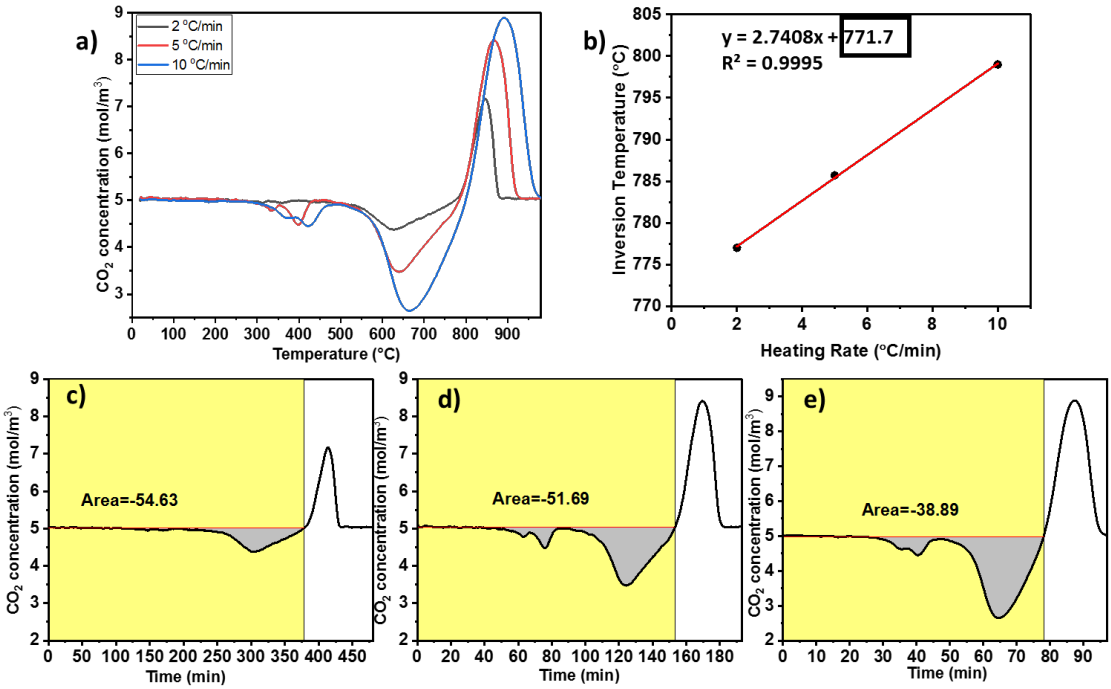

Figure 3.4. Effect of heating rate on TPC-TPDC (CaO under 10% CO_2). a) CO_2 concentration during adsorption and desorption processes with different heating rates. b) Inversion temperature as function of heating rate. c, d, and e) Amount of CO_2 adsorption at 2, 5 and 10 °C/min respectively.

Experimental results suggested that the amount of adsorbed CO_2 per mass decreased by increasing the ramping rate since the reaction time shortened (**Figure 3.4c-e**). Therefore, a lower heating rate will lead to higher CO_2 capacity for any sorbent; however, to shorten the total time of experiments, we chose 5 °C/min for our investigation for all three ternary oxide sorbents. Chowdhury et al. used the same heating rate since this heating rate is typical in large-scale twin fluidized bed reactors for CO_2 uptake and release [32].

It should be noted that the interaction between CO_2 and solid sorbent is dynamic at all temperatures where carbonation and decarbonation occur simultaneously [34]. The competition of the two reactions will determine the net sorbent mass gain or loss. **Figure 3.5** illustrates the temperature-programmed carbonation and decarbonation behavior of CaO under 10% CO_2 in balance N_2. The CO_2 uptake process starts when there is a deviation from the CO_2 feed concentration of 10 vol%. Raising temperature from room temperature, we initiate the carbonation of the sorbent. Accordingly, the CO_2 concentration will decrease in the exhaust gas (**Figure 3.5a**). The first two carbonation peaks at points "α" and "β" (i.e., 335 and 386 °C, respectively) show early carbonation due to calcium hydroxide present in the sample, which will be justified in the following sections. The carbonation rate keeps rising until it assumes a maximum, point "c" (i.e., 637 °C). After this point, the carbonation rate decreases, yet it is still the prevailing process up to point "i" (i.e., 788 °C), where the carbonation rate matches the decarbonation rate. This point is defined as the inversion temperature [32]. Above the inversion temperature, the decarbonation process takes over. The decarbonation rate peaks at point d (i.e., 871 °C). Passing point d, the decrease of decarbonation rate is inevitable due to carbonate content depletion.

The inversion point provides us with valuable information. At temperatures below this point, the carbonation proceeds. If we need to regenerate the sorbent, we need to bring the sorbent to a higher temperature than the inversion point.

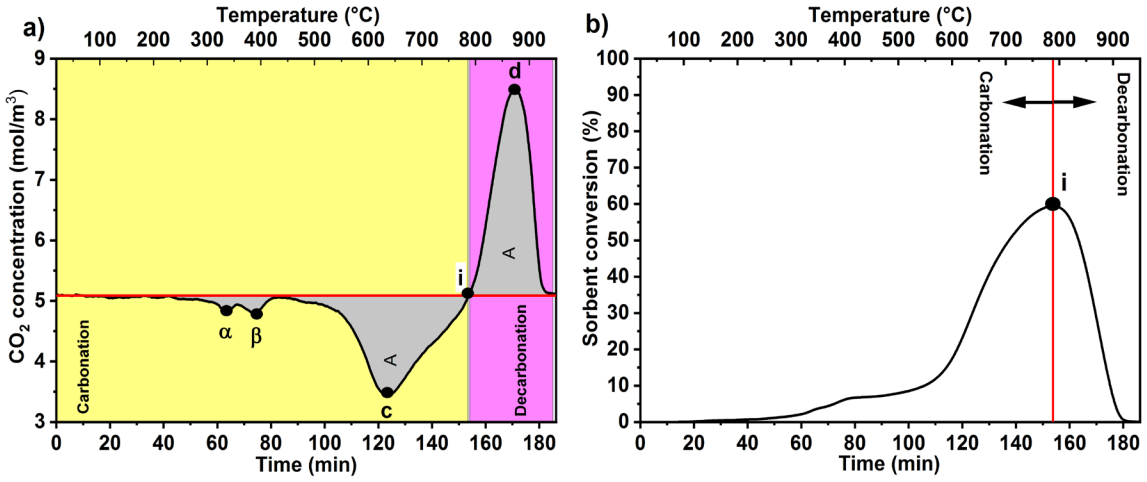

Figure 3.5. TPC-TPDC of CaO under 10% CO_2 in 90% N_2. The flow rate is 100 sccm in total. The heating rate was 5 °C/min. a) CO_2 concentration in the flue gas during carbonation and decarbonation process. b) Conversion of sorbent during the whole process. The sorbent conversion peaks at the inversion point.

3.2.4.3 CO_2 uptake and sorbent conversion

By integrating the CO_2 concentration with respect to time, the CO_2 uptake can be calculated by the following equation.

$$m = \frac{A\, \nu\, M_w}{m_s} \qquad (3-9)$$

where m is the amount of CO_2 uptake or release in g CO_2/g sorbent. A is the area under the baseline (horizontal line in **Figure 2a**) in mol min/m^3, ν is the gas flow rate in m^3/min, M_w is molecular weight of CO_2 g/mol, and m_s is mass of sorbent in g.

We defined the sorbent conversion as

$$Sorbent\ conversion\ \% = (\frac{m}{m_{max}}) \times 100 \quad (3-10)$$

Where the m_{max} is the theoretical capacity of the sorbent in g CO_2 /g sorbent. m_{max} is 0.785 g CO_2 /g sorbent for CaO.

Figure 3.5b reports the conversion of CO_2 during the carbonation and decarbonation process for CaO under 10% CO_2. As can be seen, by increasing the temperature, the conversion increases and reaches a maximum at the inversion point, then starts to decrease as the stored CO_2 starts to get released from the sorbents. The complete release of CO_2 at a very high temperature leads to zero sorbent conversion.

3.2.4.4 Effect of initial $Ca(OH)_2$ on TPC-TPDC

As described in the experimental section, we got CaO by decomposing $Ca(OH)_2$ at a high temperature. Right after cooling down in air ("Fresh"), we performed a TPC-TPDC experiment on this sorbent. The experimental data for the "Fresh" sample showed two small carbonation peaks between 300 to 450 °C (**Figure 3.6a**). These two peaks have been observed previously and attributed to CO_2 chemisorption on CaO [128, 129]. However, we saw two humidity peaks in the exhaust gas taking place precisely at the same temperature. Since the temperature was above 100°C, the behavior in this region cannot be attributed to physisorption. Therefore, the source of the humidity could be the reaction between $Ca(OH)_2$ and CO_2:

$$Ca(OH)_2\ (s) + CO_2\ (g) \rightarrow CaCO_3\ (s) + H_2O\ (g). \quad (3-11)$$

However, the characteristic diffraction peaks of $Ca(OH)_2$ were not present in the X-ray diffraction pattern of the "Fresh" sample (**Figure 3.6b**). It is possible that the amount of $Ca(OH)_2$

was not enough to be detected, or the crystallite size of $Ca(OH)_2$ was too small to be detected by XRD.

To confirm this hypothesis, we exposed CaO to ambient air at room temperature to form hydroxide naturally. After one day, we took the XRD pattern of the sample, and the existence of $Ca(OH)_2$ was confirmed (**Figure 3.6b**). The TPC-TPDC experiment was performed for the "Aged" sample. Humidity peaks were detected again in the same region as the previous sample (**Figure 3.6a**). Furthermore, the amount of water released from the sorbent during the TPC-TPDC experiment was 0.0416 g. This amount was calculated by the integration of humidity during the process.

$$RH\% = \frac{P_{H_2O}}{P^*_{H_2O}} \times 100 \rightarrow P_{H_2O} = \frac{P^*_{H_2O} \times RH\%}{100} \quad (3-12)$$

$$@T{=}20\ °C \rightarrow P^*_{H_2O} = 2333\ Pa \quad (3-13)$$

$$\overline{P_{H_2O}}\ \tau = \int_0^\tau P_{H_2O}\, dt = \frac{P^*_{H_2O}}{100} \int_0^\tau RH\%\, dt = \left(\frac{2333}{100}\right) 2410.48\ \text{Pa.min} \quad (3-14)$$

$$\overline{P_{H_2O}}\ \tau\ v = n_{H_2O} RT \rightarrow n_{H_2O} = \frac{\overline{P_{H_2O}}\ \tau\ v}{RT} \quad (3-15)$$

$$n_{H_2O} = \frac{\overline{P_{H_2O}}\ \tau\ v}{RT} = \frac{\left(\frac{2333}{100}\right) 2410.48 \times (100 \times 10^{-6})}{(8.314)(293)} = 0.00230856\ mol\ H_2O \quad (3-16)$$

$$m_{H_2O} = n_{H_2O}\ M_{w_{H_2O}} = 0.00230856 \times 18.01528 = 0.0416\ g\ H_2O \quad (3-17)$$

Where RH%, P_{H_2O}, $P^*_{H_2O}$, $\overline{P_{H_2O}}$, τ, n_{H_2O} and m_{H_2O} are water partial pressure, water saturation pressure, average partial pressure of water, experiment duration, water mole and water mass respectively.

The weight fraction of $Ca(OH)_2$ in the "Aged" sample was calculated to be 33% based on the Rietveld Refinement analysis. Accordingly, the amount of extractable water was calculated to be 0.0401 g based on the $Ca(OH)_2$ stoichiometry.

$$m_{Ca(OH)_2} = m_t \times f_{Ca(OH)_2} = 0.165\ g \qquad (3-18)$$

$$m_{H_2O} = m_{Ca(OH)_2} \times \frac{M_{w_{H_2O}}}{M_{w_{Ca(OH)_2}}} = 0.0401\ g \qquad (3-19)$$

The agreement in water content indicates that the detected steam in the exhaust gas comes from $Ca(OH)_2$ carbonation (Equation 3-11).

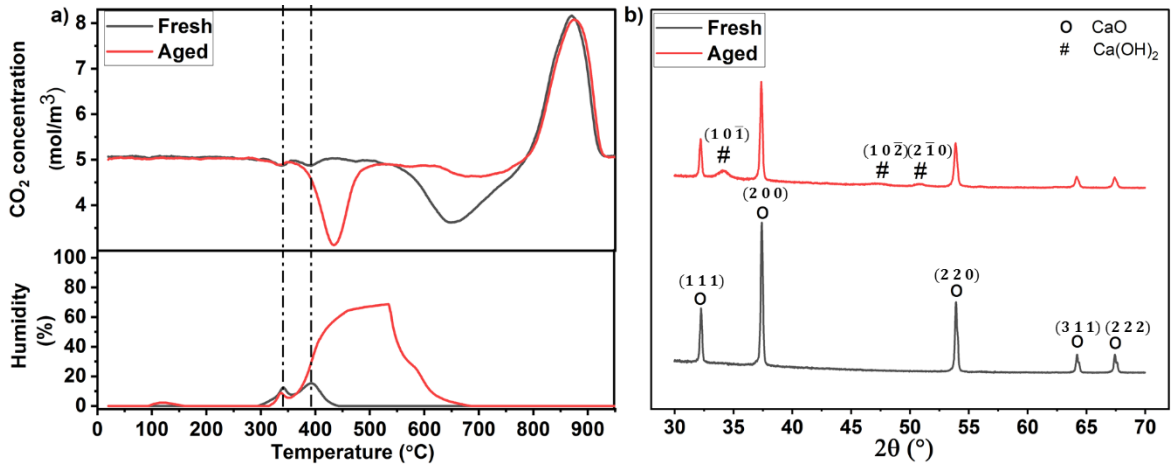

Figure 3.6. Effect of initial $Ca(OH)_2$ content on TPC-TPDC behavior (10% CO_2 in nitrogen with heating rate at 5 °C/min). a) CO_2 concentration and humidity of the exhaust gas during the temperature rise. b) Initial X-ray diffraction patterns of CaO. The "Fresh" scan is for CaO right after $Ca(OH)_2$ thermal decomposition. The "Aged" scan is for CaO after 1 day of exposure to ambient air at room temperature.

Furthermore, comparing the first and second TPC-TPDC profiles for CaO (**Figure 3.7**), we can see that the early carbonation peaks are gone in the second heating. Before the second heating step, the sample was cooled from 950 °C under pure dry N_2. If the early carbonation peaks resulted from chemisorption on CaO surface, they should not depend on the amount of hydroxide. Thus, these peaks should be related to carbonation of adventitious $Ca(OH)_2$.

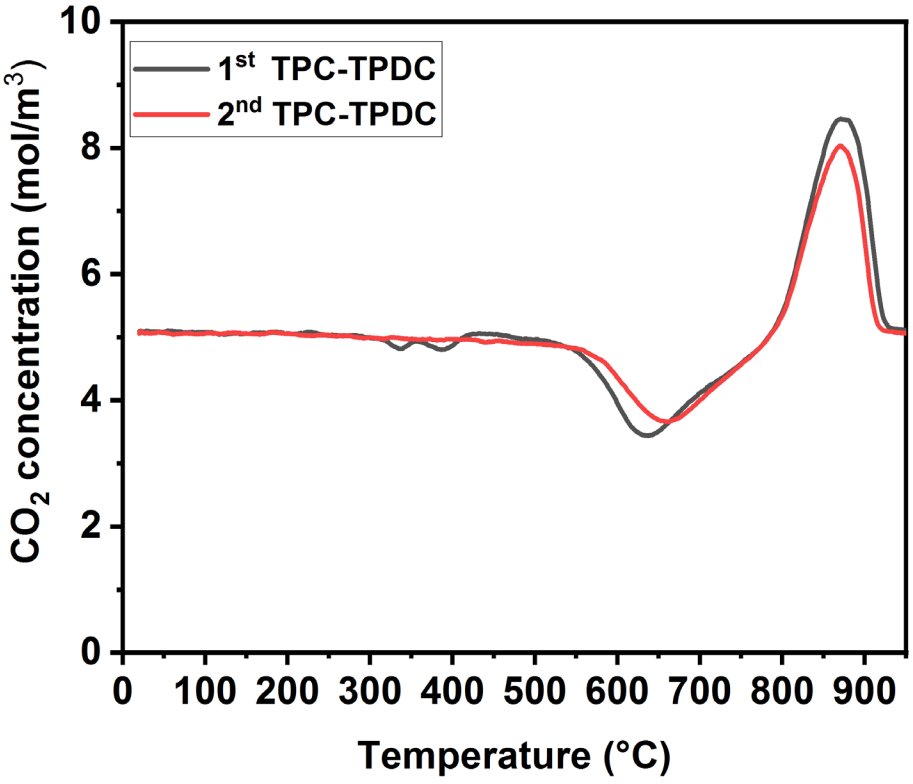

Figure 3.7. Back-to-back TPC-TPDC for CaO under 10% CO_2 and 5 °C/min heating rate.

3.2.4.5 Behavior of calcium-based ternary oxide sorbents

Figure 3.8 shows TPC-TPDC for calcium oxide and calcium metal oxide sorbents under four different concentrations of CO_2. In general, we can see that the inversion temperature increases under higher CO_2 concentrations. This agrees with the exothermic nature of the carbonation reaction. The inversion temperature will rise under higher CO_2 partial pressure (concentration) since the carbonation reaction is exothermic. An increase in CO_2 concentration also increased the CO_2 adsorption amount for all sorbents (**Table 3.3**).

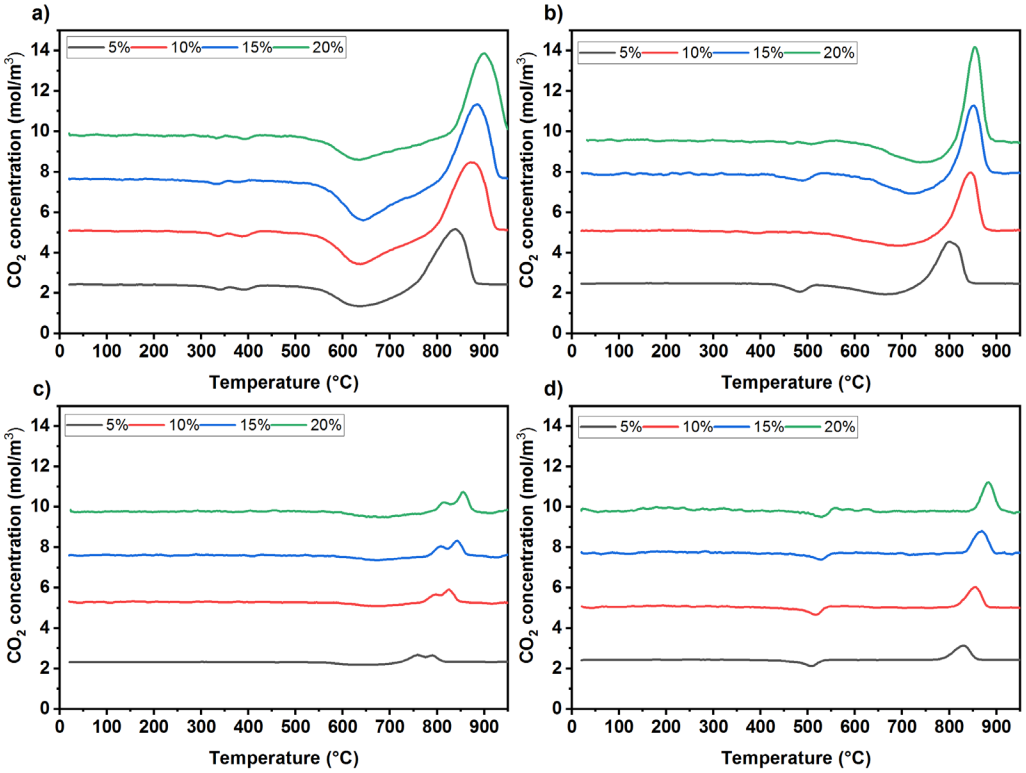

Figure 3.8. TPC-TPDC under 4 different CO_2 levels: 5% (black), 10% (red), 15% (blue), and 20% (green). Heating rate was 5 °C/min for all. a) CaO, b) Ca_2CuO_3, c) $Ca_3Co_4O_9$ and d) $Ca_2Fe_2O_5$.

Table 3.3. CO_2 uptake and sorbent conversion for CaO, Ca_2CuO_3, $Ca_3Co_4O_9$ and $Ca_2Fe_2O_5$ in various CO_2 concentrations. Sorbent mass = 0.5 g.

Sorbent	m_{Ca} (g)	m_{max} (g CO_2/g sorbent)	CO_2 concentration (%) (±1)	CO_2 uptake (g CO_2/g Sorbent)	Sorbent conversion (%)
CaO	0.357	0.785	5	0.346	44
			10	0.466	59
			15	0.47	60
			20	0.476	61
Ca_2CuO_3	0.209	0.460	5	0.196	43
			10	0.246	53
			15	0.26	57
			20	0.296	65
$Ca_3Co_4O_9$	0.120	0.264	5	0.036	14
			10	0.04	15
			15	0.05	19
			20	0.066	25
$Ca_2Fe_2O_5$	0.147	0.326	5	0.048	15
			10	0.056	17
			15	0.062	19
			20	0.064	20

Figure 3.8a reports TPC-TPD profiles for CaO with four different concentrations of CO_2. In each experiment, early carbonation was observed, showing the present of $Ca(OH)_2$ in the samples. The amount of adsorbed CO_2 into the CaO was in the range of 0.35 to 0.48 g CO_2/g sorbent. Considering the theoretical capacity of CaO, 0.79 g CO_2/g sorbent, we can see that the complete carbonation did not occur. The incomplete carbonation is attributed to the formation of a $CaCO_3$ outer layer surrounding the CaO core. This layer is a barrier for CO_2 reaction with inner CaO hindering additional carbonation [87].

Figure 3.8b shows the TPD-TPDC graphs for Ca_2CuO_3. Compared to CaO, lower inversion temperatures were observed, suggesting the possibility of low temperature decarbonation. The CO_2 uptake for this sorbent was in the range of 0.2 to 0.3 g CO_2/g sorbent.

Although the absolute CO_2 uptake amounts of Ca_2CuO_3 were less than CaO, the sorbent's conversion was almost the same for Ca_2CuO_3 and CaO (**Table 3.3**).

Figure 3.8c shows $Ca_3Co_4O_9$ performance during the TPD-TPDC experiment. The sorbents had lower inversion temperatures compared to Ca_2CuO_3 and CaO. Interestingly, unlike the other sorbents, two distinct peaks were observed during the decarbonation process. These two peaks could be related to CO_2 released from sites with different binding energies [130]. As described in the experimental section, the formation of pure $Ca_3Co_4O_9$ was not possible at 900 °C; so, we had to lower the calcination temperature to 800 °C to synthesized pure $Ca_3Co_4O_9$. We speculate that in-situ second phase formation results in the two CO_2 release peaks since other Ca-Co-O compounds readily form at high temperatures. The amount of CO_2 uptake and sorbent conversion was lower than Ca_2CuO_3 and CaO.

Among all sorbents, $Ca_2Fe_2O_5$ had the highest inversion temperatures (**Figure 3.8d**). Its carbonation started at a lower temperature than CaO, Ca_2CuO_3 and $Ca_3Co_4O_9$; however, the decarbonation process started at the highest temperature. As a result, the sorbent is not suitable for cycling. The sorbent conversion was also low compared to CaO and Ca_2CuO_3.

The temperatures of "c" points and "d" points during TPC-TPDC are depicted in **Figure 3.9**. "c" point is for the maximum CO_2 uptake rate, whereas "d" point is for the maximum CO_2 release rate. $Ca_2Fe_2O_5$ had the lowest T_c, while Ca_2CuO_3 had the highest one (**Figure 3.9a**). On the other hand, $Ca_3Co_4O_9$ had the lowest T_d, while CaO had the highest (**Figure 3.9b**). The difference between these two temperatures, $T_d - T_c$, is important as the most effective carbonation and decarbonation process can be conducted in this range with high uptake and release rates. The smaller value of $T_d - T_c$ will result in a lower energy cost in temperature cycling operation. Therefore, Ca_2CuO_3 and $Ca_3Co_4O_9$ sorbents can be good candidates for the temperature swing

process while $Ca_2Fe_2O_5$ is not (**Figure 3.9c**). Although $Ca_3Co_4O_9$ had a small temperature window of $T_d - T_c$, its CO_2 uptake was too low to be effective as a CO_2 sorbent.

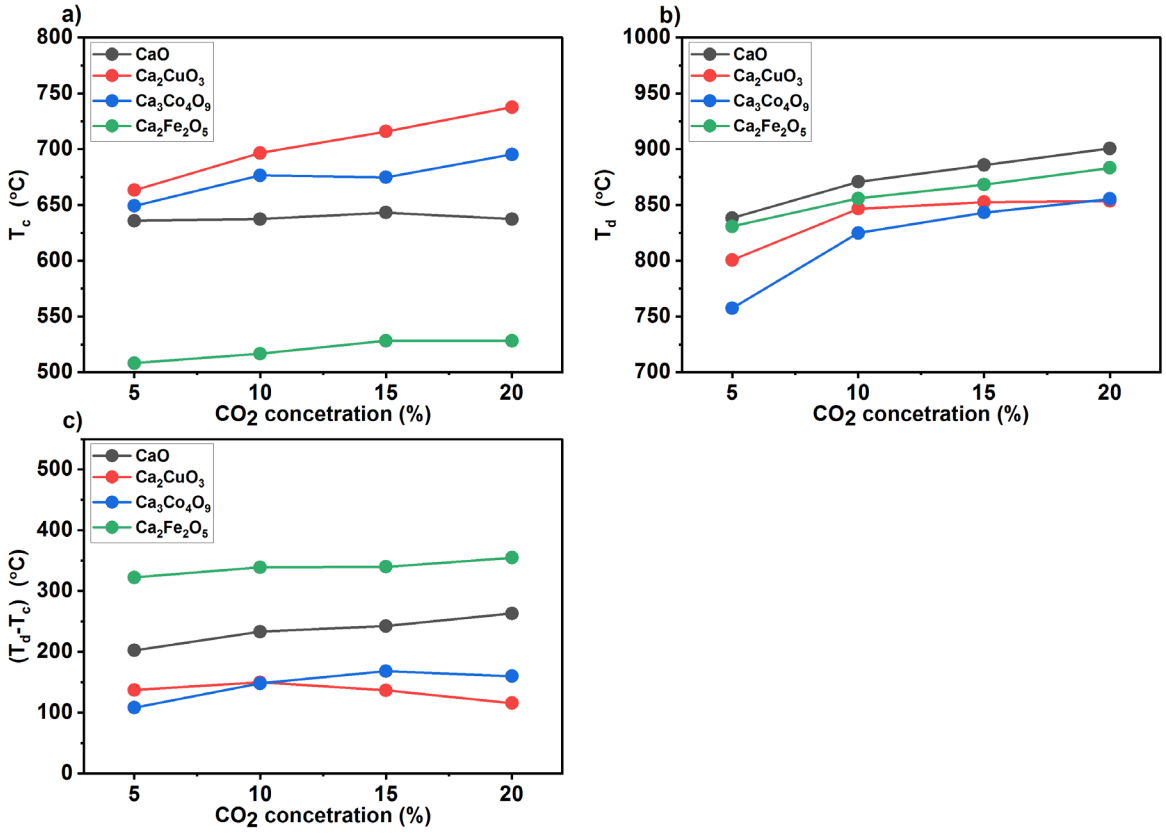

Figure 3.9. Temperature profile as function of CO_2 concentration. a) Maximum carbonation rate temperature. b) Maximum decarbonation rate temperature, and c) the difference between the two temperatures.

Figure 3.10 illustrates the decarbonation enthalpy calculation for the sorbents. The lines show linear fits to inversion temperatures for various sorbents. Four input CO_2 levels were used to get the inversion temperatures where the carbonation rate equals the decarbonation rate. The region above a line shows the carbonation-preferred condition, while the decarbonation-preferred region

lies below the line. The enthalpy value of CaO is in good agreement with a previous report [131]. We found that the calculated enthalpy values of all the sorbents were close to one another. This agreement suggests that the active phase is, as expected, CaO for Ca_2CuO_3, $Ca_3Co_4O_9$, and $Ca_2Fe_2O_5$ in the carbonation process.

After cooling down the samples under CO_2 (10%), we took the X-ray diffraction patterns of the samples as shown in **Figure 3.11**. The Rietveld refinement was performed by MAUD software on these patterns. The results are summarized in **Table 3.4**, and the final phases were identified for each sorbent in **Figure 3.11**. The "x" marks show the experimental XRD data, and the colored lines indicate the calculated profile by Rietveld refinement. The CIF files were obtained from COD [132-138]. The following of COD IDs were used for Rietveld refinement 1000044 (CaO), 1010928 ($CaCO_3$), 1000063 (Cu_2O), 1533087 (CoO), 1008777 ($Ca_2Fe_2O_5$), 1011240 (Fe_2O_3). Only calcium carbonate was observed by X-ray diffraction. No other metal carbonates were observed in this study. After the complete TPC-TPDC process (cooled down under 5~20% CO_2), the X-ray diffraction results show complete decomposition for Ca_2CuO_3 and $Ca_3Co_4O_9$ while $Ca_2Fe_2O_5$ had a partial decomposition. The final phases for Ca_2CuO_3 and $Ca_3Co_4O_9$ were the combination of calcium oxide, metal oxide (Cu_2O and CoO, respectively), and calcium carbonate. At the end of the experiment, unlike the other sorbents, $Ca_2Fe_2O_5$ still showed ternary oxide diffraction peaks with some CaO and Fe_2O_3. This demonstrates the phase stability of $Ca_2Fe_2O_5$. This high phase stability was observed previously [139], and it resulted in insufficient decomposition limiting the sorbent reactivity. This phase evolution can explain the highest inversion temperature of the sorbent, the only oxide that had the original persisting phase.

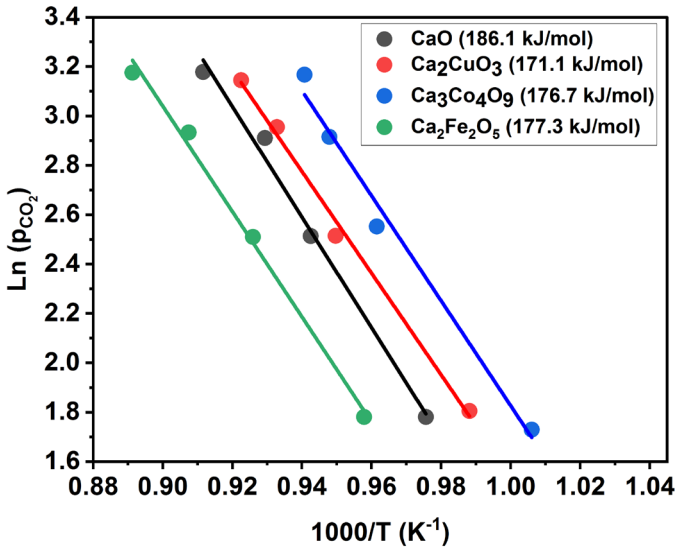

Figure 3.10. Enthalpy from inversion temperatures for CaO, Ca_2CuO_3, $Ca_3Co_4O_9$ and $Ca_2Fe_2O_5$.

Table 3.4. The result of Rietveld Refinement (using Maud software) for the sorbents after TPC-TPDC.

Sorbent	Content	Weight (%)	Crystal size (nm)	Rwp (%)
CaO	CaO	76.7	167	3.4
	$CaCO_3$	23.3	99	
Ca_2CuO_3	CaO	64	403	3.2
	$CaCO_3$	1.4	100	
	CuO	34.6	85	
$Ca_3Co_4O_9$	CaO	30.2	247	1.8
	$CaCO_3$	5.3	100	
	CoO	64.5	255	
$Ca_2Fe_2O_5$	CaO	19.7	105	3.7
	$CaCO_3$	9.3	102	
	$Ca_2Fe_2O_5$	40.1	82	
	Fe_2O_3	30.9	100	

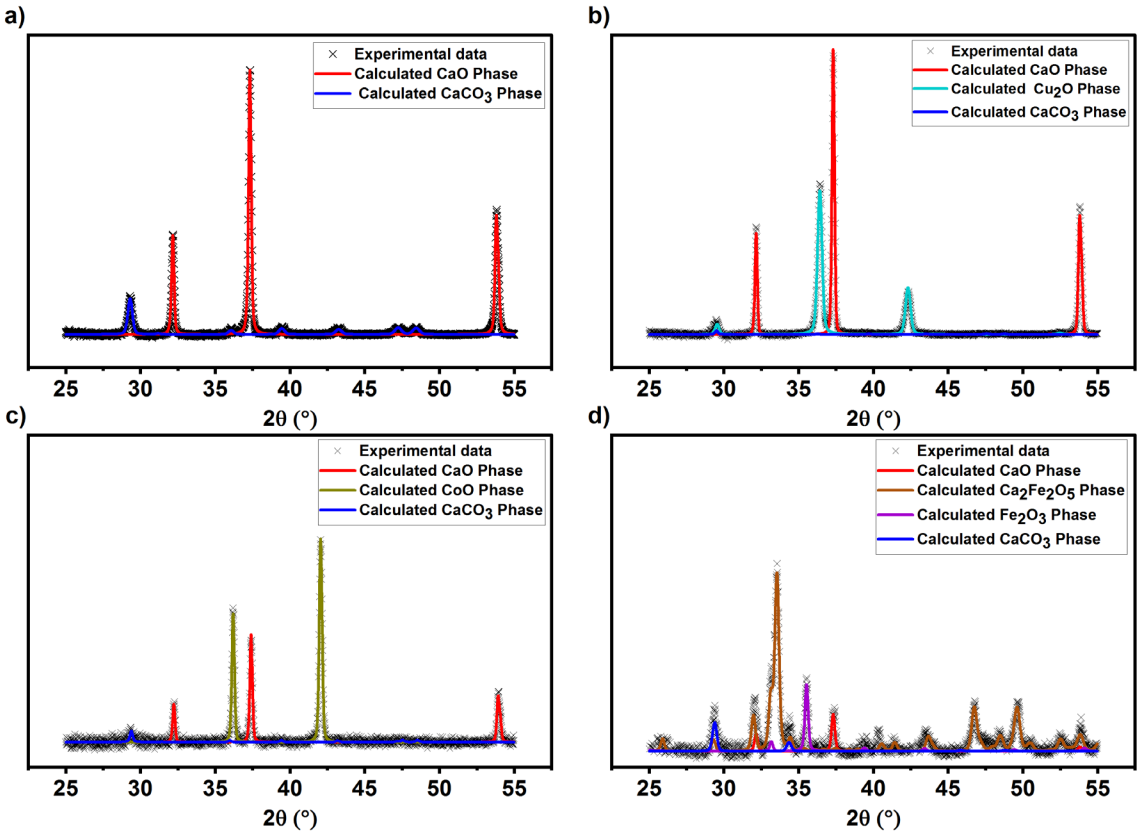

Figure 3.11. Final phases of different samples after cooling down under 10% CO_2. a) CaO, b) Ca_2CuO_3, c) $Ca_3Co_4O_9$ and d) $Ca_2Fe_2O_5$.

The pore structure of the sorbents was investigated to have a better understanding of the sorbent behavior. **Figure 3.12** shows the pore size distribution of the spent samples after TPC-TPDC. This distribution was obtained by nitrogen physisorption (Quantachrome NOVA 2200e), based on density functional method (NLDFT option in NovaWin 10.01 software from Quantachrome) [140]. We can see that CaO and Ca_2CuO_3 have a larger population of large diameter (d > 10 nm) pores than $Ca_3Co_4O_5$ and $Ca_2Fe_2O_5$. This result agrees with the higher uptake of CO_2 for CaO and Ca_2CuO_3. A greater population of large pores decreases the mass transport barrier in gas-solid reaction leading to higher CO_2 uptake [94, 141-144].

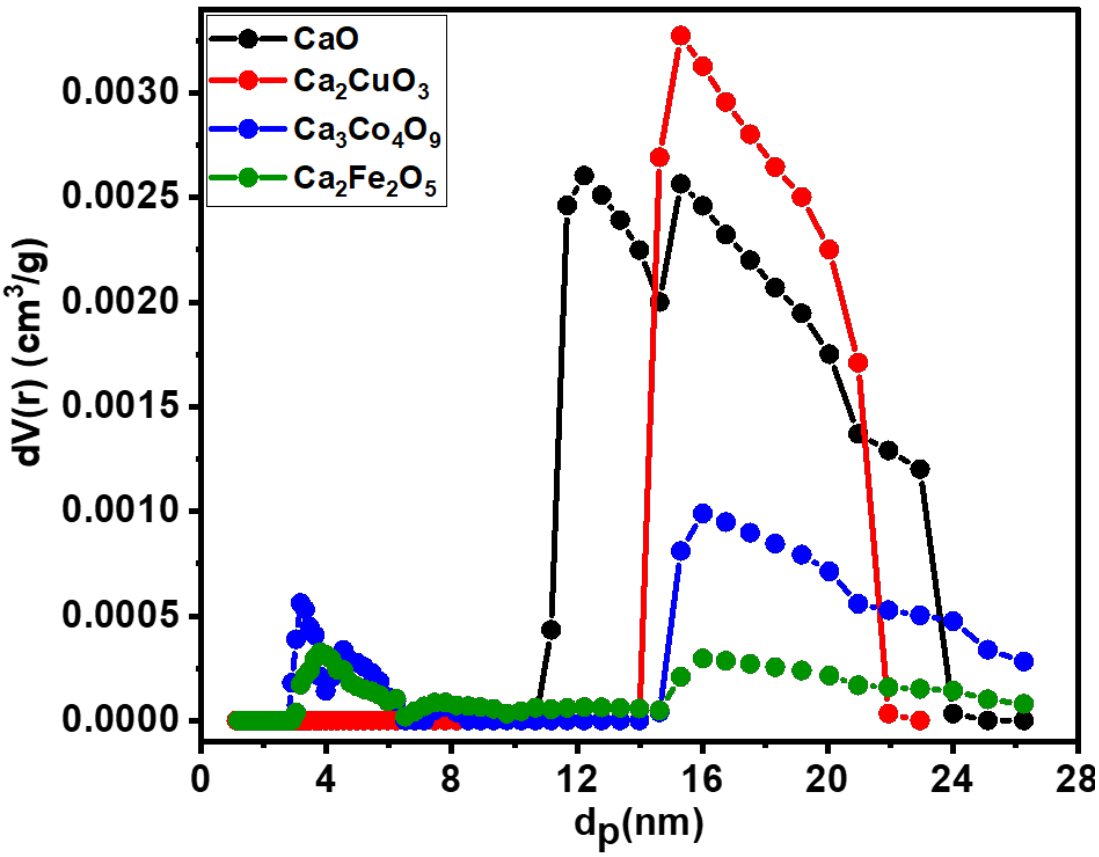

Figure 3.12. Pore size distribution analyzed by density functional method. All samples were analyzed after the TPC-TPDC test.

Due to the disadvantageous pore structure evolution found for $Ca_2Fe_2O_5$ and $Ca_3Co_4O_9$, we excluded these sorbents for further investigation and focused on Ca_2CuO_3 for the following temperature swing operations.

From the temperature swing experiment under 10% CO_2 flow, we noticed that Ca_2CuO_3 regeneration is faster than CaO regeneration showing sharper mass loss peaks in **Figure 3.13**. We check the temperature swing behavior of Ca_2CuO_3 since this was the only ternary oxide with high enough sorbent conversion, as noted in Table 1. The performance of the sorbents was investigated in the 700 to 800 °C temperature window during 6 cycles of carbonation/decarbonation. The

duration of each cycle was 60 minutes. **Figure 3.13** shows satisfactory CO_2 capacity retention for both sorbents under the chosen experimental condition. The positive peaks show the carbonation, while the negative peaks indicate the decarbonation. The highest mass gain rates for both sorbents were found in the first carbonation cycles due to carbonation during the temperature rise from room temperature to 700 °C. The last CO_2 uptake peaks are due to carbonation during the cooling down step. They are shaded in gray in **Figure 3.13**. This last CO_2 uptake amount was 0.129 g CO_2/g Ca for CaO (**Figure 3.13a**). For Ca_2CuO_3, the last CO_2 uptake amount was 0.134 g CO_2/g Ca (**Figure 3.13b**). Ca_2CuO_3 clearly maintained CO_2 capacity as well as CaO under this temperature swing condition. Notably, the Ca_2CuO_3 sorbent regeneration rate, shown as negative peaks in **Figure 3.13**, was always higher than the CaO sorbent regeneration rate during the temperature swing experiment. The facile regeneration of Ca_2CuO_3 is advantageous for calcium looping: We can regenerate our sorbent in a shorter time, reducing energy consumption.

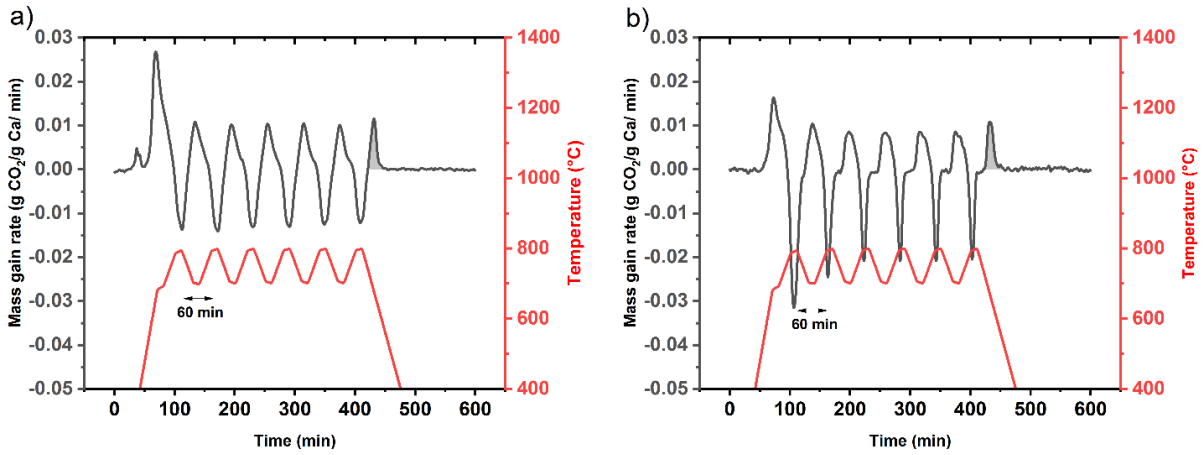

Figure 3.13. Temperature swing carbonation/decarbonation kinetics comparison under 10% CO_2 for 6 cycles. a) CaO mass change rate. b) Ca_2CuO_3 mass change rate. One cycle was 60 minutes long: 10 min of carbonation at 700 °C, 20 min for heating up, 10 min of decarbonation at 800 °C, and 20 min for cooling down.

Furthermore, we conducted the temperature swing at the temperatures of maximum carbonation and decarbonation rates (640–900 °C for CaO and 740–850 °C for Ca_2CuO_3). **Figure 3.14** shows the sorbent performance in this optimized temperature window. With the same heating and cooling rates of 10 °C/min, the duration of each cycle for CaO and Ca_2CuO_3 were different–62 and 42 minutes–since they have different widths of the temperature windows. The sorbents were held at T_c for 10-minute carbonation and at T_d for 10-minute decarbonation. It should be noted that the condition of the first carbonation differs from all other carbonation steps. The carbonation started at T_c for the first carbonation step, while the carbonation started near the inversion temperature for all other carbonation steps (during cooling down from T_d to T_c).

The carbonation proceeds from T_c to the inversion temperature in this cycling scheme making the carbonation duration per cycle longer than the nominal 10 minutes (the preset dwell time at T_c). The same scenario applies to regeneration leading to more than 10 minutes of decarbonation. We can get the average carbonation rate by integrating the area of the positive peaks and dividing them by total carbonation time. The values of 0.0080 and 0.0171 g CO_2/g Ca/min were found for CaO and Ca_2CuO_3 (**Table 3.5**). The average decarbonation rates were 0.0103 g CO_2/g Ca/min for CaO and 0.0165 g CO_2/g Ca/min for Ca_2CuO_3 calculated from the negative peak areas. (**Table 3.6**). These results indicate that Ca_2CuO_3 can outperform CaO for calcium loop processing if we operate both sorbents within their respective optimized temperature window (between T_c and T_d).

Moreover, we can reduce the energy for sorbent regeneration by choosing Ca_2CuO_3 sorbent operation temperature prudently since Ca_2CuO_3 at 850 °C shows a higher regeneration rate than CaO at 900 °C does.

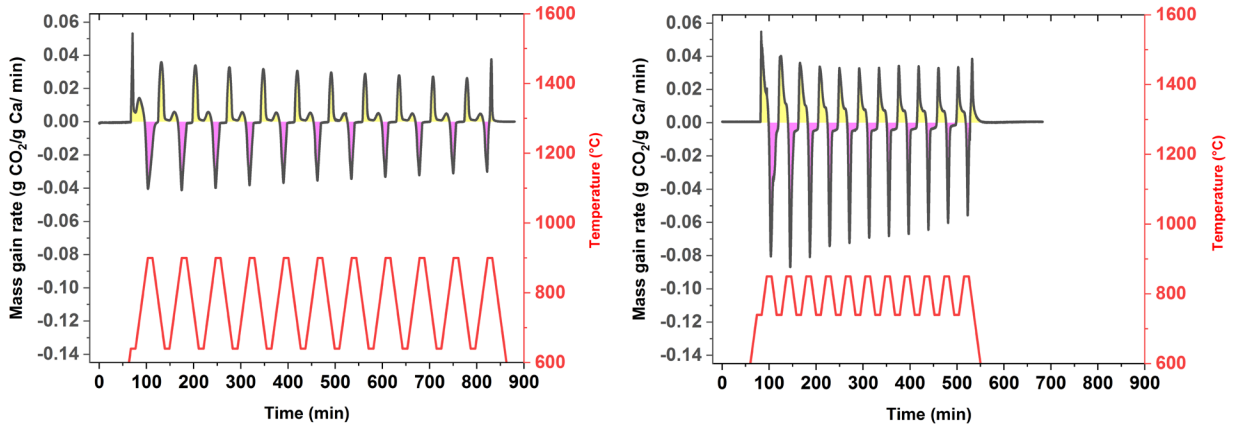

Figure 3.14. Temperature swing carbonation/decarbonation kinetics comparison under 20% CO_2. a) CaO mass change rate. b) Ca_2CuO_3 mass change rate. The experiments were done between T_c and T_d of each sorbent.

Table 3.5. The amount of CO_2 uptake in each cycle for CaO and Ca_2CuO_3 when the sorbents were cycled between T_c and T_d.

Cycle number	**CaO (g CO_2 / g Ca)**	**Ca_2CuO_3 (g CO_2 / g Ca)**
1	0.471	0.620
2	0.401	0.496
3	0.367	0.424
4	0.342	0.384
5	0.320	0.353
6	0.305	0.332
7	0.287	0.313
8	0.279	0.306
9	0.265	0.300
10	0.256	0.299
11	0.247	0.293
12	0.144	0.214
specific CO_2 uptake (g CO_2 / g Ca/ min)	**0.0080**	**0.0171**

CaO total carbonation time=460 min
Ca_2CuO_3 total carbonation time= 253 min

Table 3.6. The amount of CO_2 release in each cycle for CaO and Ca_2CuO_3 when the sorbents were cycled between T_c and T_d.

Cycle number	**CaO (g CO_2 / g Ca)**	**Ca_2CuO_3 (g CO_2 / g Ca)**
1	0.462	0.616
2	0.391	0.494
3	0.358	0.412
4	0.331	0.375
5	0.310	0.346
6	0.291	0.324
7	0.274	0.299
8	0.258	0.0282
9	0.244	0.264
10	0.231	0.254
11	0.182	0.204
specific CO_2 release (g CO_2 / g Ca/ min)	**0.0103**	**0.0165**

CaO total decarbonation time= 323 min
Ca_2CuO_3 total decarbonation time= 219 min

Even though we were able to obtain pore size distribution from nitrogen adsorption-desorption isotherms, this characterization tool can only detect micropores and mesopores. Using SEM, we were able to observe macrospores. After the 11th temperature cycle for CaO and Ca_2CuO_3, we collected the SEM images of the spent sorbents to check their morphology evolution from the fresh ones (**Figure 3.15**). The excessively large pore structure can be seen in the fresh Ca_2CuO_3 while there are fewer large pores in the fresh CaO. The large pore structure can allow facile gas phase transport of CO_2 to the sorbent surface and consequently enhance the carbonation.

Notably, Ca_2CuO_3 maintained some large pores although sintering was observed for both sorbents. This is because of the presence of the in situ generated Cu_2O phases partially mitigating the sintering. The lower maximum temperature for Ca_2CuO_3, 850 °C, is another reason for less

sintering. The higher decarbonation rate of Ca_2CuO_3 may be related to the sorbent's large pores even after undergoing several temperature cycles. CO_2 can leave the sorbent easier when there are large pores present. The SEM images suggest the importance of the pore size and distribution over the surface area.

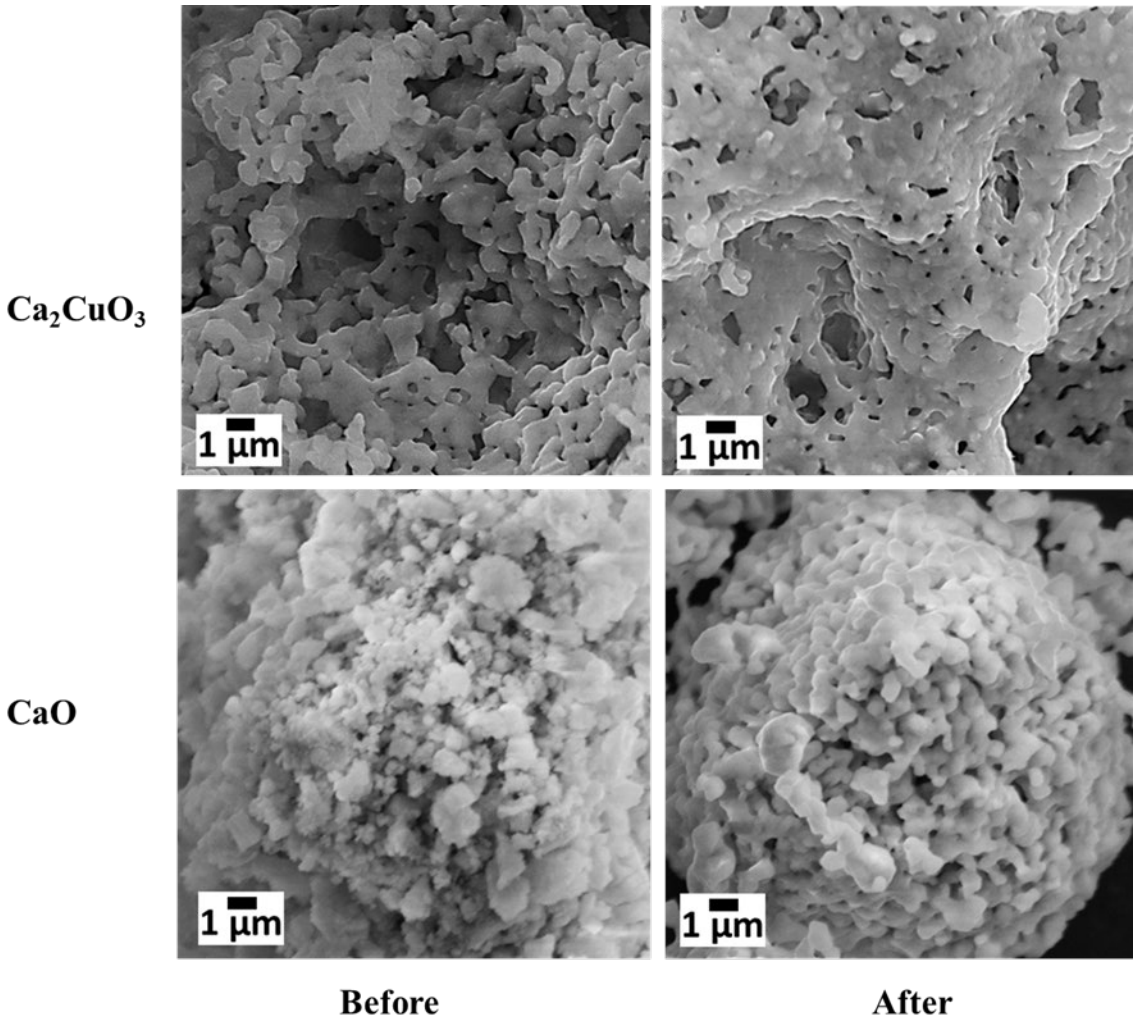

Figure 3.15. Morphology changes of Ca_2CuO_3 and CaO sorbents after the temperature swing carbonation/decarbonation process.

3.3 Conclusion

The behavior of three calcium-based ternary oxide sorbents was studied. Ca_2CuO_3 and $Ca_3Co_4O_9$ showed lower inversion temperatures compared to CaO, while this temperature was higher for $Ca_2Fe_2O_5$. After the TPC-TPDC experiment, it was found that Ca_2CuO_3 and $Ca_3Co_4O_9$ were completely decomposed to CaO and their own metal oxides while a significant proportion of $Ca_2Fe_2O_5$ was not reactive during the experiment and showed up in the X-ray pattern. This limited decomposition of $Ca_2Fe_2O_5$ is undesirable since the active calcium oxide phase does not form readily.

The lower inversion temperature of a sorbent provides the benefit of lower energy demand for regeneration. Ca_2CuO_3 and $Ca_3Co_4O_9$ are found to be suitable for a temperature swing process since they had narrow temperature windows between maximum carbonation and decarbonation rates. However, $Ca_3Co_4O_9$ had a small amount of CO_2 uptake in TPC-TPDC experiment, limiting its practical applicability in CO_2 capture. We ruled out $Ca_2Fe_2O_5$ due to high inversion temperature and $Ca_3Co_4O_9$ due to small CO_2 uptake.

Ca_2CuO_3 showed a competitive sorbent performance under a temperature swing operation between 700 °C, CO_2 uptake temperature, and 800 °C, CO_2 release temperature. We have shown that the regeneration of this sorbent was faster than CaO regeneration in the tested temperature swing cycles. The CO_2 capacity per calcium content was close to CaO after the temperature swing test.

The temperature swing experiments between T_c, the highest carbonation rate temperature, and T_d, the highest decarbonation rate temperature, showed that Ca_2CuO_3 has higher average carbonation and decarbonation rates than CaO. The higher regeneration rate of Ca_2CuO_3 is related to larger pores in this sorbent. Due to the present of Cu_2O and lower regeneration temperature, Ca_2CuO_3 does not sinter as much as CaO.

In all experiments, Ca_2CuO_3 showed a higher regeneration rate compared to the other tested sorbents. Even at 850 °C, Ca_2CuO_3 had a higher regeneration rate than CaO at 900 °C. The low regeneration temperature makes Ca_2CuO_3 a promising sorbent that can reduce energy consumption in calcium looping.

Chapter 4 Solid-state decomposition of Ca_2CuO_3 enhances its CO_2 reactivity and cycle stability

Abstract

The carbonation/decarbonation performance of Ca_2CuO_3 with various decomposition degrees were compared to CaO (a typical sorbent for post combustion CO_2 capture). For the mixture of calcium and copper, three different sorbents, Non-decomposed (N-CCO), Partially decomposed (P-CCO), and Fully decomposed Ca_2CuO_3 (F-CCO) were identified by X-ray diffractometry. Homogenous mixing between copper and calcium atoms confirmed by energy-dispersive X-ray spectroscopy (EDS) analysis. We found that a higher degree of carbonating/decarbonation achievement when a high content of copper (the inert phase) was present in the sorbent. High conductivity of copper correlated to the efficient performance of sorbent. Through a temperature-resolved experiment, we realized lower carbonation temperatures for F-CCO (400 °C) compared to N-CCO (below 600 °C was negligible). F-CCO demonstrated better performance in the regeneration stage as well. At 600 °C a significant recovery of 85% was achieved for F-CCO compared to 16% for N-CCO. Through a time-resolved experiment at 800 °C, F-CCO showed a higher degree of carbonation compared to P-CCO and N-CCO. The conversion of F-CCO reached to 52% after 26 min while the conversion of 46% and 48% were achieved for P-CCO and N-CCO respectively after 39 min. The F-CCO sorbent showed extremely fast regeneration rate at 800 °C compared to the other sorbents. The regeneration of F-CCO completed in less than 3.5 min while for the regenerate completion of other sorbents did not achieve even after 26 min (95% for P-CCO and 78% for N-CCO). Finally, the average conversion of the sorbents over 10 cycles were estimated 79.2%, 44.7% and 45.5% for F-CCO, P-CCO and

CaO when the sorbent regenerated under 4% H_2. This amount was 35.7% and 44.7%, for N-CCO and CaO when air used as regeneration gas.

4.1 Introduction

CO_2 is the major greenhouse gas that causes climate change. Since the industrial revolution the amount of CO_2 concentration in the atmosphere increases by 47% [8, 59]. It has been projected that if CO_2 emission does not reduce extremely, the global warming of 1.5 to 2 °C will occur in 21st century [2]. Burning fossil fuel for power generation in the industry is the major source of CO_2 emissions [145, 146]. The vast energy demand in industry makes it very hard to eliminate fossil fuel from reliable energy sources. Until the time when energy can be efficiently obtained from clean and sustainable sources, Carbon Capture and Storage (CCS) methods need to be improved to reduce CO_2 emission and consequently mitigate the climate change. CCS can be classified into three main categories: pre-combustion, oxy-fuel combustion, and post-combustion [57].

The post-combustion carbon capture is desirable since it can be retrofitted into current power plants without significant changes in the equipment [58, 63, 147]. Two main methods are used in post-combustion carbon capture: amine scrubbing and calcium looping (CaL). Although amine scrubbing is more mature in industrial usage, calcium looping provides better efficiency for CO_2 capture [35, 148-152].

CaO, the main active component in CaL process, can be derived from natural limestone. The abundancy and high CO_2 capture capacity of this sorbent make it favorable for carbon capture. Despite these prominent benefits, CaO loses its surface area from sintering during regeneration step and cannot be used in a long-term operation [38, 153]. Therefore, a well-designed modification is necessary to improve the performance of this sorbent.

Many efforts have been made to enhance the cycle stability of the CaO-based sorbents [75, 76, 81, 96, 100, 102, 114, 131]. Some methods focused on the structural changes via ball milling [80, 81, 94], electrospinning [110], and acid-based treatment [154] to increase the pore size and surface area. This microstructure engineering will consequently enhance kinetics and conversion [88, 143]. Although the structural change is beneficial in increasing the sorbents conversion initially, the cycle stability problem persists [94].

Another approach for cycle stability relies on metal oxide incorporation into CaO. The idea is to include metal oxides of high Tammann temperatures to fabricate composite solid sorbents that can resist sintering at high temperatures [54, 56, 155-157]. The metal oxide inclusions deter facile grain growth and densification of the solid sorbent by slowing down the grain boundary movement. In most of the cases, the added metal oxides remain inert during the carbonation/decarbonation process preventing sintering for better cycle stability [158, 159].

Despite extensive study on CaO-based sorbent improvement using metal oxide incorporation, there is no study that directly focuses on the in situ generation of metallic particles from CaO-based solid sorbents. If metallic particles are incorporated into CaO, they will result in sintering resistance in the composite sorbent. In addition, due to high thermal conductivity of metal, the heat transfer in the sorbent will be enhanced. We can expect that the facile heat transfer will increase the carbonation or decarbonation reaction rate under the given thermodynamic condition. Among many available metals, Cu suits this purpose well due to its abundancy and high thermal conductivity [124, 160, 161]. The melting point and thermal conductivity of copper and copper oxides in literatures are summarized in **Table 4.2**.

In this work, we first synthesized Ca_2CuO_3 where calcium and copper atoms are locked in an oxide lattice with atomic-level dispersion. Then using hydrogen, we reduced Ca_2CuO_3 to CaO

and Cu. CaO provides the active sites for CO_2 capture, and Cu is dispersed in the CaO matrix for the sintering resistance and facile heat transfer. To see the effect of solid-state decomposition on the performance of the resultant sorbent, three different samples were synthesized: single ternary oxide (Ca_2CuO_3), partially decomposed oxide, and fully decomposed oxide. Then we studied the performance of these sorbents on carbonation and decarbonation.

4.2 Experimental

4.2.1 Sorbent preparation

4.2.1.1 CaO

Calcium formate (Alfa Aesar, 98%) was heated to 900 °C (heating rate ~ 10°C/min) under atmospheric condition and kept for 3 hours. After cooling down, X-ray diffraction confirmed complete conversion of calcium formate into CaO.

4.2.1.2 Ca_2CuO_3 (N-CCO)

Stoichiometric amounts of calcium nitrate tetrahydrate (BeanTown Chemical 99%) and copper (II) acetate monohydrate (ACS reagent, ≥98% Sigma-Aldrich) were dissolved in water. After complete dissolution, the solution was heated to form a gel. This gel was then calcined at 900 °C for 3 h in air. The detail of the synthesis can be found in the previous work by the author [162].

4.2.1.3 Fully decomposed Ca_2CuO_3 (F-CCO)

The decomposition of the Ca_2CuO_3 were conducted in a severe condition. 100 mg of the sample was loaded into a ceramic boat. This boat was placed in a quartz tube (inner diameter of 0.86 inches and length of 24 inches) that went into a tube furnace. Under 4% H_2 in N_2 atmosphere, the sample was heated to 800 °C with heating rate of 10 °C/min. The sorbent was kept at 800 °C

for 12 h before cooling down to the room temperature. X-ray diffraction patterns of the sample indicated complete decomposition of Ca_2CuO_3 into CaO and Cu showing no CuO or Cu_2O phases.

4.2.1.4 Partially decomposed Ca_2CuO_3 (P-CCO)

The Ca_2CuO_3 (N-CCO) was loaded on XRK 900 reactor stage (Anton Paar, designed for in situ X-ray diffraction study) to be heated to 800 °C with heating rate of 10 °C/min under % 4 H_2 in N_2. When the sample reached target temperature, the in situ X-ray diffraction pattern was taken to confirm partial decomposition of Ca_2CuO_3. There were some Cu_2O particles left in the sample that did not convert to Cu. The partially decomposed sorbent was never cooled down. It was tested in isothermal kinetics studies and carbonation-regeneration cycling studies.

4.2.2 Sorbents characterization

We used AXRD powder diffraction system (Proto manufacturing), Quantachrome NOVA 2200e (Anton Paar) and EVO50 Scanning Electron Microscope (Zeiss) to characterize phase compositions, pore size distribution, and element analysis respectively. Rietveld refinement was conducted on X-ray diffraction patterns using MAUD software [163] to calculate phase contents in the sorbents [94, 164]. We obtained the pore size distribution by applying Density Functional Theory method on N_2 physisorption data points (NLDFT option in NovaWin 10.01 software from Quantachrome) [140]. The surface area of the sorbents was acquired by BET method. The elemental analysis was conducted by Energy-dispersive X-ray spectroscopy (EDS) mapping.

4.2.3 CO_2 capture test

4.2.3.1 Ex situ experiment

We examined the carbonation behavior N-CCO and F-CCO under pure CO_2. The sorbents were individually loaded into the quartz tube and put into a tube furnace. We heated up the furnace with ramping rate of 10 °C/min to 800 °C under pure CO_2. They were kept at this temperature for

12 h and cooled down to room temperature. We collected the X-ray diffraction patterns of the sorbents after the carbonation.

4.2.3.2 In situ experiment

For testing the performance of the sorbents, we monitored the behavior of the sorbent under carbonation and regeneration. 100 mg of each sorbent was loaded to ceramic holder (14 mm diameter 3mm height, the schematic can be found in the supporting information of the reference [94]) of the XRK 900 reactor. The flowrate of gas was controlled using MKS G series. The phase change of the sorbent monitored using in situ X-ray diffraction at high temperature. The Rietveld refinement was conducted to calculate the weight percentage of the phase content in the sorbent. Then, the sorbent conversion was calculated using the following equations (MW: molecular weight):

$$\text{CaO, P-CCO and F-CCO: } \frac{wt\%CaCO_3}{wt\%CaO\left(\frac{MW_{CaCO_3}}{MW_{CaO}}\right) + wt\%CaCO_3} \times 100; \quad (4-1)$$

$$\text{N-CCO: } \frac{wt\%CaCO_3}{wt\%CaO\left(\frac{MW_{CaCO_3}}{MW_{CaO}}\right) + wt\%Ca_2CuO_3\left(\frac{2 \times MW_{CaCO_3}}{MW_{Ca_2CuO_3}}\right) + wt\%CaCO_3} \times 100. \quad (4-2)$$

The sorbent recovery was calculated based on following equation:

$$Sorbent\ recovery = \frac{intial\ conversion - conversion\ during\ the\ regeneration}{intial\ coversion} \times 100 \quad (4-3)$$

We also used Scherrer equation [165] for calculating the crystal size of CaO phase of the sorbent

$$Crystal\ size = \frac{K\lambda}{\beta\ Cos\ (\theta)} \qquad (4-4)$$

where K is a shape factor with typical value of 0.93, λ is the wavelength of X-ray (1.5406 Å for Cu), β is the line boarding at half of the maximum intensity in radians, and θ is Bragg angle in radians.

4.2.3.2.1 Temperature-resolved carbonation and regeneration experiment

We designed a temperature-resolved experiment to comprehend the carbonation behavior of N-CCO and F-CCO under pure CO_2. With a heating rate of 10 °C/min, the temperature of XRK900 was raised from room temperature to 300 °C. We kept the sorbents at this temperature for 26 min before taking the 13 min X-ray diffraction scan. The procedure was repeated for higher temperatures up to 800 °C with a 100 °C temperature interval. The sorbents were cooled down under pure CO_2.

We repeated the same heating and date collection procedure for sorbent regeneration. Only the gas flow composition was changed to decarbonate the sorbents. We used air and 4% H_2 for N-CCO and F-CCO samples, respectively. At the end of the regeneration, we cooled the sorbents down under the used regeneration gas.

4.2.3.2.2 Time-resolved carbonation and regeneration experiment

Time-resolved experiments were conducted isothermally at 800 °C to investigate the carbonation and regeneration behavior of N-CCO, P-CCO, and F-CCO. The sorbents were heated to 800 °C under their regeneration gas (N-CCO: air; P-CCO and F-CCO: 4% H_2 in N_2) with a heating rate of 10 °C/min. Once the temperature reached 800 °C, we changed the gas to pure CO_2. The X-ray scans were repeated with no time delay; each scan took 13 min. After taking three

consecutive X-ray scans, the carbonation gas got switched back to the original regeneration gas. We took three more scans back to back to track sorbent regeneration.

4.2.3.2.3 Isothermal stability test

The cycle stability of the sorbents was tested over 10 cycles of carbonation and regeneration at 800 °C. For sorbent carbonation, an MKS mass flow controller was used to flow pure CO_2 at 75 sccm. After 26 min of carbonation, X-ray diffraction patterns were collected for 13 min from 20 to 54.5 2θ degrees. We used air for CaO and N-CCO for sorbent regeneration, while P-CCO and N-CCO were decarbonated in 4% H_2 in N_2 (100 sccm total flow rate). The data collection time scale during sorbent regeneration was the same as the carbonation process.

4.3 Result and discussion

4.3.1 Sorbent characterization

Figure 4.1 shows the X-ray diffraction patterns (XRD) for all sorbents. The XRD of calcined calcium formate indicates a pure crystalline phase of CaO (black line). The formation of Ca_2CuO_3 was confirmed (red line). In situ XRD of partially decomposed Ca_2CuO_3 shows the formation of CaO, Cu, and Cu_2O. The fully decomposed Ca_2CuO_3 had only CaO and Cu. The weight percent of the components obtained by Rietveld refinement were in a good agreement with the stoichiometry calculations. The weight percent of calcium, copper, and oxygen in the Ca_2CuO_3 are 41.8%, 33.1% and 25.0 % respectively based on stoichiometry. Based on the Rietveld refinement, the weight percent of CaO and Cu were calculated 65.8% and 34.2% accordingly for fully decomposed Ca_2CuO_3. Neglecting oxygen in the weight percent calculation (because the amount of oxygen is going to change after decomposition while the amount of calcium and copper will be constant), the weight percent of Ca is 55.8% and Cu is 44.2%. These values were calculated 57.9% and 42.1% respectively based on the Rietveld refinement. The same scenario can be applied

for partially decomposed Ca_2CuO_3. This agreement shows the sorbent will not form any amorphous phase after decomposition. The detail of Miller indices for each peak can be found on **Table 4.1**.

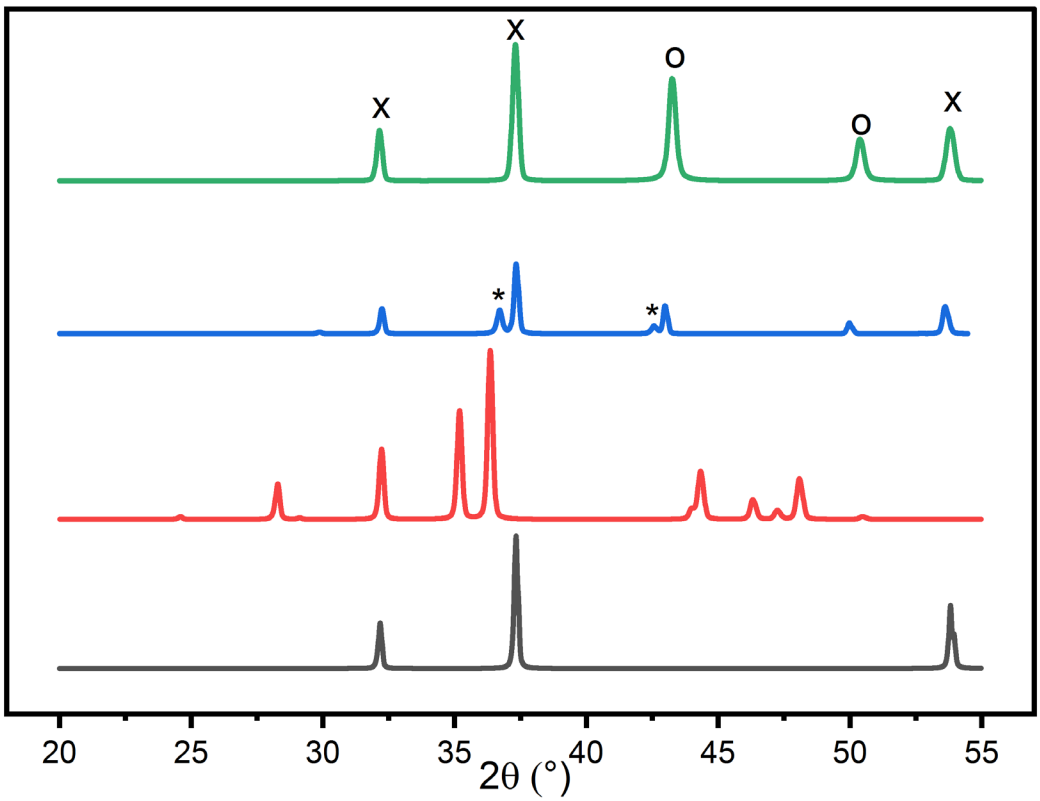

Figure 4.1. X-ray diffraction patterns of the sorbents. Black, red, blue, and green are CaO, N-CCO, P-CCO, and F-CCO respectively. The symbols x, o and * indicate CaO, Cu, and Cu_2O accordingly. All the profiles were taken ex situ except the scan for the partially decomposed Ca_2CuO_3 (P-CCO) which was taken in situ.

Table 4.1. The miller index of each peak in Figure 4.1. the balk, red, blue and green colors show the peaks information of CaO, Ca_2CuO_3, Cu_2O and Cu respectivly. The reference data was obtained from Crystallography Crystallography Open Database [132-138].

CaO		**N-CCO**		**P-CCO**		**F-CCO**	
Peak position (°)	**Miller indices (h k l)**	**Peak position (°)**	**Miller indices (h k l)**	**Peak position (°)**	**Miller indices (h k l)**	**Peak position (°)**	**Miller indices (h k l)**
32.2	1 1 1	24.7	1 1 0	29.9	1 1 0	32.2	1 1 1
37.4	2 0 0	28.4	1 0 1	32.2	1 1 1	37.4	2 0 0
53.9	2 2 0	32.3	3 1 0	36.7	1 1 1	43.3	1 1 1
		35.2	3 0 1	37.4	2 0 0	50.4	2 0 0
		36.4	0 1 1	42.6	2 0 0	53.9	2 2 0
		44	5 1 0	43.3	1 1 1		
		44.4	6 0 0	50.4	2 0 0		
		46.4	5 0 1	53.9	2 2 0		
		47.3	4 1 1				

CaO Ca_2CuO_3 Cu_2O Cu

Figure 4.2 illustrates the elemental analysis using EDS technique. We could observe a uniform distribution of Ca and Cu atoms for N-CCO. This distribution was expected since Ca, Cu, and O needs to bond together in atomic scale to form Ca_2CuO_3. This uniform distribution also was

observed after the decomposing of Ca_2CuO_3 (F-CCO). This is desirable for the sorbent since finely-dispersed copper particles between calcium oxide particles can hinder sintering process during regeneration.

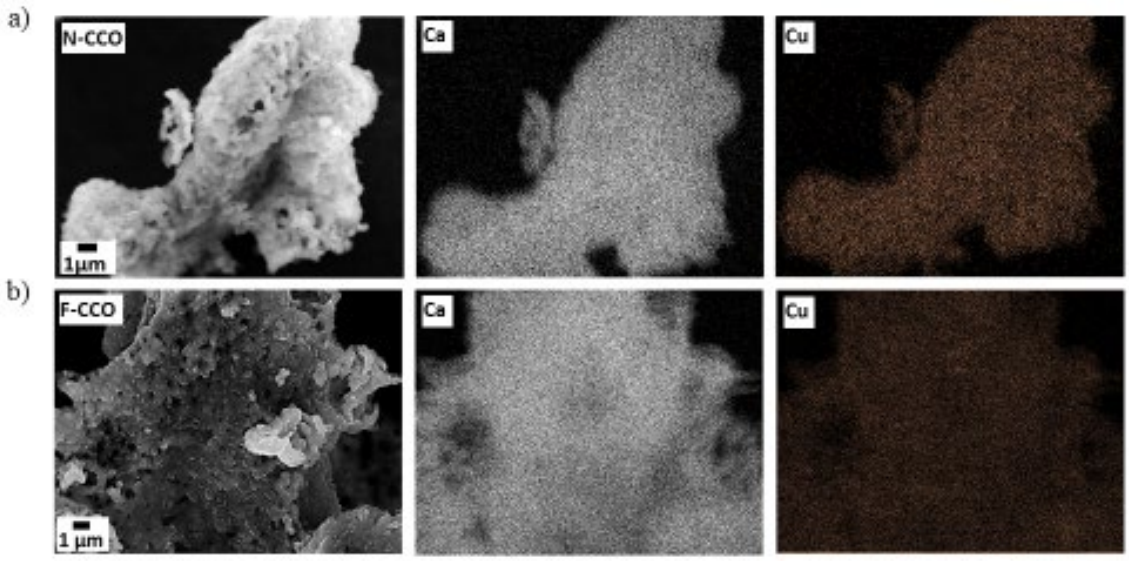

Figure 4.2. Uniform distribution of Ca and Cu. Energy-dispersive X-ray spectroscopy (EDS) of a) N-CCO b) F-CCO.

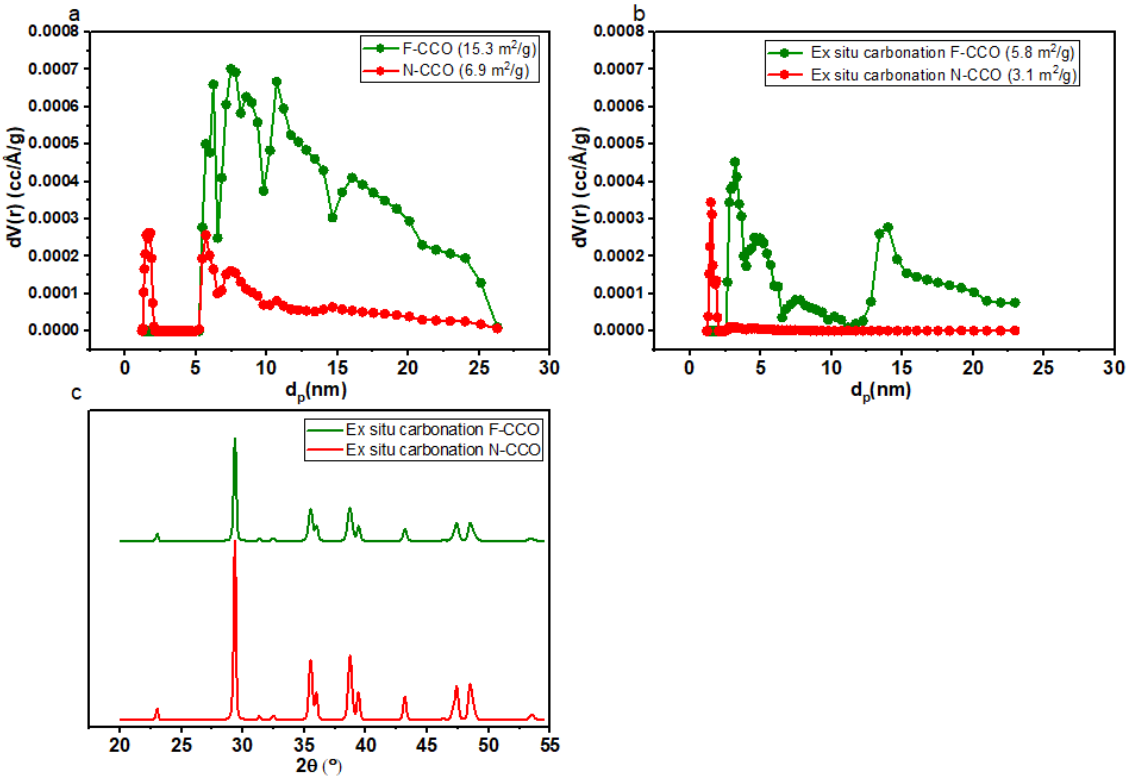

Figure 4.3a depicts the pore size distribution of N-CCO and F-CCO before any carbonation. The pore size below 5 nm was observed only for N-CCO. F-CCO showed larger pore population bigger that 5 nm. This can be beneficial for the carbonation reaction since the CO_2 can diffuse in the gas phase to the sorbent surface more easily [88]. The BET surface area of F-CCO and N-CCO were calculated 15.3 m^2/g and 6.9 m^2/g from nitrogen physisorption. Larger surface area provides better contact between gas (CO_2) and solid sorbent and facilitate the reaction [88].

The physisorption analysis of the sorbents after carbonation show a significant decrease in surface area and pore size for both sorbents (**Figure 4.3b**). The population of pores larger than 3 nm was eliminated for N-CCO. For F-CCO, although the absolute pore volume decreased, we still have surviving pores that are larger than 5 nm. This should be beneficial for easy regeneration facilitating the release of CO_2 from the sorbent. The reduction in surface area and pore size can be

related to formation of $CaCO_3$, consequently sintering, due to a long time exposure of sorbents with CO_2 at high temperature.

After 12 h of carbonation, we took X-ray of the sorbents **Figure 4.3c**. Complete carbonation of both sorbents was confirmed. We did not observe any calcium-containing phase other than $CaCO_3$, and all the copper-containing phases were converted to CuO. The sharper diffraction peaks of N-CCO after long carbonation show a larger crystal size for this sorbent. The smaller crystal size of F-CCO should be attributable to the dispersed copper particles in F-CCO that provided sintering resistance.

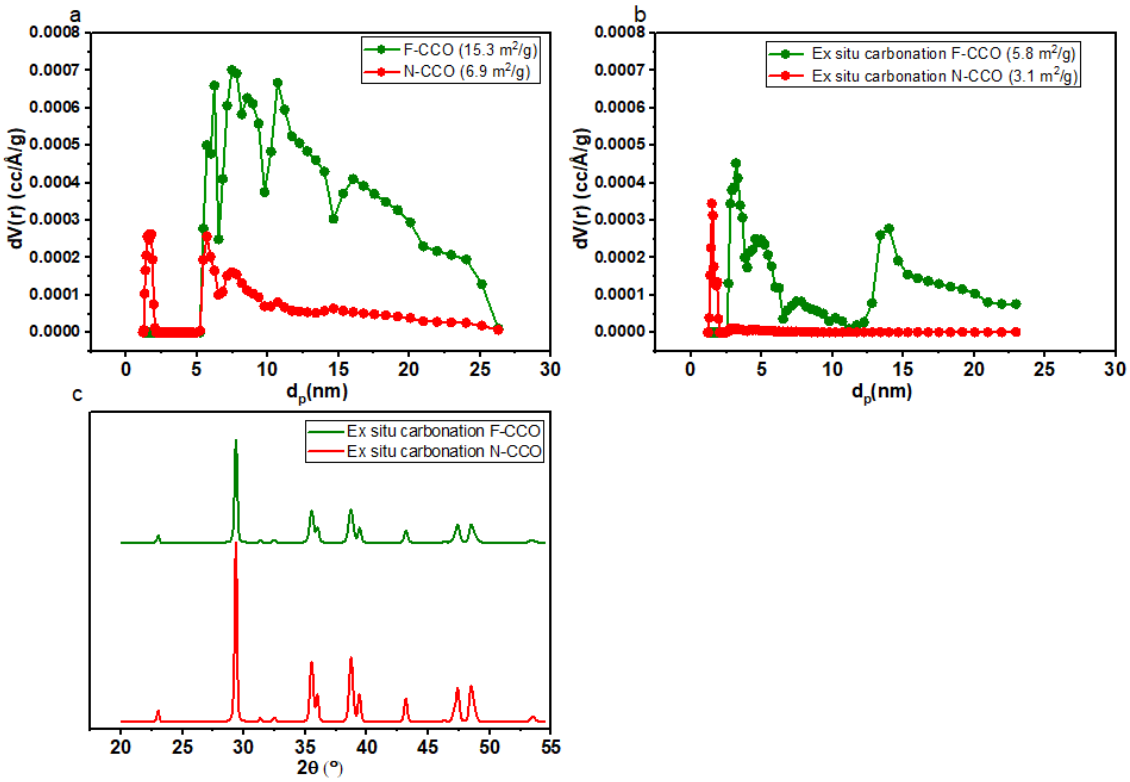

Figure 4.3. Characterization of sorbents. a) Pore size distribution of N-CCO and F-CCO before any carbonation. b) Pore size distribution after ex-situ carbonation of N-CCO and F-CCO under pure CO_2 for 12 h at 800 °C. c) X-ray diffraction patterns of ex-situ carbonated N-CCO and F-CCO.

4.3.2 Temperature-resolved carbonation and regeneration

4.3.2.1 Carbonation behavior of N-CCO and F-CCO

Figure 4.4 shows the carbonation behavior of the sorbents under pure CO_2. A minuscule peak around 29° (2θ) emerged at 500 °C for N-CCO (**Figure 4.4a**). This peak is the most intensive characteristic peak for $CaCO_3$. The results show that the amount of carbonation below 600 °C was

negligible for N-CCO. The conversion of this sorbent reached 10%, 39%, and 81% at 600, 700, and 800 °C respectively. During the operation, we did not detect any CaO in the sorbent, but CuO characteristic peak showed up in the XRD. This implies that CaO was an intermediate phase which quickly reacted with CO_2 to form carbonate. There was no copper-containing carbonate phase which showed the reaction between CuO and CO_2 was not possible within the experimental conditions. The composition of the sorbent at different temperatures can be seen in **Figure 4.5**. The final carbonation products from N-CCO sorbent were $CaCO_3$, Ca_2CuO_3, CuO, and a small amount of Cu.

The carbonation of F-CCO started with CaO and Cu phase. We did not see any composition change at 300 °C (**Figure 4.4b**). When the temperature reached to 400 °C, a low amount of carbonation was detected after 39 min (including 13 min of scan). As the temperature increased, the characteristic peak of $CaCO_3$ became more intensive while CaO got weaker. During experiment Cu content did not react with CO_2. At the end of the experiment at 800 °C, F-CCO turned into 3 phases including, Cu, $CaCO_3$ and a small amount of CaO. The sorbent conversion reached to 83%.

The amount of carbonation was higher for F-CCO compared to N-CCO at the same temperature (**Figure 4.4c**). Comparing the carbonation behavior of F-CCO with N-CCO reveals that the carbonation process can start at lower temperature for F-CCO, which shows the higher reactivity for CO_2 capture. Above 80% of sorbent conversion was achieved for both sorbents under pure CO_2 at 800 °C.

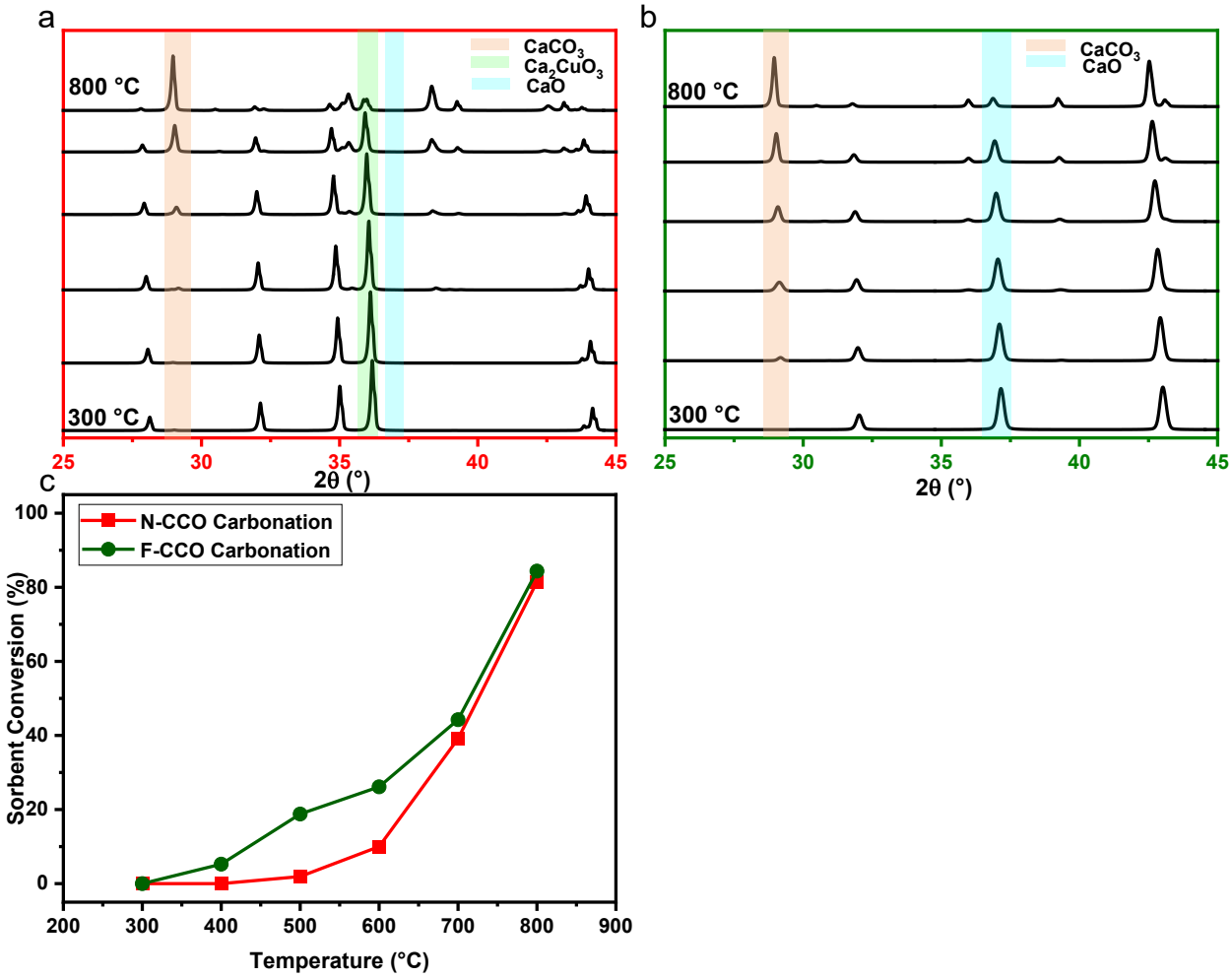

Figure 4.4. Carbonation behavior of the N-CCO and F-CCO under pure CO_2 from 300 °C (bottom scan) to 800 °C (top scan) with a 100 °C interval. a) N-CCO and b) F-CCO. c) Sorbent conversion with respect to temperature. Scanning after 26 min dwell. 13 min scan duration. Heating rate: 10 °C/min.

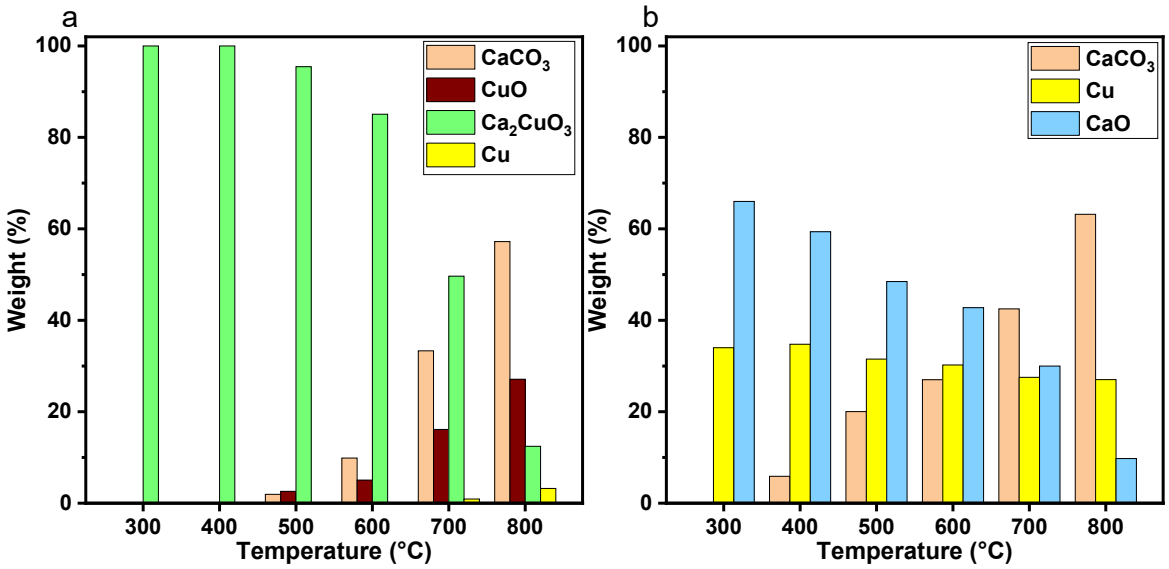

Figure 4.5. The composition of the sorbents under a carbonation condition as the temperature rises. a) N-CCO and b) F-CCO.

4.3.2.2 Regeneration behavior of the carbonated N-CCO and F-CCO

After cooling down the samples under pure CO_2, the sorbent regeneration behavior was investigated. For the carbonated N-CCO, air was used to proceed the regeneration reaction. The dwelling time and X-ray scan time stayed the same as the temperature-resolved carbonation. The air flow rate was 100 sccm during the whole regeneration process. From XRD scans in **Figure 4.6a**, one can observe that there was no change in material composition below 600 °C. The regeneration rate of the carbonated N-CCO was negligible at the low temperatures. At 600 °C, the CaO peak started to emerge, and the amount of $CaCO_3$ started to decrease. At 700 °C, the $CaCO_3$ disappeared as the intensity of the CaO peaks increased. The regeneration of CaO got almost completed at this temperature. The composition of sorbents during regeneration is illustrated in

Figure 4.7. At the end of the regeneration experiment, the N-CCO sorbent turned into 3 phases including, CaO, CuO, and Ca_2CuO_3.

The regeneration for the carbonated F-CCO was conducted under 4% H_2 in N_2 (4 sccm H_2, 96 sccm N_2). **Figure 4.6b** summarizes the regeneration behavior of the carbonated F-CCO. Although the regeneration was negligible below 600 °C, most of the $CaCO_3$ already turned into CaO at 600 °C with 85% sorbent recovery (**Figure 4.6c**). We showed that F-CCO can go through regeneration at lower temperature than N-CCO. Going beyond 600 °C, the $CaCO_3$ peaks disappeared at 700 °C completing the regeneration process. At the end of F-CCO sorbent regeneration, we had two phases of CaO and Cu.

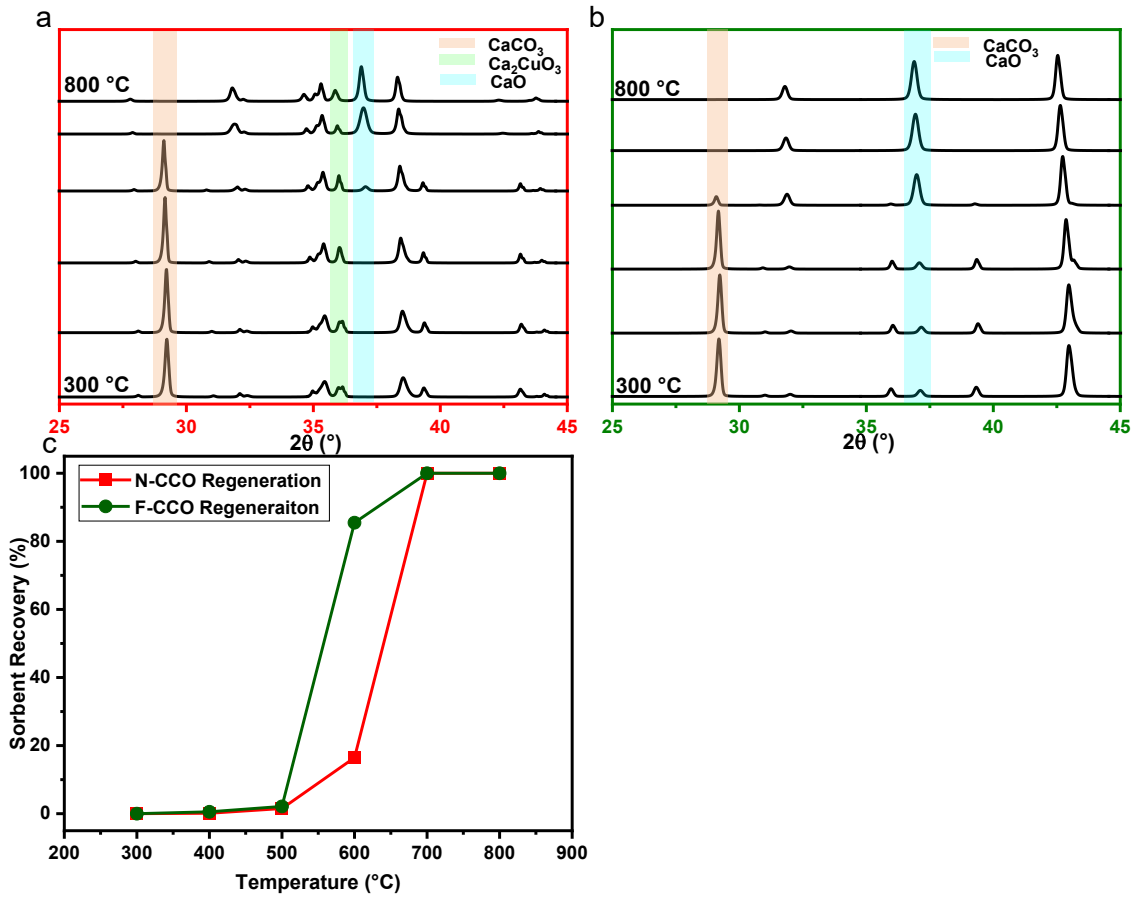

Figure 4.6. Regeneration behavior of the carbonated N-CCO and carbonated F-CCO from 300 °C (bottom scan) to 800 °C (top scan) with a 100 °C interval. a) N-CCO under pure air. b) F-CCO under 4% H_2 in N_2. c) Sorbent recovery with respect to temperature. Scanning after 26 min dwell. 13 min scan duration. Heating rate: 10 °C/min.

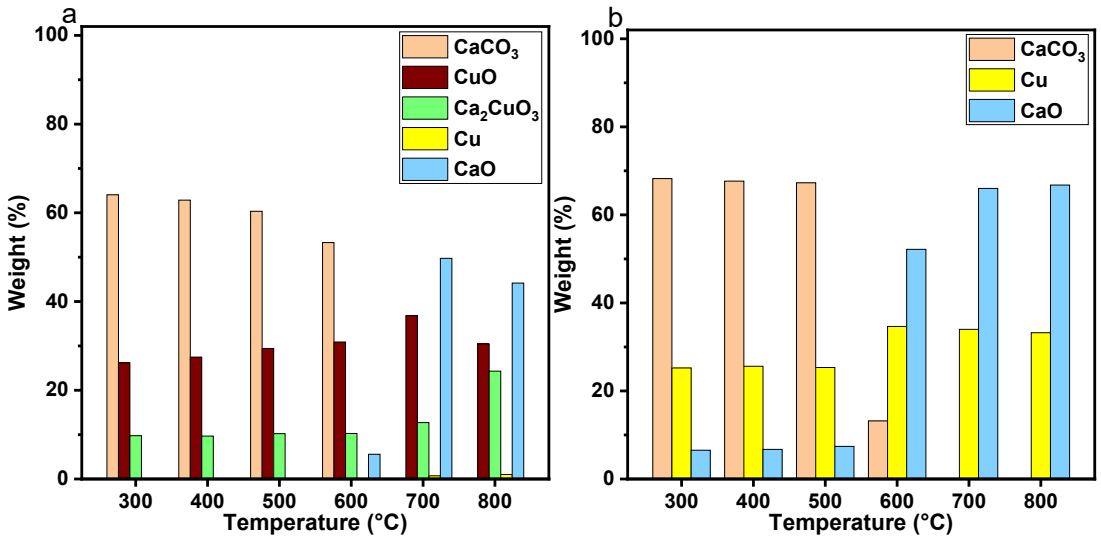

Figure 4.7. The composition of the sorbents under a regeneration condition as the temperature rises. a) N-CCO and b) F-CCO.

4.3.3 Time-resolved carbonation and regeneration

4.3.3.1 Isothermal carbonation kinetics

Figure 4.8 shows the carbonation behavior of the sorbents at 800 °C under pure CO_2 with respect to time. In the first X-ray diffraction patterns, we were not able to see the strongest $CaCO_3$ peak for any of the sorbents. This is because the reactor needs time for the gas transition to CO_2. At high temperatures such as 800 °C, the reaction environment needs to reach a high enough concentration of CO_2 to have the carbonation reaction start. The strongest diffraction peak position of $CaCO_3$ is around 29° (2θ). Considering the scan rate (~2.62°/min), it took less than 3.5 min for the scan to reach this diffraction angle. This limited time prevented us from detecting calcium carbonate diffraction peaks at low angles. Although the main peak at 29° is missing in the first scan, other diffraction peaks of $CaCO_3$ did appear in the high angle region of the first diffraction pattern. Rietveld refinement was performed to estimate the amount of carbonation at the end of

each scan. For the first scan, since the main peak of $CaCO_3$ was missing, we selected the 2θ angle window of 30 to 54° for phase quantification. **Figure 4.8d** summarized the amount of carbonation for the sorbents after each scan. The weight fractions of phases after each scan are shown in **Figure 4.9**.

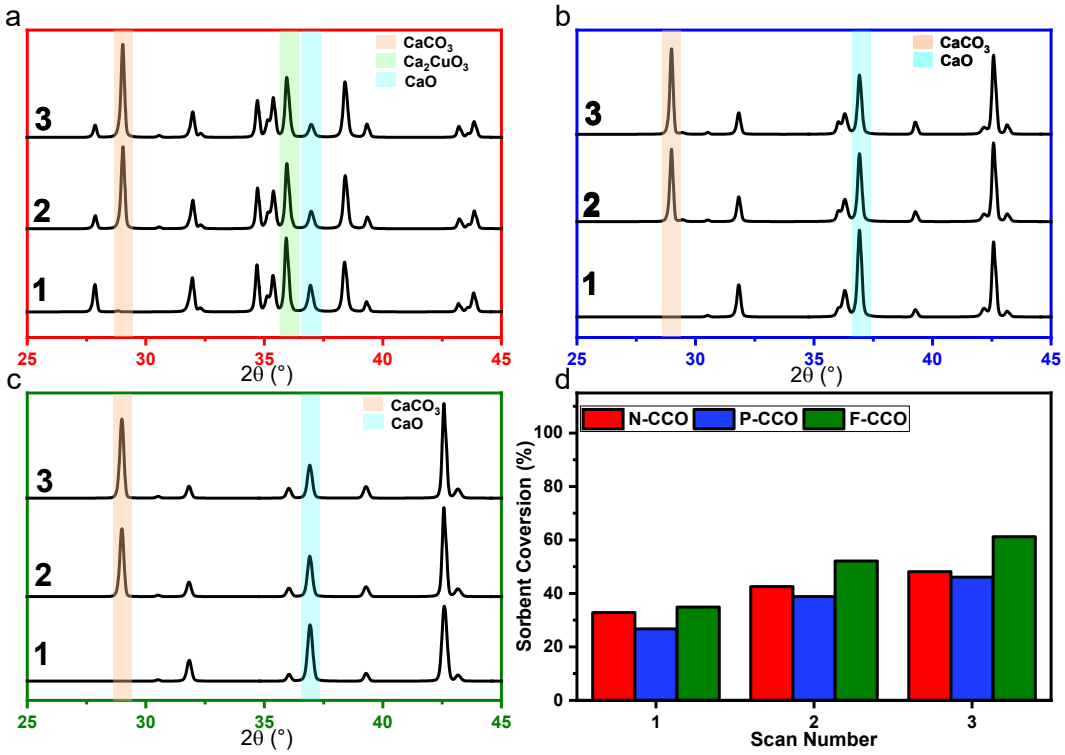

Figure 4.8. The carbonation kinetics of the sorbents under pure CO_2 at 800 °C. a) N-CCO, b) P-CCO, c) F-CCO, and d) Sorbent conversion after each scan (scan duration: 13 min).

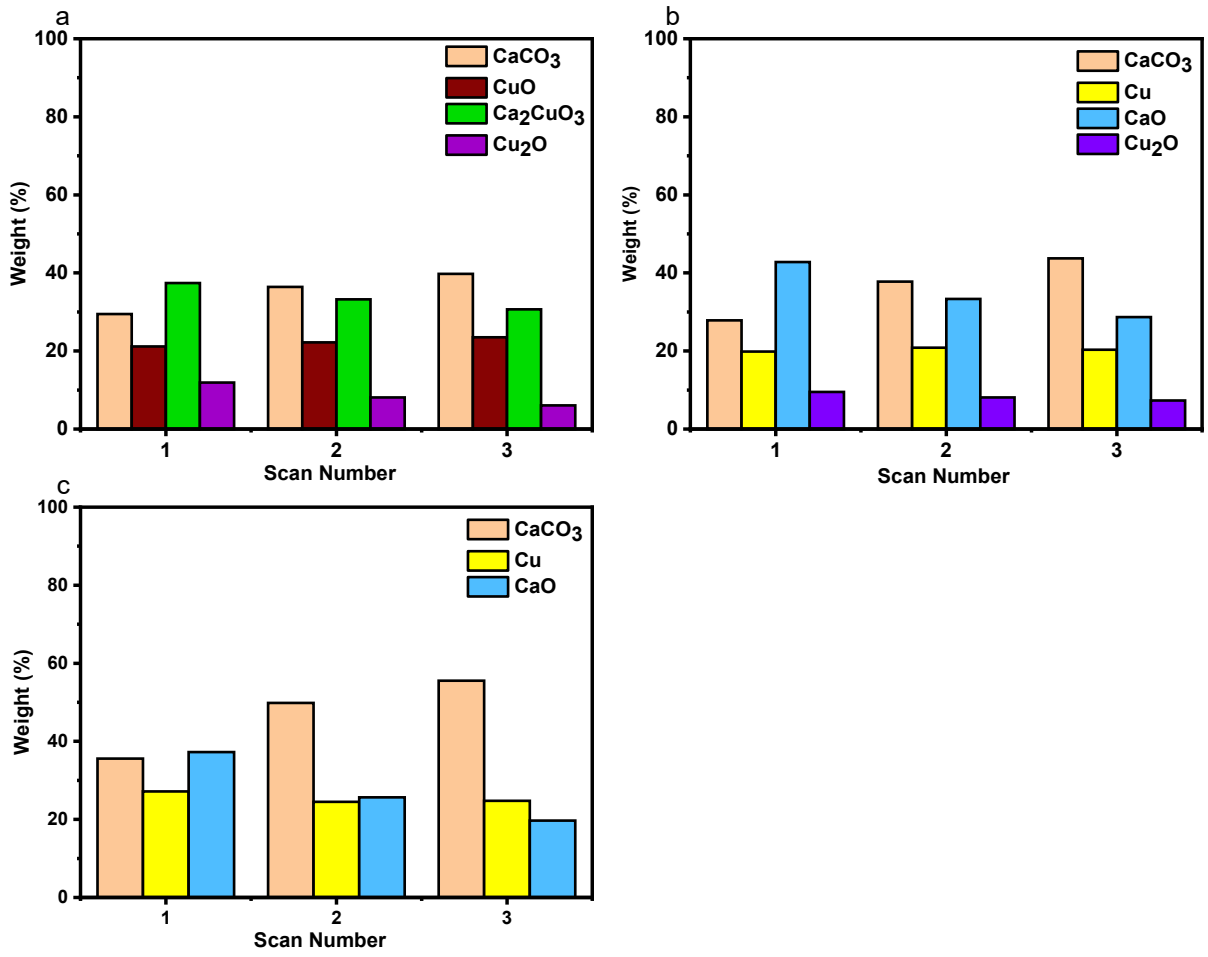

Figure 4.9. The composition of the sorbents during isothermal carbonation at the end of scans. a) N-CCO, b) P-CCO, and c) F-CCO. The carbonation temperature was 800 °C.

4.3.3.2 Isothermal regeneration kinetics

After the third X-ray scan of carbonation, the gas was changed into the regeneration gases. Three consecutive X-ray scans were taken without any time delay (**Figure 4.10**). The strongest peak of $CaCO_3$ at 29° was disappeared during first scan for carbonated F-CCO figure (**Figure 4.10c**). This suggests that the complete regeneration can be done within less than 3.5 min for F-CCO. P-CCO regeneration was also faster than N-CCO. In the first scan, the sorbent recovery of

P-CCO was almost 2.5 times higher than that of N-CCO. In the second scan sorbent recovery reached 78% for N-CCO and 95% for P-CCO. For all samples, calcium carbonate phases vanished in the third scans. At the end of isothermal regeneration, sorbent composition varied based on the thermal history. The regenerated F-CCO had two phases: CaO and Cu. P-CCO had one more phase, Cu_2O. The final composition of N-CCO was CaO, Ca_2CuO_3, CuO, and very small amount of Cu (**Figure 4.11**). N-CCO was the only sorbent that kept original Ca_2CuO_3 phase throughout the whole isothermal carbonation and regeneration processes.

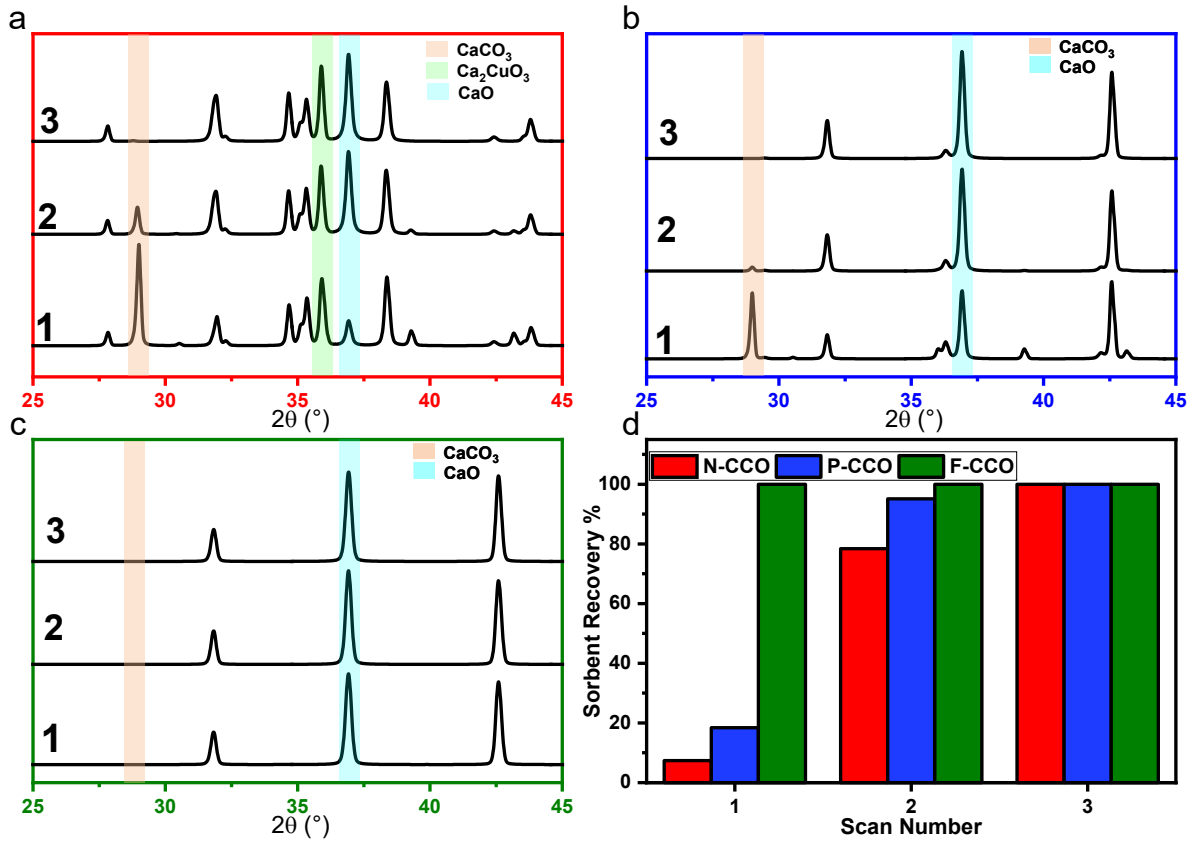

Figure 4.10. The regeneration kinetics of the sorbents under pure air (for N-CCO) and 4% H_2 (for P-CCO and F-CCO) at 800 °C. a) N-CCO, b) P-CCO, c) F-CCO, and d) Sorbent recovery after each scan (scan duration: 13 min).

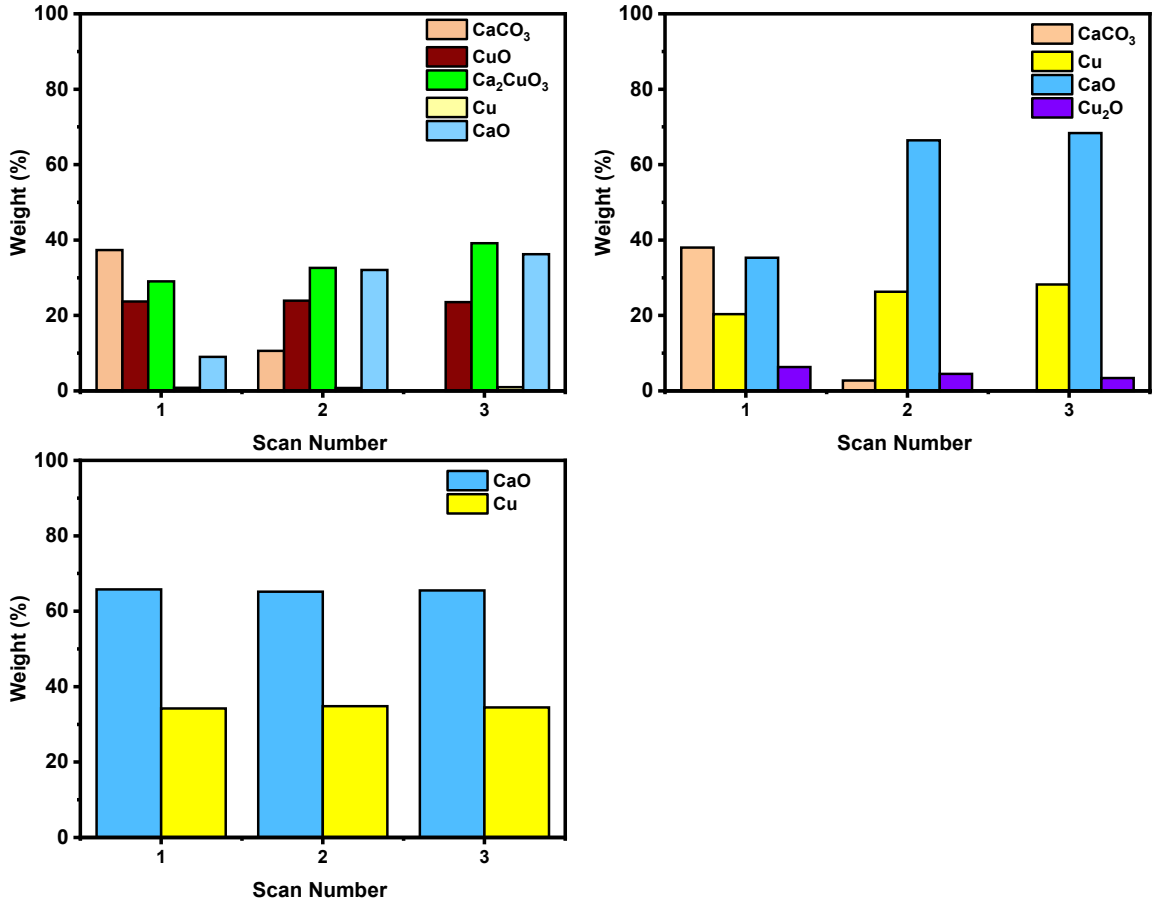

Figure 4.11. The composition of the sorbents during isothermal regeneration at the end of scans. a) N-CCO, b) P-CCO, and c) F-CCO. The decarbonation temperature was 800 °C.

4.3.4 Stability of the sorbents

Figure 4.12a shows the stability of the sorbents through 10 cycles of carbonation-regeneration when the regeneration gas was pure air. A common decrease in performance were observed for both CaO and N-CCO. This decline is caused by the sintering of CaO [94, 162, 166]. The CO_2 conversions at the end of the first cycle were around 59% (CaO) and 49% (N-CCO).

These conversions decreased to 37% (CaO) and 34% (N-CCO) for the 10th cycle. Although the initial sorbent conversion was higher for CaO, the sorbent conversion eventually degraded to the level of N-CCO conversion within 10 cycles. N-CCO consistently showed four phases of CaO, $CaCO_3$, CuO, and Ca_2CuO_3 after each carbonation step (**Figure 4.13**). The residual Ca_2CuO_3 agrees with the low overall CO_2 conversion for this sorbent. The amount of this residual Ca_2CuO_3 gradually increased as the cycling continued. This trend shows that a portion of CaO formed Ca_2CuO_3 again during the sorbent regeneration. The newly formed Ca_2CuO_3 remained inefficient for CO_2 capture in the following cycles.

Figure 4.12b depicts the sorbent stability over 10 cycles with 4% H_2 (in nitrogen) as a regeneration gas. It should be mentioned that the behavior of CaO did not change considerably when we switch the regeneration gases. The average conversion of CaO were 44.7% and 45.5% over 10 cycles when we regenerated the sorbent by pure air and 4% H_2 respectively.

For P-CCO, we observed almost stable behavior over 10 cycles (44.7% $\pm$ 1.5%). In the final several cycles, the P-CCO showed higher sorbent conversion than CaO even though the sorbent conversion in initial cycles were not high. This stable behavior of P-CCO contrasted the well-known performance degradation of CaO. The stable behavior can be related to the existence of copper particles in this sorbent. The in situ generated copper particles provided sintering resistance for the sorbent.

F-CCO had the most efficient performance with average sorbent conversion of 79.2%. In contrast to the usual monotonous degradation of sorbent conversion, we saw sorbent conversion increment. It showed a stable value around 80% from the 3rd cycle on. This increasing, "self-activation", is related to long preheating treatment (12 h) of this sorbent under 4% of H_2 at 800 °C before any carbonation. Manovic et al. explained the similar sorbent behavior in CaO by a pore-

skeleton model [167]. Preheating treatment forms a hard skeleton in the sorbent. This causes slower rate of carbonation for initial cycles.

Figure 4.13 shows the composition evolution for each sorbent as cycling continues. The reported compositions were analyzed after carbonation steps. P-CCO contained CaO, $CaCO_3$, Cu_2O, and Cu while F-CCO did not show any Cu_2O. The weight fraction of Cu is very similar for both P-CCO and F-CCO; however, the copper particle size will be different for these two cases since F-CCO had longer reduction time. The results suggest that the particle size of the sintering barrier material has a significant impact on the sorbent performance. Using Scherrer equation, the CaO crystal sizes in the sorbents were calculated before first and last carbonation (**Table 4.3**). We found that the crystal sizes of CaO and N-CCO increased by 37.5 % and 18.4% while the crystal size of F-CCO ad P-CCO showed little change. CuO particles in N-CCO had limited sintering prevention effect while copper particles in P-CCO and F-CCO were very effective in suppressing sorbent sintering. This is interesting since the melting point of copper is even lower than that of $CaCO_3$. A conventional strategy is to incorporate oxides of high melting point such as ZrO_2 and Al_2O_3. We propose the following explanation. The significant sintering in CaO-based sorbent is related to the easy agglomeration of $CaCO_3$ particles during carbonation. Therefore, it would be critical to remove exothermic heat of the carbonation reaction from the active reaction sites to prevent excessive growth of emerging $CaCO_3$ grains. The presence of copper, a metal with very high thermal conductivity, should facilitate the dissipation of the exothermic heat from the reaction sites. This enhanced heat removal may be the mechanism behind the copper-mediated effective sintering prevention.

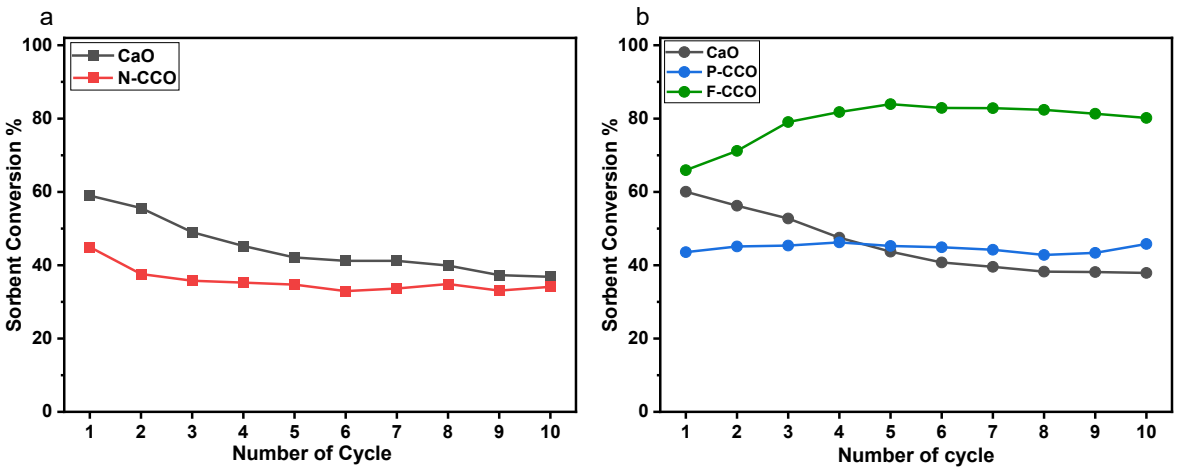

Figure 4.12. Stability analysis for the Ca_2CuO_3 series compared to CaO at 800 °C during 780 min (78 min for each cycle). Each point represents the end of carbonation after complete regeneration. a) Sorbent conversion trend when regenerated by air (CaO and N-CCO). b) Sorbent conversion trend when regenerated by 4% H_2 in N_2 (CaO, P-CCO and N-CCO).

Table 4.2. Thermal properties of relevant materials.

Material	Melting point (°C) [161]	Thermal conductivity (W/m K)
Cu	1085	400 [160]
Cu_2O	1244	4.5 [168]
CuO	1227	18 [160]
CaO	2613	19.5 [169]
$CaCO_3$	1339 [156]	4.5 [170]

Table 4.3. Crystal size of CaO phase in the sorbents within $\pm 2\ nm$ error.

	Crystal size (nm)	
Sorbent	Before first carbonation	Before last carbonation
CaO	32	44
N-CCO	38	45
P-CCO	40	41
F-CCO	28	29

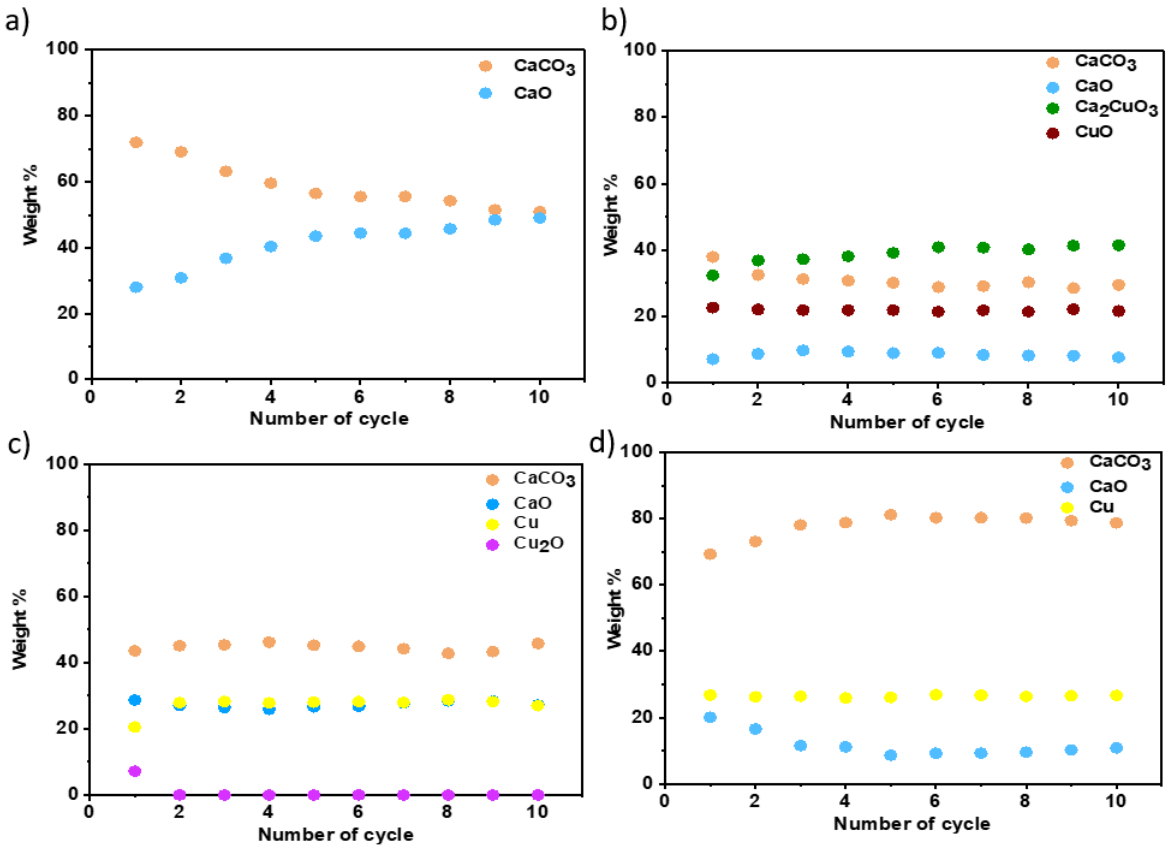

Figure 4.13. Weight percentage of phases at the end of carbonation as the number of cycles increased. a) CaO, b) N-CCO, c) P-CCO, and d) F-CCO.

4.4 Conclusion

To compare their carbonation and regeneration behaviors, four different sorbents, CaO, N-CCO, P-CCO, and F-CCO, were successfully synthesized. Ca_2CuO_3 (N-CCO) was reduced under 4% H_2 to fabricate two different variants. When Ca_2CuO_3 is completely decomposed (F-CCO), only CaO and Cu phases survived, while Cu_2O was also present in addition to CaO and Cu for the partially decomposed case (P-CCO). After complete decomposition, F-CCO had a larger surface area and pore size than N-CCO. The phase quantification was based on Rietveld refinement to evaluate the sorbent conversion and recovery. We observed complete carbonation of both F-CCO

and N-CCO when carbonation was conducted under pure CO_2 for 12 h at 800 °C. F-CCO had a smaller $CaCO_3$ crystal size than N-CCO at the end of carbonation. The initial copper content in the F-CCO may be the reason since the high thermal conductivity of copper supports facile heat removal from the carbonation reaction front. In the temperature-resolved experiments, F-CCO showed higher conversion throughout the whole temperature range with a lower carbonation onset temperature than N-CCO.

Temperature below 500 °C was ineffective in regenerating any of the tested sorbents. However, at 600 °C, high recovery was attained for F-CCO (more than 80%), surpassing the low N-CCO sorbent recovery (less than 20%). Therefore, the F-CCO sorbent has the potential to make the post-combustion carbon capture process energy-efficient.

The isothermal carbonation and regeneration test at 800 °C showed that F-CCO had faster kinetics than the other sorbents. The great regeneration rate resulted in the complete sorbent recovery in less than 3.5 min. A sorbent with rapid regeneration is desirable due to process cost reduction in time and energy. F-CCO also showed self-activation during the cycling stability test. Averaged sorbent conversion of this sorbent was outstanding, delivering at least 33% higher value than other sorbents. The excellent stability of this sorbent may be related to finely-dispersed copper particles within the CaO matrix. Even though copper particles have a low melting point, the high thermal conductivity of the copper particles efficiently deters sorbent sintering. We confirmed that the CaO crystal size does not increase when we have in situ generated copper particles dispersed in P-CCO and F-CCO.

In conclusion, F-CCO showed favorable post-combustion CO_2 capture performance regarding capacity, kinetics, and cycle stability under the conditions where in situ generated copper particles are preserved.

Chapter 5 Conclusion and future work

In this dissertation, mechanical and chemical activation of CaO-based sorbents were investigated. In the first chapter, a literature review was done to understand the challenges facing the Calcium Looping technology. As discussed, one of the main challenges in this process is the decay behavior of CaO for long-term use due to the sintering. Here, we tried to address the issue by activation of the sorbent through the mechanical and chemical processes. In chapter 2, we investigated the effect of morphology change by ball milling on carbonation, regeneration, and cycle stability. We found low-speed ball milling is not effective for the process. There was no significant change observed when we used 100 rpm in carbonation conversion and regeneration rate. The sorbent showed a promising performance when 500 rpm was applied. The increase in surface area and pore size, and decrease in particle size and crystal size of the sorbent were correlated to higher conversion and regeneration rate of the sorbent. After 10 cycles, the regeneration rate decreased significantly when the commercial $Ca(OH)_2$ was used, while the CH500 showed a decent regeneration rate. The average conversion of 68.2% was achieved when CH500 was used. This amount was 55.2 % for the commercial $Ca(OH)_2$. Although the mechanical activation was effective, the typical decay in the performance of the sorbent was observed. Therefore, more investigations were done by chemical activation of CaO-based sorbents.

In chapter 3, we synthesized three different calcium-based ternary oxides to evaluate their performance for CO_2 capture. It was found that $Ca_2Fe_2O_5$ and $Ca_3Co_4O_9$ had a low CO_2 adsorption capacity. Ca_2CuO_3 showed a high capacity for CO_2 adsorption. During cycle stability, this sorbent did not only show a decent retention capacity but also a narrower range of operational temperature

while a higher cycle-averaged decarbonation rate. The satisfactory performance of Ca_2CuO_3leads us to conduct more investigation on this sorbent.

In chapter 4, we focused on the effect of the solid-state decomposition of Ca_2CuO_3 on the performance of the sorbent for CO_2 capture at high temperatures. The high stability was observed for Ca_2CuO_3 while the complete decomposition was performed on the sorbent. We also observed a self-activation for F-CCO. This means unlike the typical decay of CaO performance through cycling, an increase in the performance was observed initially and stabled for the next cycles. The presence of Cu, a material with high thermal conductivity, in the sorbent was the main reason for the efficient performance of F-CCO. Lower carbonation temperatures were observed for F-CCO sorbent. F-CCO also showed rapid regeneration kinetics, which makes this sorbent suitable for Calcium Looping process.

Despite the improvement in sorbent behavior in this work, synthesizing an engineering sorbent to maximize its capacity and stability remains challenging. Therefore the following directions are recommended for future works.

5.1 Synthesizing nanofiber sorbents

One of the main goals in synthesizing CaO-based sorbents is to increase surface area and pore size to provide better contact between CO_2 and the sorbent, and decrease the diffusion limitation of CO_2 in the CaO pores. One of the method that we propose is the electrospinning technique which can be an excellent choice in this regard. The size of fiber which is related to the final size of particle, can be controlled by the viscosity of the solution, the distance (between the syringe needle and collector plate), the voltage of the electric field and the needle size. Taking

these parameters into account, we can synthesize CaO-based sorbents with high surface area and pore size.

In order to see the effectiveness of this method, we evaluated the performance of Ca_2CuO_3 nanofiber. The temperature swing carbonation/decarboation was conducted between 740-850 °C (this is the optimum temperatures that we found in the 3rd chapter) under 20% CO_2. .we heated the sorbents to T_c under pure N_2, then we changed the gas to 20% CO_2 (in N_2). The reactor temperature was further raised to T_d. We repeated this T_c-T_d temperature cycling with 10 °C/min heating and cooling rates to have 22 carbonation periods and 21 decarbonation periods in total while we kept the inlet CO_2 20 percent constant. The results of the experiment can be seen in **Figure 5.1**. The sharper peaks in **Figure 5.1b** (compared to **Figure 5.1**a) indicate higher carbonation and regeneration rate of Ca_2CuO_3 nanofiber (compared to the powder one). We calculated the total amount of carbonation in the process by integrating the area under the curve of each carbonation stage and sum up all together. We also calculated the average carbonation and decarbonation rate of each sorbent. The results are summarized in **Table 5.1**.

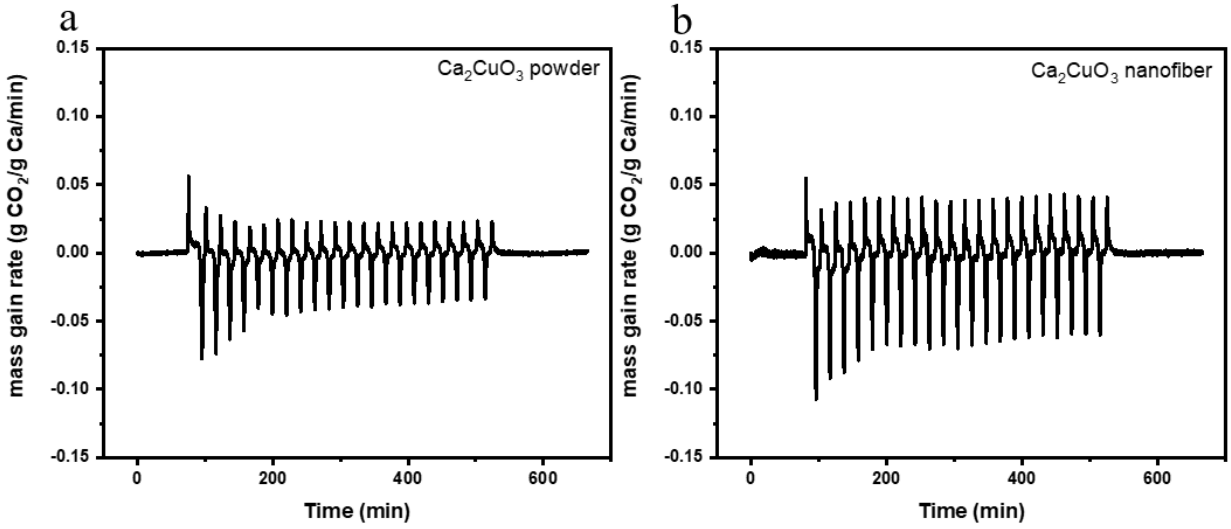

Figure 5.1. Temperature swing carbonation/decarbonation kinetics comparison under 20% CO_2. a) Ca_2CuO_3 powder change rate. b) Ca_2CuO_3 nanofiber mass change rate. The experiments were done between Tc (740 °C) and Td (850 °C) of each sorbent.

Table 5.1. The performance comparison of Ca_2CuO_3 powder and Ca_2CuO_3 nanofiber under 20% of CO_2 in temperature swing carbonation/ decarbonation experiment.

Sorbent	Ca_2CuO_3 Powder	Ca_2CuO_3 nanofiber
Carbonation (g CO_2/ g Ca)	2.485	3.490
Average carbonation rate (g CO_2/g Ca/min)	0.011	0.016
Average regeneration rate (g CO_2/g Ca/min)	0.009	0.013

The performance of Ca_2CuO_3 nanofiber increased by 40%, 45%, and 44% in carbonation amount, average carbonation rate, and average regeneration rate compared to Ca_2CuO_3 Powder. This increase can be related to the high surface and pore size of this sorbent, as can be seen in **Figure 5.2**. The surface area of Ca_2CuO_3 nanofiber is almost 3 times of Ca_2CuO_3 nanofiber.

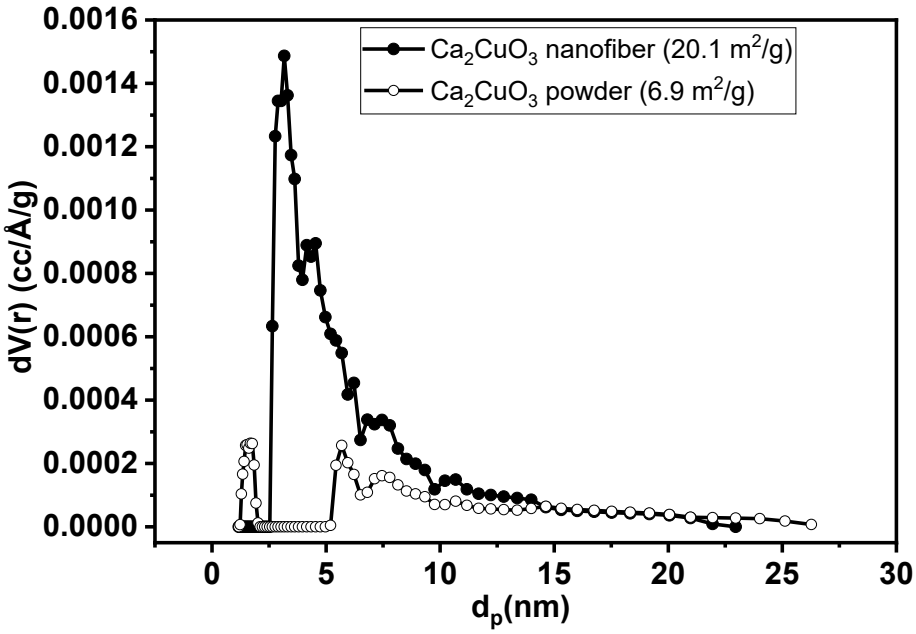

Figure 5.2. Surface area and pore size distribution of fresh Ca_2CuO_3 Powder and Ca_2CuO_3 nanofiber.

The fiber structure of this sorbent was also confirmed by Scanning Electron Microscope (**Figure 5.3**).

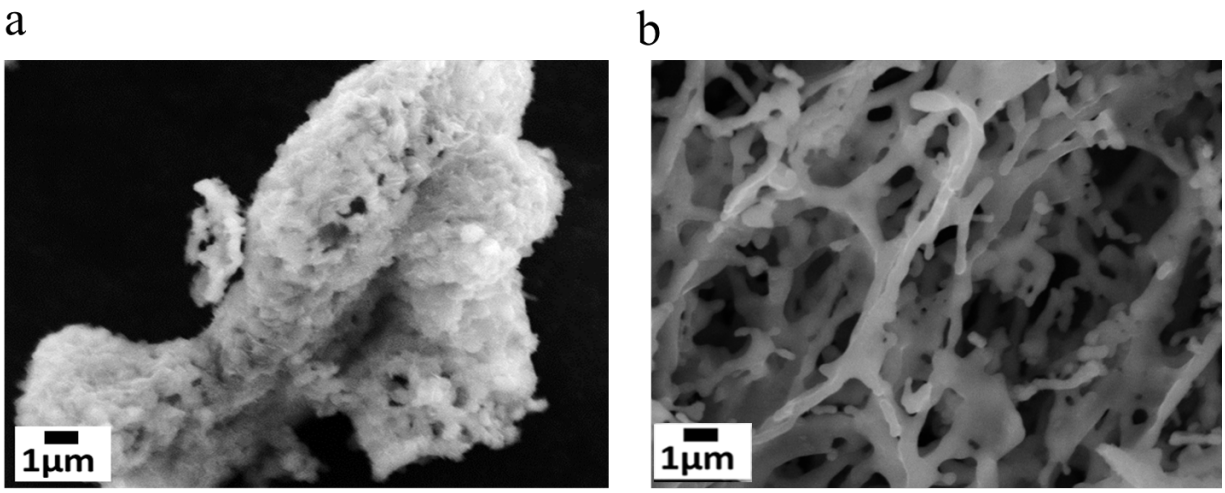

Figure 5.3. SEM Images of fresh Ca_2CuO_3 Powder and Ca_2CuO_3 nanofiber.

The preliminary results showed synthesizing Ca_2CuO_3 nanofiber using the electrospinning technique can improve the performance of the sorbent for CO_2 capture in the Calcium Looping process.

The nanofiber sorbent was synthesized with the specific condition as follow. 2.5 g Polyvinylpyrrolidone (PVP) was dissolved in 10g Dimethylformamide (DMF). Stoichiometry amount of calcium nitrate tetrahydrate (BeanTown Chemical, 99%) and copper (II) acetate monohydrate (Sigma-Aldrich, ACS Reagent, ≥98%) were added to the solution. The solution was stirred overnight and then loaded into the syringe. The electrospinning was done under specific conditions illustrated in **Figure 5.4**. The collected fiber sheet was calcined at 900 °C to produce a single phase Ca_2CuO_3.

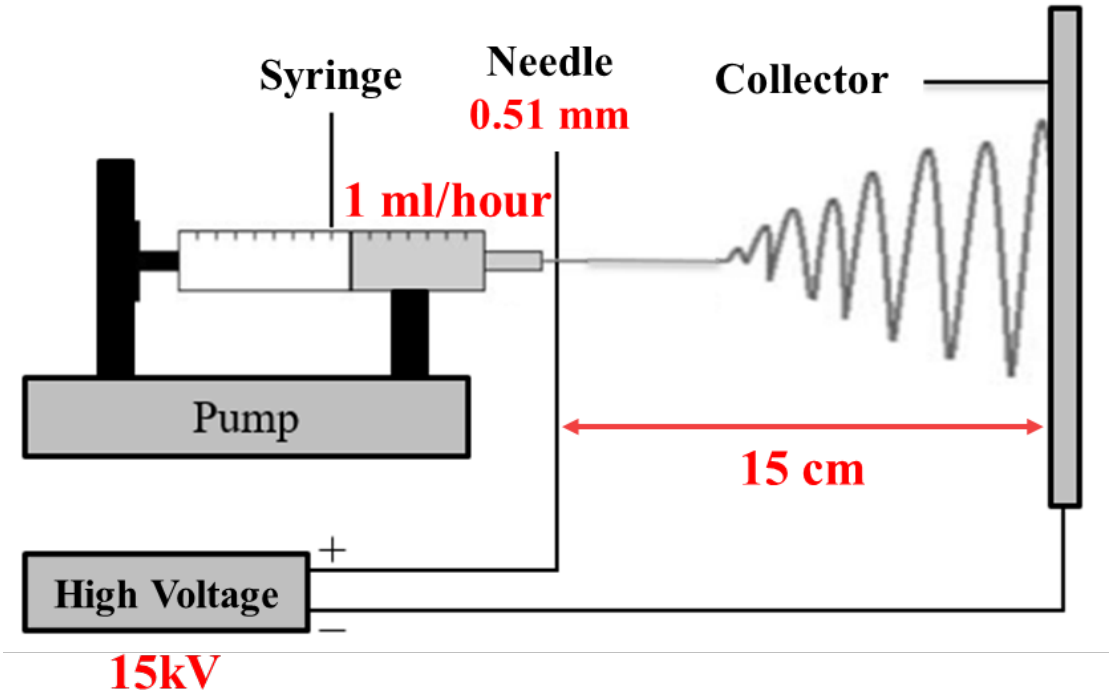

Figure 5.4. Electrospinning condition for synthesizing Ca_2CuO_3 nanofiber.

As mention, by controlling variables in electrospinning, one can synthesize the nanofiber with desirable thickness to produce high surface area sorbents to increase the capacity of CO_2 capture in Calcium Looping process.

5.2 Synthesizing composite sorbents with high melting point and thermal conductivity

We found generating in situ copper into CaO can mitigate the sintering due to the high thermal conductivity of Cu. Although Cu has very high thermal conductivity, it has a relatively low melting point (1085 °C). Synthesized an engineered composite with a high melting point and high thermal conductivity by composition variable and introducing it into CaO can improve the performance of sorbent. A higher melting point provides an excellent scaffold for the sorbent and high temperature, while a higher thermal conductivity can enhance a heat transfer between gas and solid phase. As a result, the kinetics of the reaction will boost. Therefore, a shorter time is needed for the regeneration process, which results in sintering mitigation.

MgO (2852 °C), ZrO_2 (2709 °C), La_2O_3 (2410 °C) and CeO (2400 °C) [156] can be the best candidates due to their melting point. Synthesizing a composite of CaO, Cu and these materials (one or more) may provide a sorbent with the satisfied performance considering fast reaction kinetics and stability. It should be mentioned that one of the main challenges is to keep the composition of the sorbent constant. This is because we want to have Cu without oxidation while other composites are metal oxide. This condition may be achieved by controlling the reduction environment and adjusting gas composition (changing the hydrogen concertation in the regeneration stage) or regeneration temperature. A comprehensive thermodynamics study is necessary to achieve this goal.

Another aspect that needs to be investigated is the impact of externally introduce of copper and copper oxide into CaO on carbonation and decarbonation performance. In chapter 4, the copper

was internally generated by Ca_2CuO_3 decomposition. Controlling the composition of the sorbent by introducing a specific amount of copper and/or copper oxide, and its impact on the performance is of great interest.

Controlling the amount of H_2 in the regeneration stage also can be an area of investigation. The goal is to reduce the amount of H_2 since it is a high valuable energy source. However, the declining performance of the sorbent should not be sacrificed. The preliminary result suggests that when we change the regeneration gas into pure N_2 (compared to 4% H_2 in N_2, which was studied in chapter 4), the performance of sorbent decreases (**Figure 5.5**). The average sorbent conversion declined to 66.7% when we used pure N_2 as regeneration gas (it was 79.2 % when 4% H_2 was used).

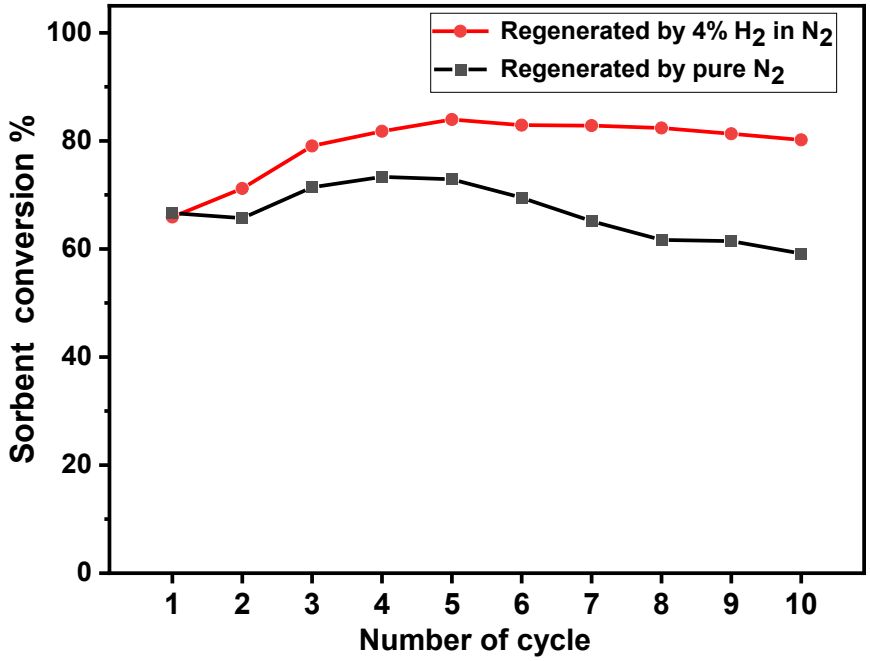

Figure 5.5. Comparison of F-CCO carbonation performance when 4% H_2 and pure N_2 were used as regeneration gas.

5.3 Using CaO based sorbent for carbon capture at low temperatures

Most studies have focused on the CaO-based sorbents application on CO2 capture at high temperatures. A lack of comprehensive research on using CaO based sorbent at low temperature for carbon capture should get the scientists' attention. Based on the effectiveness of ball milling, this can be done by changing the microstructure of CaO-based sorbent. Regarding this, we designed an experiment to investigate the performance of CaO-based sorbent for CO_2 capture at low temperatures. We put 1.1 g $Ca(OH)_2$ in the 250 ml jar (which was filled by 250 g of 3mm zirconia balls which filled 100 ml of jar size). The jar was filled with pure CO_2 to 34.7 psia. We run the ball milling with 300 rpm and keep track of pressure drop each 30 min. The results of the experiment can be seen in **Table 5.2** and **Figure 5.6**. The conversion of CO_2 was calculated as follow,

$$CO_2\ coversion\ \% = \frac{P_{CO_{2_i}} - P_{CO_2}}{P_{CO_{2_i}}} \times 100 \qquad (5-1)$$

where $P_{CO_{2_i}}$ initial CO_2 pressure, and P_{CO_2} is final CO_2 pressure with respect to time.

Table 5.2. CO_2 pressure and conversion over time under 300 rpm ball milling when $Ca(OH)_2$ was used as the sorbent.

Time (min)	pressure (psia)	CO_2 conversion (%)
0	34.7	0
30	26	25.1
60	18.6	46.4

90	8	76.9
120	5.4	84.4
150	4.7	86.5
180	4	88.5

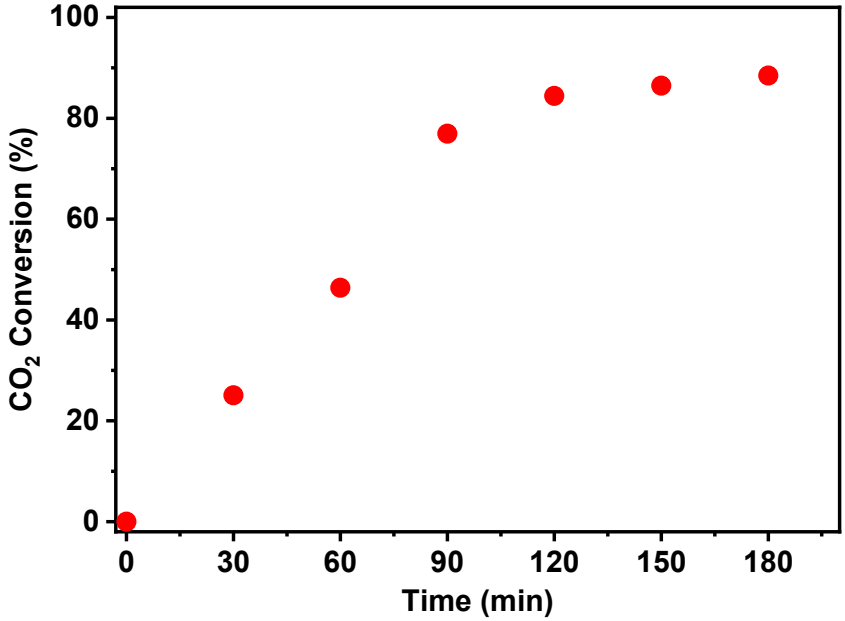

Figure 5.6. CO_2 conversion over time under 300 rpm ball milling when $Ca(OH)_2$ (1.1 g) was used as the sorbent.

After 3 hours of ball milling, the sorbent was collected, and we took the X-ray scan. The Rietveld refinement was performed on the X-ray pattern of the sorbent, and the weight percent of $Ca(OH)_2$ and $CaCO_3$ was calculated. The conversion of sorbent was calculated based on the following equation (MW: molecular weight):

$$\text{Sorbent conversion} = \frac{wt\%CaCO_3}{wt\%Ca(OH)_2\left(\frac{MW_{CaCO_3}}{MW_{Ca(OH)_2}}\right) + wt\%CaCO_3} \times 100 \qquad (4-1)$$

The result indicates a conversion of 91.7%. This result agrees with CO_2 conversion, which was obtained from the pressure drop in the jar due to CO_2 consumption by the sorbent. CO_2 conversion is equal to sorbent conversion according to stoichiometry of the component in the following reaction,

$$Ca(OH)_2\,(s) + CO_2\,(g) \rightarrow CaCO_3\,(s) + H_2O\,(g). \qquad (4-2)$$

In addition to the above experiment, the performance of CaO was investigated and compared with $Ca(OH)_2$. For the sake of fair comparison, 6 g of $Ca(OH)_2$ was equally divided into 3 g. One of the sample was burnt at 900 °C to synthesize CaO, and the other one was used as it is. The same ball milling procedure was done for both sorbents for 2 hours. The result can be seen in **Figure 5.7**. The result indicates that the performance of $Ca(OH)_2$ is better than CaO.

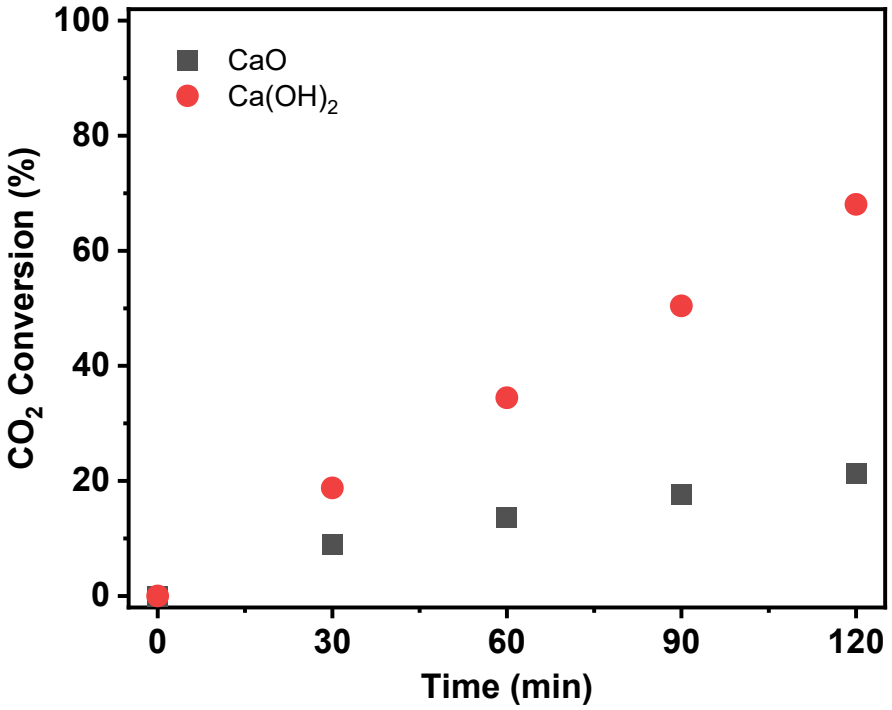

Figure 5.7. Comparison of CO_2 conversion of CaO and $Ca(OH)_2$ (3 g) over time under 300 rpm ball milling.

The result showed that the carbonation of $Ca(OH)_2$ can be effective at low temperatures. The following proposal can be a direction to improve the process of carbonation at low temperatures:

1- The experiment was done at 300 rpm of ball milling. This rotational speed imposes a huge cost on the CO_2 capture process. Lowering the rotational speed is desirable as long as the amount of carbonation is satisfied.

2- The result showed that CaO could not be effective enough to use this sorbent at low temperatures. However, CaO naturally can be covert to $Ca(OH)_2$ in a humid

environment due to its hydrophilicity. Therefore, the effect of humidity on the sorbent conversion needs to be investigated.

References

[1] K.M.K. Yu, I. Curcic, J. Gabriel, S.C.E. Tsang, Recent advances in CO_2 capture and utilization, ChemSusChem: Chemistry & Sustainability Energy & Materials 1 (2008) 893-899.

[2] H.O. Pörtner, D.C. Roberts, H. Adams, C. Adler, P. Aldunce, E. Ali, R.A. Begum, R. Betts, R.B. Kerr, R. Biesbroek, Climate change 2022: impacts, adaptation and vulnerability, (2022).

[3] S.A. Rackley, Carbon capture and storage, Butterworth-Heinemann2017.

[4] Z. Zhang, T.N. Borhani, M.H. El-Naas, Carbon capture, Exergetic, energetic and environmental dimensions, Elsevier2018, pp. 997-1016.

[5] P. Markewitz, W. Kuckshinrichs, W. Leitner, J. Linssen, P. Zapp, R. Bongartz, A. Schreiber, T.E. Müller, Worldwide innovations in the development of carbon capture technologies and the utilization of CO 2, Energy & environmental science 5 (2012) 7281-7305.

[6] A. Al-Mamoori, A. Krishnamurthy, A.A. Rownaghi, F. Rezaei, Carbon capture and utilization update, Energy Technology 5 (2017) 834-849.

[7] M.R. Rahimpour, M. Farsi, M.A. Makarem, Advances in Carbon Capture: Methods, Technologies and Applications, Woodhead Publishing2020.

[8] B. Metz, O. Davidson, H. De Coninck, M. Loos, L. Meyer, IPCC special report on carbon dioxide capture and storage, Cambridge: Cambridge University Press2005.

[9] J. Oexmann, A. Kather, S. Linnenberg, U. Liebenthal, Post-combustion CO_2 capture: chemical absorption processes in coal-fired steam power plants, Greenhouse Gases: Science and Technology 2 (2012) 80-98.

[10] D. Jansen, M. Gazzani, G. Manzolini, E. van Dijk, M. Carbo, Pre-combustion CO_2 capture, International Journal of Greenhouse Gas Control 40 (2015) 167-187.

[11] B. Erlach, M. Schmidt, G. Tsatsaronis, Comparison of carbon capture IGCC with pre-combustion decarbonisation and with chemical-looping combustion, Energy 36 (2011) 3804-3815.

[12] J. Xu, G.F. Froment, Methane steam reforming, methanation and water-gas shift: I. Intrinsic kinetics, AIChE journal 35 (1989) 88-96.

[13] M. Halabi, M. De Croon, J. Van der Schaaf, P. Cobden, J. Schouten, Low temperature catalytic methane steam reforming over ceria–zirconia supported rhodium, Applied Catalysis A: General 389 (2010) 68-79.

[14] C. Higman, Gasification, Combustion engineering issues for solid fuel systems, Elsevier2008, pp. 423-468.

[15] T.L. LeValley, A.R. Richard, M. Fan, The progress in water gas shift and steam reforming hydrogen production technologies–A review, International Journal of Hydrogen Energy 39 (2014) 16983-17000.

[16] J. Yu, F.-J. Tian, L.J. McKenzie, C.-Z. Li, Char-supported nano iron catalyst for water-gas-shift reaction: hydrogen production from coal/biomass gasification, Process Safety and Environmental Protection 84 (2006) 125-130.

[17] D.S. Newsome, The water-gas shift reaction, Catalysis Reviews Science and Engineering 21 (1980) 275-318.

[18] C. Ratnasamy, J.P. Wagner, Water gas shift catalysis, Catalysis Reviews 51 (2009) 325-440.

[19] B.S. RJ, M. Loganathan, M.S. Shantha, A review of the water gas shift reaction kinetics, International Journal of Chemical Reactor Engineering 8 (2010).

[20] C. Wheeler, A. Jhalani, E. Klein, S. Tummala, L. Schmidt, The water–gas-shift reaction at short contact times, Journal of catalysis 223 (2004) 191-199.

[21] B. Dutcher, M. Fan, A.G. Russell, Amine-based CO_2 capture technology development from the beginning of 2013- A Review, ACS applied materials & interfaces 7 (2015) 2137–2148.

[22] M.B. Toftegaard, J. Brix, P.A. Jensen, P. Glarborg, A.D. Jensen, Oxy-fuel combustion of solid fuels, Progress in energy and combustion science 36 (2010) 581-625.

[23] M.A. Nemitallah, M.A. Habib, H.M. Badr, S.A. Said, A. Jamal, R. Ben-Mansour, E.M. Mokheimer, K. Mezghani, Oxy-fuel combustion technology: current status, applications, and trends, International Journal of Energy Research 41 (2017) 1670-1708.

[24] G. Scheffknecht, L. Al-Makhadmeh, U. Schnell, J. Maier, Oxy-fuel coal combustion—A review of the current state-of-the-art, International Journal of Greenhouse Gas Control 5 (2011) S16-S35.

[25] M. Habib, H. Badr, S. Ahmed, R. Ben-Mansour, K. Mezghani, S. Imashuku, G. la O', Y. Shao-Horn, N. Mancini, A. Mitsos, A review of recent developments in carbon capture utilizing oxy-fuel combustion in conventional and ion transport membrane systems, International Journal of Energy Research 35 (2011) 741-764.

[26] S. Yadav, S. Mondal, A review on the progress and prospects of oxy-fuel carbon capture and sequestration (CCS) technology, Fuel 308 (2022) 122057.

[27] B.J. Buhre, L.K. Elliott, C. Sheng, R.P. Gupta, T.F. Wall, Oxy-fuel combustion technology for coal-fired power generation, Progress in energy and combustion science 31 (2005) 283-307.

[28] C. Chao, Y. Deng, R. Dewil, J. Baeyens, X. Fan, Post-combustion carbon capture, Renewable and Sustainable Energy Reviews 138 (2021) 110490.

[29] Y. Wang, L. Zhao, A. Otto, M. Robinius, D. Stolten, A review of post-combustion CO_2 capture technologies from coal-fired power plants, Energy Procedia 114 (2017) 650-665.

[30] M. Kárászová, B. Zach, Z. Petrusová, V. Červenka, M. Bobák, M. Šyc, P. Izák, Post-combustion carbon capture by membrane separation, Review, Separation and purification technology 238 (2020) 116448.

[31] S. Zhao, P.H. Feron, L. Deng, E. Favre, E. Chabanon, S. Yan, J. Hou, V. Chen, H. Qi, Status and progress of membrane contactors in post-combustion carbon capture: A state-of-the-art review of new developments, Journal of Membrane Science 511 (2016) 180-206.

[32] K. Ramasubramanian, W.W. Ho, Recent developments on membranes for post-combustion carbon capture, Current Opinion in Chemical Engineering 1 (2011) 47-54.

[33] G.T. Rochelle, Amine scrubbing for CO_2 capture, Science 325 (2009) 1652-1654.

[34] G. Rochelle, Conventional amine scrubbing for CO_2 capture, Absorption-based post-combustion capture of carbon dioxide, Elsevier2016, pp. 35-67.

[35] J. Blamey, E. Anthony, J. Wang, P. Fennell, The calcium looping cycle for large-scale CO_2 capture, Progress in Energy and Combustion Science 36 (2010) 260-279.

[36] C.C. Dean, J. Blamey, N.H. Florin, M.J. Al-Jeboori, P.S. Fennell, The calcium looping cycle for CO_2 capture from power generation, cement manufacture and hydrogen production, Chemical Engineering Research and Design 89 (2011) 836-855.

[37] H. Dieter, A.R. Bidwe, G. Varela-Duelli, A. Charitos, C. Hawthorne, G. Scheffknecht, Development of the calcium looping CO_2 capture technology from lab to pilot scale at IFK, University of Stuttgart, Fuel 127 (2014) 23-37.

[38] M. Erans, V. Manovic, E.J. Anthony, Calcium looping sorbents for CO_2 capture, Applied Energy 180 (2016) 722–742.

[39] P. Fennell, Calcium and chemical looping technology: an introduction, Calcium and Chemical Looping Technology for Power Generation and Carbon Dioxide (CO_2) Capture, Elsevier2015, pp. 3-14.

[40] A. Perejón, L.M. Romeo, Y. Lara, P. Lisbona, A. Martínez, J.M. Valverde, The Calcium-Looping technology for CO_2 capture: On the important roles of energy integration and sorbent behavior, Applied Energy 162 (2016) 787-807.

[41] J. Yin, C. Qin, B. Feng, L. Ge, C. Luo, W. Liu, H. An, Calcium looping for CO_2 capture at a constant high temperature, Energy & Fuels 28 (2013) 307–318.

[42] S. Freguia, G.T. Rochelle, Modeling of CO_2 capture by aqueous monoethanolamine, AIChE Journal 49 (2003) 1676-1686.

[43] P. Luis, Use of monoethanolamine (MEA) for CO_2 capture in a global scenario: Consequences and alternatives, Desalination 380 (2016) 93-99.

[44] B. Arias, M. Diego, J. Abanades, M. Lorenzo, L. Diaz, D. Martínez, J. Alvarez, A. Sánchez-Biezma, Demonstration of steady state CO_2 capture in a 1.7 MWth calcium looping pilot, International Journal of Greenhouse Gas Control 18 (2013) 237-245.

[45] J. Yin, C. Qin, H. An, W. Liu, B. Feng, High-temperature pressure swing adsorption process for CO_2 separation, Energy & Fuels 26 (2011) 169–175.

[46] L. Fedunik-Hofman, A. Bayon, S.W. Donne, Comparative kinetic analysis of $CaCO_3$/CaO reaction system for energy storage and carbon capture, Applied Sciences 9 (2019) 4601.

[47] P. Sun, J.R. Grace, C.J. Lim, E.J. Anthony, Determination of intrinsic rate constants of the CaO–CO_2 reaction, Chemical Engineering Science 63 (2008) 47-56.

[48] D.K. Lee, An apparent kinetic model for the carbonation of calcium oxide by carbon dioxide, Chemical Engineering Journal 100 (2004) 71-77.

[49] B. Khoshandam, R.V. Kumar, L. Allahgholi, Mathematical modeling of CO2 removal using carbonation with CaO: The grain model, Korean Journal of Chemical Engineering 27 (2010) 766-776.

[50] J.C. Abanades, D. Alvarez, Conversion limits in the reaction of CO_2 with lime, Energy & Fuels 17 (2003) 308-315.

[51] J. Wang, E.J. Anthony, On the decay behavior of the CO_2 absorption capacity of CaO-based sorbents, Industrial & engineering chemistry research 44 (2005) 627-629.

[52] G.S. Grasa, J.C. Abanades, CO_2 capture capacity of CaO in long series of carbonation/calcination cycles, Industrial & Engineering Chemistry Research 45 (2006) 8846–8851.

[53] R.H. Borgwardt, Sintering of nascent calcium oxide, Chemical Engineering Science 44 (1989) 53–60.

[54] L. Huang, Q. Zheng, B. Louis, Q. Wang, A facile Solvent/Nonsolvent Preparation of Sintering-Resistant MgO/CaO Composites for High-Temperature CO_2 Capture, Energy Technology 6 (2018) 2469-2478.

[55] W. Liu, B. Feng, Y. Wu, G. Wang, J. Barry, J.o.C. Diniz da Costa, Synthesis of sintering-resistant sorbents for CO_2 capture, Environmental science & technology 44 (2010) 3093-3097.

[56] M. Zhao, Y. Song, G. Ji, X. Zhao, Demonstration of polymorphic spacing strategy against sintering: Synthesis of stabilized calcium looping absorbents for high-temperature CO_2 sorption, Energy & Fuels 32 (2018) 5443-5452.

[57] M. Wang, A. Lawal, P. Stephenson, J. Sidders, C. Ramshaw, Post-combustion CO_2 capture with chemical absorption: A state-of-the-art review, Chemical engineering research and design 89 (2011) 1609-1624.

[58] M. Zhao, A.I. Minett, A.T. Harris, A review of techno-economic models for the retrofitting of conventional pulverised-coal power plants for post-combustion capture (PCC) of CO_2, Energy & Environmental Science 6 (2013) 25–40.

[59] R.K. Pachauri, M.R. Allen, V.R. Barros, J. Broome, W. Cramer, R. Christ, J.A. Church, L. Clarke, Q. Dahe, P. Dasgupta, Climate change 2014: synthesis report. Contribution of Working Groups I, II and III to the fifth assessment report of the Intergovernmental Panel on Climate Change, Ipcc2014.

[60] N. MacDowell, N. Florin, A. Buchard, J. Hallett, A. Galindo, G. Jackson, C.S. Adjiman, C.K. Williams, N. Shah, P. Fennell, An overview of CO_2 capture technologies, Energy & Environmental Science 3 (2010) 1645–1669.

[61] J.D. Figueroa, T. Fout, S. Plasynski, H. McIlvried, R.D. Srivastava, Advances in CO_2 capture technology—the US Department of Energy's Carbon Sequestration Program, International journal of greenhouse gas control 2 (2008) 9–20.

[62] B. Li, Y. Duan, D. Luebke, B. Morreale, Advances in CO_2 capture technology: A patent review, Applied Energy 102 (2013) 1439–1447.

[63] D.P. Hanak, C. Biliyok, E.J. Anthony, V. Manovic, Modelling and comparison of calcium looping and chemical solvent scrubbing retrofits for CO_2 capture from coal-fired power plant, International Journal of Greenhouse Gas Control 42 (2015) 226–236.

[64] S. Chi, G.T. Rochelle, Oxidative degradation of monoethanolamine, Industrial & engineering chemistry research 41 (2002) 4178–4186.

[65] G.S. Goff, G.T. Rochelle, Monoethanolamine degradation: O_2 mass transfer effects under CO_2 capture conditions, Industrial & Engineering Chemistry Research 43 (2004) 6400–6408.

[66] G. Fytianos, S. Ucar, A. Grimstvedt, A. Hyldbakk, H.F. Svendsen, H.K. Knuutila, Corrosion and degradation in MEA based post-combustion CO_2 capture, International Journal of Greenhouse Gas Control 46 (2016) 48–56.

[67] I.R. Soosaiprakasam, A. Veawab, Corrosion and polarization behavior of carbon steel in MEA-based CO_2 capture process, International journal of greenhouse gas control 2 (2008) 553–562.

[68] T. Shimizu, T. Hirama, H. Hosoda, K. Kitano, M. Inagaki, K. Tejima, A twin fluid-bed reactor for removal of CO_2 from combustion processes, Chemical Engineering Research and Design 77 (1999) 62–68.

[69] E. Baker, The calcium oxide–carbon dioxide system in the pressure range 1—300 atmospheres, Journal of the Chemical Society (1962) 464-470.

[70] V. Manovic, E.J. Anthony, Lime-Based Sorbents for High-Temperature CO_2 Capture—A Review of Sorbent Modification Methods, International Journal of Environmental Research and Public Health 7 (2010) 3129–3140.

[71] W. Liu, H. An, C. Qin, J. Yin, G. Wang, B. Feng, M. Xu, Performance enhancement of calcium oxide sorbents for cyclic CO_2 capture□A review, Energy & Fuels 26 (2012) 2751–2767.

[72] Y.-j. Li, C.-s. Zhao, L.-b. Duan, C. Liang, Q.-z. Li, W. Zhou, H.-c. Chen, Cyclic calcination/carbonation looping of dolomite modified with acetic acid for CO_2 capture, Fuel Processing Technology 89 (2008) 1461–1469.

[73] K. Wang, X. Hu, P. Zhao, Z. Yin, Natural dolomite modified with carbon coating for cyclic high-temperature CO_2 capture, Applied energy 165 (2016) 14–21.

[74] K. Wang, Z. Yin, P. Zhao, D. Han, X. Hu, G. Zhang, Effect of chemical and physical treatments on the properties of a dolomite used in Ca looping, Energy & Fuels 29 (2015) 4428–4435.

[75] Z. Li, J. Ouyang, G. Luo, H. Yao, High-Efficiency CaO-Based Sorbent Modified by Aluminate Cement and Organic Fiber Through Wet Mixing Method, Industrial & Engineering Chemistry Research 58 (2019) 22040-22047.

[76] X. Ma, Y. Li, X. Yan, W. Zhang, J. Zhao, Z. Wang, Preparation of a morph-genetic CaO-based sorbent using paper fibre as a biotemplate for enhanced CO_2 capture, Chemical Engineering Journal 361 (2019) 235-244.

[77] J. Chen, L. Duan, Z. Sun, Accurate control of cage-like CaO hollow microspheres for enhanced CO_2 capture in calcium looping via a template-assisted synthesis approach, Environmental science & technology 53 (2019) 2249-2259.

[78] J. Ebri, J. Valverde, M. Quintanilla, High intensity sound enhances calcination and CO_2 capture of limestone and dolomite at Ca-looping conditions, Industrial & Engineering Chemistry Research 55 (2016) 8671–8678.

[79] A. Kurlov, M. Broda, D. Hosseini, S.J. Mitchell, J. Perez-Ramirez, C.R. Muller, Mechanochemically Activated, Calcium Oxide-Based, Magnesium Oxide-Stabilized Carbon Dioxide Sorbents, ChemSusChem 9 (2016) 2380–2390.

[80] M. Sayyah, Y. Lu, R.I. Masel, K.S. Suslick, Mechanical activation of CaO-based adsorbents for CO_2 capture, ChemSusChem 6 (2013) 193–198.

[81] J. Sun, W.Q. Liu, M.K. Li, X.W. Yang, W.Y. Wang, Y.C. Hu, H.Q. Chen, X. Li, M.H. Xu, Mechanical Modification of Naturally Occurring Limestone for High-Temperature CO_2 Capture, Energy & Fuels 30 (2016) 6597–6605.

[82] J. Sun, Y. Yang, Y. Guo, Y. Xu, W. Li, C. Zhao, W. Liu, P. Lu, Stabilized CO_2 capture performance of wet mechanically activated dolomite, Fuel 222 (2018) 334–342.

[83] R. Molinder, T.P. Comyn, N. Hondow, J.E. Parker, V. Dupont, In situ X-ray diffraction of CaO based CO_2 sorbents, Energy & Environmental Science 5 (2012) 8958.

[84] N. Koga, J. Criado, The influence of mass transfer phenomena on the kinetic analysis for the thermal decomposition of calcium carbonate by constant rate thermal analysis (CRTA) under vacuum, International journal of chemical kinetics 30 (1998) 737-744.

[85] J.M. Valverde, A. Perejon, S. Medina, L.A. Perez-Maqueda, Thermal decomposition of dolomite under CO 2: insights from TGA and in situ XRD analysis, Physical Chemistry Chemical Physics 17 (2015) 30162-30176.

[86] A. Biasin, C. Segre, G. Salviulo, F. Zorzi, M. Strumendo, Investigation of CaO–CO_2 reaction kinetics by in-situ XRD using synchrotron radiation, Chemical Engineering Science 127 (2015) 13–24.

[87] D. Alvarez, J.C. Abanades, Pore-size and shape effects on the recarbonation performance of calcium oxide submitted to repeated calcination/recarbonation cycles, Energy & Fuels 19 (2005) 270–278.

[88] S. Lu, Q. Lin, S. Wu, Synergy of Pore Size and Specific Surface Area on the CO_2 Sorption Performance of Nano CaO-Based Sorbents, J Nanosci Nanotechnol 19 (2019) 3205–3209.

[89] J. Blunden, D. Arndt, State of the Climate in 2019, Bulletin of the American Meteorological Society 101 (2020) S1-S429.

[90] A. Charitos, C. Hawthorne, A. Bidwe, S. Sivalingam, A. Schuster, H. Spliethoff, G. Scheffknecht, Parametric investigation of the calcium looping process for CO_2 capture in a 10 kWth dual fluidized bed, International Journal of Greenhouse Gas Control 4 (2010) 776-784.

[91] A. Martínez, Y. Lara, P. Lisbona, L.M. Romeo, Energy penalty reduction in the calcium looping cycle, International Journal of Greenhouse Gas Control 7 (2012) 74-81.

[92] M.E. Boot-Handford, J.C. Abanades, E.J. Anthony, M.J. Blunt, S. Brandani, N. Mac Dowell, J.R. Fernández, M.-C. Ferrari, R. Gross, J.P. Hallett, Carbon capture and storage update, Energy & Environmental Science 7 (2014) 130-189.

[93] M. Krödel, A. Landuyt, P.M. Abdala, C.R. Müller, Mechanistic Understanding of CaO-Based Sorbents for High-Temperature CO_2 Capture: Advanced Characterization and Prospects, ChemSusChem 13 (2020) 6259-6272.

[94] E. Hassani, F. Feyzbar-Khalkhali-Nejad, A. Rashti, T.-S. Oh, Carbonation, regeneration, and cycle stability of the mechanically activated $Ca(OH)_2$ sorbents for CO_2 capture: an in situ X-ray diffraction study, Industrial & Engineering Chemistry Research (2020).

[95] N.H. Florin, A.T. Harris, Reactivity of CaO derived from nano-sized $CaCO_3$ particles through multiple CO_2 capture-and-release cycles, Chemical Engineering Science 64 (2009) 187-191.

[96] Y. Hu, W. Liu, J. Sun, M. Li, X. Yang, Y. Zhang, X. Liu, M. Xu, Structurally improved CaO-based sorbent by organic acids for high temperature CO_2 capture, Fuel 167 (2016) 17-24.

[97] J. Chen, L. Duan, Z. Sun, Review on the development of sorbents for calcium looping, Energy & Fuels 34 (2020) 7806-7836.

[98] A.M. Kierzkowska, R. Pacciani, C.R. Müller, CaO-based CO_2 sorbents: from fundamentals to the development of new, highly effective materials, ChemSusChem 6 (2013) 1130-1148.

[99] W. Liu, H. An, C. Qin, J. Yin, G. Wang, B. Feng, M. Xu, Performance enhancement of calcium oxide sorbents for cyclic CO_2 capture: A review, Energy & Fuels 26 (2012) 2751-2767.

[100] Y. Hu, W. Liu, H. Chen, Z. Zhou, W. Wang, J. Sun, X. Yang, X. Li, M. Xu, Screening of inert solid supports for CaO-based sorbents for high temperature CO_2 capture, Fuel 181 (2016) 199-206.

[101] Y. Hu, H. Lu, W. Liu, Y. Yang, H. Li, Incorporation of CaO into inert supports for enhanced CO_2 capture: Recent progress and new trends, Chemical Engineering Journal (2020) 125253.

[102] K. Gao, M. Shokrollahi Yancheshmeh, J.e. Duchesne, M.C. Iliuta, Valorization of coal fly ash as a stabilizer for the development of Ni/CaO-based bifunctional material, ACS Sustainable Chemistry & Engineering 8 (2020) 3885-3895.

[103] M. Aissaoui, O.A.Z. Sahraei, M.S. Yancheshmeh, M.C. Iliuta, Development of a Fe/Mg-bearing metallurgical waste stabilized-CaO/NiO hybrid sorbent-catalyst for high purity H2 production through sorption-enhanced glycerol steam reforming, International Journal of Hydrogen Energy 45 (2020) 18452-18465.

[104] H.R. Radfarnia, M.C. Iliuta, Metal oxide-stabilized calcium oxide CO_2 sorbent for multicycle operation, Chemical engineering journal 232 (2013) 280-289.

[105] C. Qin, J. Yin, C. Luo, H. An, W. Liu, B. Feng, Enhancing the performance of CaO/CuO based composite for CO_2 capture in a combined Ca–Cu chemical looping process, Chemical engineering journal 228 (2013) 75-86.

[106] J. Chen, L. Duan, T. Shi, R. Bian, Y. Lu, F. Donat, E.J. Anthony, A facile one-pot synthesis of CaO/CuO hollow microspheres featuring highly porous shells for enhanced CO 2 capture in a combined Ca–Cu looping process via a template-free synthesis approach, Journal of Materials Chemistry A 7 (2019) 21096-21105.

[107] S.S. Kazi, A. Aranda, L. Di Felice, J. Meyer, R. Murillo, G. Grasa, Development of cost effective and high performance composite for CO_2 capture in Ca-Cu looping process, Energy Procedia 114 (2017) 211-219.

[108] V. Manovic, Y. Wu, I. He, E.J. Anthony, Core-in-shell CaO/CuO-based composite for CO_2 capture, Industrial & engineering chemistry research 50 (2011) 12384-12391.

[109] L.T. Minardi, F.H. Alshafei, Z.K. Mishra, D.A. Simonetti, Impacts of metal oxide additives on the capacity and stability of calcium oxide based materials for the reactive sorption of CO 2, Sustainable Energy & Fuels 5 (2021) 767-778.

[110] F.H. Alshafei, L.T. Minardi, D. Rosales, G. Chen, D.A. Simonetti, Improved Sorption-Enhanced Steam Methane Reforming via Calcium Oxide–Based Sorbents with Targeted Morphology, Energy Technology 7 (2019) 1800807.

[111] L. Han, Q. Liu, Y. Zhang, Q. Wang, N. Rong, X. Liang, Y. Feng, K. Ma, M. Yan, Y. Hu, Catalytic toluene reforming with in situ CO_2 capture via an iron–calcium hybrid absorbent for promoted hydrogen production, Energy Technology 8 (2020) 2000083.

[112] L. Han, Q. Liu, Y. Zhang, K. Lin, G. Xu, Q. Wang, N. Rong, X. Liang, Y. Feng, P. Wu, A novel hybrid iron-calcium catalyst/absorbent for enhanced hydrogen production via catalytic tar reforming with in-situ CO_2 capture, International Journal of Hydrogen Energy 45 (2020) 10709-10723.

[113] X. Ma, Y. Li, Y. Qian, Z. Wang, A carbide slag-based, Ca12Al14O33-Stabilized sorbent prepared by the hydrothermal template method enabling efficient CO_2 capture, Energies 12 (2019) 2617.

[114] K. Liu, B. Zhao, Y. Wu, F. Li, Q. Li, J. Zhang, Bubbling synthesis and high-temperature CO_2 adsorption performance of CaO-based adsorbents from carbide slag, Fuel 269 (2020) 117481.

[115] B. Zhao, L. Ma, H. Shi, K. Liu, J. Zhang, Calcium precursor from stirring processes at room temperature for controllable preparation of nano-structure CaO sorbents for high-temperature CO_2 adsorption, Journal of CO_2 Utilization 25 (2018) 315-322.

[116] D. Cazorla-Amoros, A. Linares-Solano, C. Salinas-Martinez de Lecea, J. Joly, A temperature-programmed reaction study of calcium-catalyzed carbon gasification, Energy & fuels 6 (1992) 287-293.

[117] J. Joly, D. Cazorla-Amoros, H. Charcosset, A. Linares-Solano, N. Marcilio, A. Martinez-Alonso, C.S.-M. de Lecea, The state of calcium as a char gasification catalyst—a temperature-programmed reaction study, Fuel 69 (1990) 878-884.

[118] K. Hill, E. Winter, Thermal dissociation pressure of calcium carbonate, The Journal of Physical Chemistry 60 (1956) 1361-1362.

[119] V. Shah, Z. Cheng, D.S. Baser, J.A. Fan, L.-S. Fan, Highly Selective Production of Syngas from Chemical Looping Reforming of Methane with CO_2 Utilization on MgO-supported Calcium Ferrite Redox Materials, Applied Energy 282 (2021) 116111.

[120] Y. Zhao, B. Jin, X. Luo, Z. Liang, Thermodynamic evaluation and experimental investigation of CaO-assisted Fe-based chemical looping reforming process for syngas production, Applied Energy 288 (2021) 116614.

[121] M. Ismail, W. Liu, M.S. Chan, M.T. Dunstan, S.A. Scott, Synthesis, application, and carbonation behavior of $Ca_2Fe_2O_5$ for chemical looping H_2 production, Energy & Fuels 30 (2016) 6220-6232.

[122] C. Dang, Y. Li, S.M. Yusuf, Y. Cao, H. Wang, H. Yu, F. Peng, F. Li, Calcium cobaltate: a phase-change catalyst for stable hydrogen production from bio-glycerol, Energy & Environmental Science 11 (2018) 660-668.

[123] Z. Sun, S. Chen, J. Hu, A. Chen, A.H. Rony, C.K. Russell, W. Xiang, M. Fan, M.D. Dyar, E.C. Dklute, Ca2Fe2O5: A promising oxygen carrier for CO/CH4 conversion and almost-pure H2 production with inherent CO_2 capture over a two-step chemical looping hydrogen generation process, Applied Energy 211 (2018) 431-442.

[124] F. Feyzbar-Khalkhali-Nejad, E. Hassani, A. Rashti, T.-S. Oh, Adsorption-based CO removal: principles and materials, Journal of Environmental Chemical Engineering (2021) 105317.

[125] M.T. Izquierdo, A. Saleh, E. Sánchez-Fernández, M.M. Maroto-Valer, S. García, High-temperature CO_2 capture by Li_4SiO_4 sorbents: effect of CO_2 concentration and cyclic performance under representative conditions, Industrial & Engineering Chemistry Research 57 (2018) 13802-13810.

[126] M.B. Chowdhury, M.R. Quddus, H.I. deLasa, CO_2 capture with a novel solid fluidizable sorbent: thermodynamics and temperature programmed carbonation–decarbonation, Chemical engineering journal 232 (2013) 139-148.

[127] F. Garcıa-Labiano, A. Abad, L. De Diego, P. Gayán, J. Adánez, Calcination of calcium-based sorbents at pressure in a broad range of CO_2 concentrations, Chemical engineering science 57 (2002) 2381-2393.

[128] A. Linares-Solano, M. Almela-Alarcón, C.S.-M. de Lecea, CO_2 chemisorption to characterize calcium catalysts in carbon gasification reactions, Journal of Catalysis 125 (1990) 401-410.

[129] C. Jo-Shu, J.P. Adcock, L.L. Lauderback, J.L. Falconer, TPR and SIMS studies of $CaCO_3$ catalyzed CO_2 gasification of carbon, Carbon 27 (1989) 593-602.

[130] K. Leary, J. Michaels, A. Stacy, Temperature-programmed desorption: Multisite and subsurface diffusion models, AIChE journal 34 (1988) 263-271.

[131] H. Sun, C. Wu, B. Shen, X. Zhang, Y. Zhang, J. Huang, Progress in the development and application of CaO-based adsorbents for CO_2 capture—a review, Materials Today Sustainability 1 (2018) 1-27.

[132] R.T. Downs, M. Hall-Wallace, The American Mineralogist crystal structure database, American Mineralogist 88 (2003) 247-250.

[133] S. Gražulis, D. Chateigner, R.T. Downs, A. Yokochi, M. Quirós, L. Lutterotti, E. Manakova, J. Butkus, P. Moeck, A. Le Bail, Crystallography Open Database–an open-access collection of crystal structures, Journal of applied crystallography 42 (2009) 726-729.

[134] S. Gražulis, A. Daškevič, A. Merkys, D. Chateigner, L. Lutterotti, M. Quiros, N.R. Serebryanaya, P. Moeck, R.T. Downs, A. Le Bail, Crystallography Open Database (COD): an open-access collection of crystal structures and platform for world-wide collaboration, Nucleic acids research 40 (2012) D420-D427.

[135] S. Gražulis, A. Merkys, A. Vaitkus, M. Okulič-Kazarinas, Computing stoichiometric molecular composition from crystal structures, Journal of applied crystallography 48 (2015) 85-91.

[136] A. Merkys, A. Vaitkus, J. Butkus, M. Okulič-Kazarinas, V. Kairys, S. Gražulis, COD:: CIF:: Parser: an error-correcting CIF parser for the Perl language, Journal of applied crystallography 49 (2016) 292-301.

[137] M. Quirós, S. Gražulis, S. Girdzijauskaitė, A. Merkys, A. Vaitkus, Using SMILES strings for the description of chemical connectivity in the Crystallography Open Database, Journal of cheminformatics 10 (2018) 1-17.

[138] A. Vaitkus, A. Merkys, S. Gražulis, Validation of the crystallography open database using the crystallographic information framework, Journal of applied crystallography 54 (2021).

[139] I. Zamboni, C. Courson, A. Kiennemann, Synthesis of Fe/CaO active sorbent for CO_2 absorption and tars removal in biomass gasification, Catalysis today 176 (2011) 197-201.

[140] J. Landers, G.Y. Gor, A.V. Neimark, Density functional theory methods for characterization of porous materials, Colloids and Surfaces A: Physicochemical and Engineering Aspects 437 (2013) 3-32.

[141] S. Nouri, H. Ebrahim, Effect of sorbent pore volume on the carbonation reaction of lime with CO_2, Brazilian Journal of Chemical Engineering 33 (2016) 383-389.

[142] S. Lu, Q. Lin, S. Wu, Synergy of pore size and specific surface area on the CO2 sorption performance of nano CaO-based sorbents, Journal of nanoscience and nanotechnology 19 (2019) 3205-3209.

[143] S. Wei, R. Han, Y. Su, J. Gao, G. Zhao, Y. Qin, Pore structure modified CaO-based sorbents with different sized templates for CO_2 capture, Energy & Fuels 33 (2019) 5398-5407.

[144] H. Lu, A. Khan, P.G. Smirniotis, Relationship between structural properties and CO_2 capture performance of CaO− based sorbents obtained from different organometallic precursors, Industrial & Engineering Chemistry Research 47 (2008) 6216-6220.

[145] R. Nassar, T.G. Hill, C.A. McLinden, D. Wunch, D.B. Jones, D. Crisp, Quantifying CO_2 emissions from individual power plants from space, Geophysical Research Letters 44 (2017) 10,045-010,053.

[146] J.L. Bullister, Atmospheric Histories (1765-2015) for CFC-11, CFC-12, CFC-113, CCl4, SF6 and N2O, Carbon Dioxide Information Analysis Center, Oak Ridge National Laboratory, US Department of Energy, Oak Ridge, Tennessee (2015).

[147] M.P. Santos, V. Manovic, D.P. Hanak, Unlocking the potential of pulp and paper industry to achieve carbon-negative emissions via calcium looping retrofit, Journal of Cleaner Production 280 (2021) 124431.

[148] D.P. Hanak, M. Erans, S.A. Nabavi, M. Jeremias, L.M. Romeo, V. Manovic, Technical and economic feasibility evaluation of calcium looping with no CO_2 recirculation, Chemical Engineering Journal 335 (2018) 763-773.

[149] M. Erans, D.P. Hanak, J. Mir, E.J. Anthony, V. Manovic, Process modelling and techno-economic analysis of natural gas combined cycle integrated with calcium looping, Thermal Science 20 (2016) 59-67.

[150] M. Zhao, A.I. Minett, A.T. Harris, A review of techno-economic models for the retrofitting of conventional pulverised-coal power plants for post-combustion capture (PCC) of CO 2, Energy & Environmental Science 6 (2013) 25-40.

[151] D.P. Hanak, V. Manovic, Economic feasibility of calcium looping under uncertainty, Applied Energy 208 (2017) 691-702.

[152] D.P. Hanak, A.J. Kolios, V. Manovic, Comparison of probabilistic performance of calcium looping and chemical solvent scrubbing retrofits for CO_2 capture from coal-fired power plant, Applied Energy 172 (2016) 323-336.

[153] J. Abanades, Calcium looping for CO_2 capture in combustion systems, Fluidized bed technologies for near-zero emission combustion and gasification (2013) 931-970.

[154] A. Nawar, M. Ali, A.H. Khoja, A. Waqas, M. Anwar, M. Mahmood, Enhanced CO_2 capture using organic acid structure modified waste eggshell derived CaO sorbent, Journal of Environmental Chemical Engineering 9 (2021) 104871.

[155] F.D.M. Daud, K. Vignesh, S. Sreekantan, A.R. Mohamed, Improved CO 2 adsorption capacity and cyclic stability of CaO sorbents incorporated with MgO, New Journal of Chemistry 40 (2016) 231-237.

[156] Y. Xu, C. Luo, Y. Zheng, H. Ding, Q. Wang, Q. Shen, X. Li, L. Zhang, Characteristics and performance of CaO-based high temperature CO 2 sorbents derived from a sol–gel process with different supports, RSC advances 6 (2016) 79285-79296.

[157] X. Zhang, Z. Li, Y. Peng, W. Su, X. Sun, J. Li, Investigation on a novel CaO–Y_2O_3 sorbent for efficient CO_2 mitigation, Chemical Engineering Journal 243 (2014) 297-304.

[158] J. Chen, F. Donat, L. Duan, A.M. Kierzkowska, S.M. Kim, Y. Xu, E.J. Anthony, C.R. Mueller, Metal-oxide stabilized CaO/CuO composites for the integrated Ca/Cu looping process, Chemical Engineering Journal 403 (2021) 126330.

[159] Y. Hu, H. Lu, W. Liu, Y. Yang, H. Li, Incorporation of CaO into inert supports for enhanced CO_2 capture: A review, Chemical Engineering Journal 396 (2020) 125253.

[160] M. Abolghasemi, A. Keshavarz, M.A. Mehrabian, Thermodynamic analysis of a thermal storage unit under the influence of nano-particles added to the phase change material and/or the working fluid, Heat and Mass Transfer 48 (2012) 1961-1970.

[161] W.M. Haynes, D.R. Lide, T.J. Bruno, CRC handbook of chemistry and physics, CRC press2016.

[162] E. Hassani, J. Cho, F. Feyzbar-Khalkhali-Nejad, A. Rashti, S.S. Jang, T.-S. Oh, Ca_2CuO_3: A high temperature CO_2 sorbent with rapid regeneration kinetics, Journal of Environmental Chemical Engineering 10 (2022) 107334.

[163] L. Lutterotti, Maud: a Rietveld analysis program designed for the internet and experiment integration, Acta Crystallogr. A 56 (2000) s54.

[164] F. Feyzbar-Khalkhali-Nejad, E. Hassani, K.D. Leonard, T.-S. Oh, A highly stable CuO-derived adsorbent with dual Cu (I) sites for selective CO adsorption, Separation and Purification Technology (2022) 120906.

[165] A. Patterson, The Scherrer formula for X-ray particle size determination, Physical review 56 (1939) 978.

[166] B. González, G.S. Grasa, M. Alonso, J.C. Abanades, Modeling of the deactivation of CaO in a carbonate loop at high temperatures of calcination, Industrial & engineering chemistry research 47 (2008) 9256-9262.

[167] V. Manovic, E.J. Anthony, Thermal activation of CaO-based sorbent and self-reactivation during CO_2 capture looping cycles, Environmental science & technology 42 (2008) 4170-4174.

[168] A. Subramaniyan, R. Ilangovan, Thermal Conductivity of Cu2O-TiO2 Composite-Nanofluid Based on Maxwell model, International Journal of Nanoscience and Nanotechnology 11 (2015) 59-62.

[169] Z. Yang, K. Yuan, J. Meng, X. Zhang, D. Tang, M. Hu, Why thermal conductivity of CaO is lower than that of CaS: a study from the perspective of phonon splitting of optical mode, Nanotechnology 32 (2020) 025709.

[170] H. Ebadi-Dehaghani, M. Reiszadeh, A. Chavoshi, M. Nazempour, M. Vakili, The effect of zinc oxide and calcium carbonate nanoparticles on the thermal conductivity of polypropylene, Journal of Macromolecular Science, Part B 53 (2014) 93-107.

Appendix A Supporting information for chapter 2

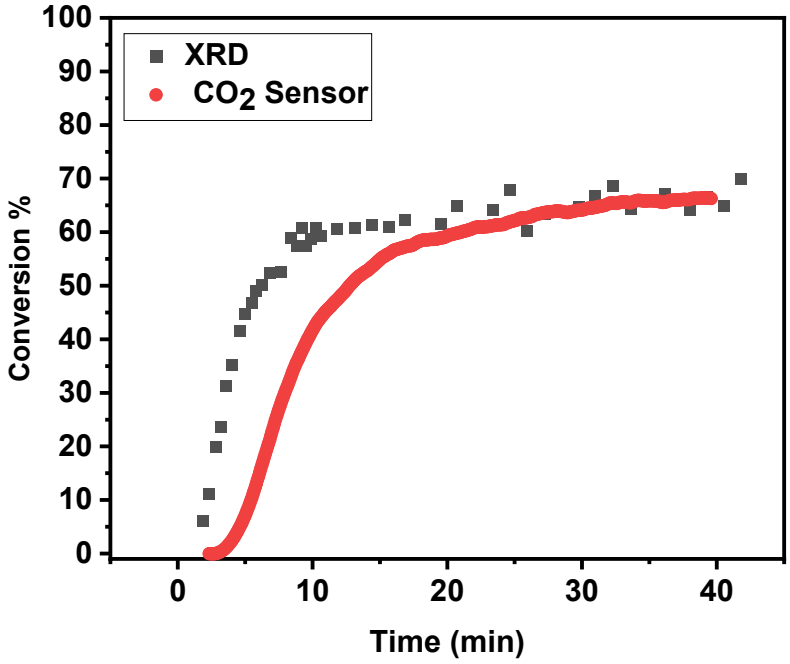

Figure A.1. Comparison of conversion calculation based on the Rietveld refinement (XRD) and CO_2 concentration in exhausted gas (CO_2 Sensor).

There is good agreement between the final sorbent conversions calculated by Rietveld refinement (XRD) and CO_2 Sensor. The delayed response in CO_2 sensor is because of the dead volume of the reactor and long tubing from the reactor outlet and CO_2 sensor inlet.